Flux Expulsion in Coaxial Superconducting Radiofrequency Cavities

by

RuthAnn Rose Gregory

A Thesis Submitted in Partial Fulfillment of the
Requirements for the Degree of

MASTER OF SCIENCE

in the Department of Physics

University of Victoria

Flux Expulsion in Coaxial Superconducting Radiofrequency Cavities

by

RuthAnn Rose Gregory
B.Sc., Michigan State University, 2018

Supervisory Committee

Prof. Robert Laxdal, Co-Supervisor
Department of Physics

Prof. Tobias Junginger, Co-Supervisor
Department of Physics

Abstract

This thesis explores the effects of different cool-down speeds and applied magnetic fields on TRIUMF's coaxial cavities using COMSOL ® simulations and experimental results. Magnetic sensitivity describes how sensitive the surface resistance of a material is to an external magnetic field, and is an important characteristic of SRF accelerator design. Reducing magnetic sensitivity can improve cavity performance. Previous studies have shown that nitrogen doped elliptical cavities are very sensitive to external fields compared to conventionally treated cavities, resulting in stringent requirements for the residual field and cavity cool-down speed. Few such studies have been done on non-elliptical cavities such as half wave resonators (HWRs) and quarter wave resonators (QWRs). Factors affecting magnetic sensitivity include cavity treatment, rf field distribution inside the cavity, external magnetic field direction, cool-down speed, and thermal gradient during transition to the superconducting state. Reducing the magnetic sensitivity can improve cavity performance since in practice it is impossible to eliminate all residual magnetic fields from external sources such as Earth's natural magnetic field during a cool-down.

It was found that magnetic sensitivity is not an ideal parameter for characterizing TRIUMF's HWR and QWR since these cavities exhibit non-uniform flux trapping. Therefore, the parameter normalized R_{mag} is introduced. Normalized R_{mag}, or R_{magN} is the additional surface resistance introduced by applying a dc magnetic field to the cavity, divided by the applied magnetic field. The HWR's normalized R_{mag} is compared for different resonant frequencies after 400 and 120 ℃ bakes, with the 120 ℃ bake resulting in lower normalized R_{mag}. The normalized R_{mag} was found to generally increase with frequency for both the HWR and QWR.

The study also seeks to maximize flux expulsion, which occurs when a cavity is cooled down through its superconducting temperature. Flux expulsion is affected by cool-down speed, temperature gradient, and cavity orientation relative to an applied magnetic field. The effects of cool-down speed and temperature gradient on flux expulsion were found to be insignificant for the QWR with a vertically applied magnetic field. However, a horizontal magnetic field can be nearly completely expelled by a fast, high temperature gradient cool-down.

Contents

List of Tables

List of Figures

Acknowledgments

Firstly I would like to thank Philipp Kolb and Bob Laxdal for all of their teaching, guidance and help with editing this thesis. I would like to thank Tobi Junginger for taking me on as a graduate student and teaching me topics on accelerator physics. I would also like to thank Zhongyuan Yao for his help with cavity tests and COMSOL simulations. Also thank you to Johnson Cheung, Rowan Bjarnason and David Kishi for supplying helium and operating the cryogenics systems during our cavity tests.

Also special thanks to Bryan Dury for laying the foundation for the COMSOL ® simulations performed in this thesis.

I would like to thank Angela Kang, Lin Manuel Miranda and everyone who worked with them for creating wonderful works of art. Last but not least I would like to thank both my parents for the invaluable support they have given me throughout my entire life.

Dedication

"Work is the best antidote to sorrow, my dear Watson."

-Sir Arthur Conan Doyle, *The Return of Sherlock Holmes*

Chapter 1

Introduction and Background

1.1 Particle Accelerators

Particle accelerators are devices that accelerate beams of charged particles. Accelerators have many important applications for both pure scientific research and practical uses. One example of a scientific discovery made with particle accelerators is the discovery of the Higgs boson particle. The Higgs boson has an important role in explaining why objects have mass. This discovery was made at the Conseil Européen pour la Recherche Nucléaire (CERN) with the use of the Large Hadron Collider (LHC), the world's largest particle accelerator [1]. This discovery was made possible by the continued improvement of particle accelerator technology.

One example of an application for particle accelerators is proton therapy as a cancer treatment [2]. Proton therapy works by directing a beam of high-energy protons towards cancerous tumors to destroy them while doing less collateral damage to healthy cells compared to conventional radiation treatments [2]. Another practical use for particle accelerators is the treatment of waste products created by nuclear power plants. Nuclear power plants can generate electricity, but they produce hazardous waste products in the process. For example, the facilities described as Accelerator-driven Transmutation Waste (ATW) make use of an accelerator to treat its radio-toxic waste products [3]. Improving particle accelerator technology can make these practical uses more efficient and lead to new scientific discoveries and enable societal benefits.

Particle accelerators accelerate beams of charged particles using either constant or oscillating electric fields and steer and focus them using electric and magnetic fields. Modern particle accelerators use radio frequency (RF) cavities to accelerate beams of charged particles by imparting energy to the beam. RF cavities are chambers containing an electromagnetic field. When charged particles enter this field they experience an electrical force that accelerates them [4].

1.2 Resonant Cavities

A key component of many modern accelerators is an electromagnetic cavity that uses oscillating electromagnetic fields to increase the kinetic energy of charged particles. When a charged particle passes through an electric field generated by an RF cavity, it will experience an accelerating force called the Lorentz force

$$F = q \cdot (\mathbf{E} + \mathbf{v} \times \mathbf{B}), \tag{1.1}$$

where q is the charge of the particle, $\mathbf{v}$ is the velocity of the particle, and $\mathbf{E}$ and $\mathbf{B}$ are the electric and magnetic fields generated by the cavity.

The magnetic field can also be expressed as $\mathbf{H}$ where $\mathbf{H} = \mathbf{B}/\mu_0$ where μ_0 is the vacuum permeability. Some other useful equations for analyzing RF cavities are Maxwell's equations in free space

$$\nabla \times \mathbf{E} = \frac{\partial \mathbf{B}}{\partial t} \tag{1.2}$$

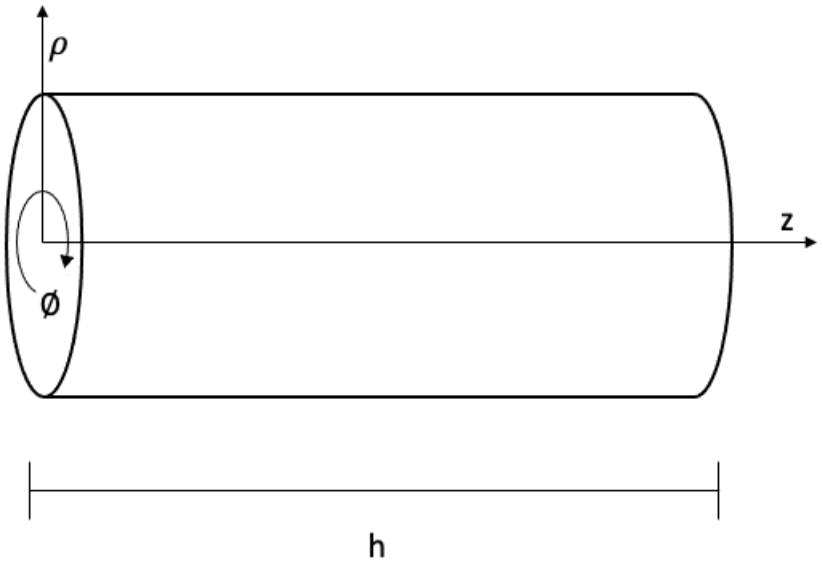

Figure 1.1: Sketch of a cylindrical cavity, also known as a pill-box cavity with cylindrical coordinates superimposed.

$$\nabla \times \mathbf{H} = \mathbf{J} + \frac{\partial D}{\partial t} \tag{1.3}$$

$$\nabla \cdot \mathbf{D} = \rho_v \tag{1.4}$$

$$\nabla \cdot \mathbf{B} = 0 \tag{1.5}$$

where $\mathbf{D}$ is the electric flux density, $\mathbf{J}$ is the electric current density, and ρ_v is the electric charge density [5, 6].

1.2.1 TEM and TM mode

Consider a cylindrical cavity of radius a centered along the z axis as shown in Figure 1.1 [7]. If this cavity is assumed to be a perfect conductor, then according to Maxwell's equations it must satisfy the boundary conditions

$$\hat{n} \times \mathbf{E} = 0,\ \hat{n} \cdot \mathbf{H} = 0 \tag{1.6}$$

where $\hat{n}$ is the unit vector normal to the surface of the conductor [8]. The traveling wave solutions for the electric and magnetic fields will have the form

$$\begin{aligned} \mathbf{E} &= \mathbf{E}(\rho, \phi) e^{i(\omega t - k_g z)} \\ \mathbf{H} &= \mathbf{H}(\rho, \phi) e^{i(\omega t - k_g z)} \end{aligned} \tag{1.7}$$

where ω is the angular frequency and k_g is the wave number for the wave guide.

The wave equation for this cylindrical waveguide can be written as

$$\nabla_\perp^2 + (k^2 - k_g^2) \begin{Bmatrix} \mathbf{E} \\ \mathbf{H} \end{Bmatrix} = 0 \tag{1.8}$$

where $\nabla_\perp^2 = \nabla^2 - \frac{\partial^2}{\partial z^2}$, c is the speed of light, and $k^2 = \omega^2/c^2$ is the free-space wave number. By introducing a new variable $k_c^2 = k^2 - k_g^2$ and taking the Laplacian, equation 1.8 can be re-written as

$$\begin{aligned} \frac{1}{\rho}\frac{\partial}{\partial\rho}\left(\rho\frac{\partial \mathbf{E}}{\partial\rho}\right) + \frac{1}{\rho^2}\frac{\partial^2\mathbf{E}}{\partial\phi} + k_c^2\mathbf{E} = 0 \\ \frac{1}{\rho}\frac{\partial}{\partial\rho}\left(\rho\frac{\partial \mathbf{H}}{\partial\rho}\right) + \frac{1}{\rho^2}\frac{\partial^2\mathbf{H}}{\partial\phi} + k_c^2\mathbf{H} = 0. \end{aligned} \tag{1.9}$$

Equation 1.9 describes the transverse components of the waveguide, while the longitudinal components E_z and H_z can be described by the following equation:

$$\begin{aligned} \frac{\partial^2 E_z}{\partial z^2} = -k_g^2 E_z \\ \frac{\partial^2 H_z}{\partial z^2} = -k_g^2 H_z \end{aligned} \tag{1.10}$$

where E_z and H_z are independent of each other.

The solutions to equations 1.9 and 1.10 yield two modes which are called the Transverse Electric (TE) and Transverse Magnetic (TM) modes. For TE modes, the **H** field has a longitudinal component and the **E** field only has a transverse component ($\mathrm{E}_z = 0$ and $\mathrm{H}_z \neq 0$). For TM modes the **H** field is transverse everywhere while the **E** field has a longitudinal component ($\mathrm{H}_z = 0$ and $\mathrm{E}_z \neq 0$). The different TM modes are classified using the nomenclature TM_{mnp}, where the indices m, n, and p represent the number of sign changes that the electric field undergoes in the ϕ, ρ, and z directions, respectively [6, 8].

In the case that both E_z and H_z are zero, then the transverse components of **E** and **H** must also be zero, or $k_c^2 = k^2 - k_g^2 = 0$. This solution is called the transverse electromagnetic mode (TEM) [6].

1.2.2 Pill-box Cavity

The cylindrical pill-box shaped cavity shown in Figure 1.1 can be solved analytically for its RF field distribution. Typically the TM mode is used for acceleration since its electric field has a longitudinal component.

For a pill-box cavity of radius R and height h, the tangential components of the electric field must vanish at the cavity walls; $E_\rho = E_\phi = 0$ for $z = 0$ and $z = h$. For the TM mode of a pill-box cavity, the general solutions for the field components are [9]

$$\begin{aligned} E_z &= E_0 J_m\left(\frac{x_{mn}\rho}{R}\right)\cos(m\phi)\cos(p\pi z/h)\exp[i\omega t] \\ E_\rho &= \frac{p\pi}{h}\frac{R}{x_{mn}}E_0 J_m'\left(\frac{x_{mn}\rho}{R}\right)\cos(m\phi)\sin(p\pi z/h)\exp[i\omega t] \\ E_\phi &= -\frac{p\pi}{h}\frac{mR^2}{x_{mn}^2\rho}E_0 J_m\left(\frac{x_{mn}\rho}{R}\right)\sin(m\phi)\sin(p\pi z/h)\exp[i\omega t] \\ H_z &= 0 \\ H_\rho &= -i\omega\frac{mR^2}{x_{mn}^2\rho c^2}E_0 J_m\left(\frac{x_{mn}\rho}{R}\right)\sin(m\phi)\cos(p\pi z/h)\exp[i\omega t] \\ H_\phi &= -i\omega\frac{R}{x_{mn}c^2}E_0 J_m'\left(\frac{x_{mn}\rho}{R}\right)\cos(m\phi)\cos(p\pi z/h)\exp[i\omega t]. \end{aligned} \tag{1.11}$$

J_m is the m-th Bessel funciton, J_m' is its derivative, and x_{mn} is the n-th root of either function. The angular resonant frequency of the cavity is ω.

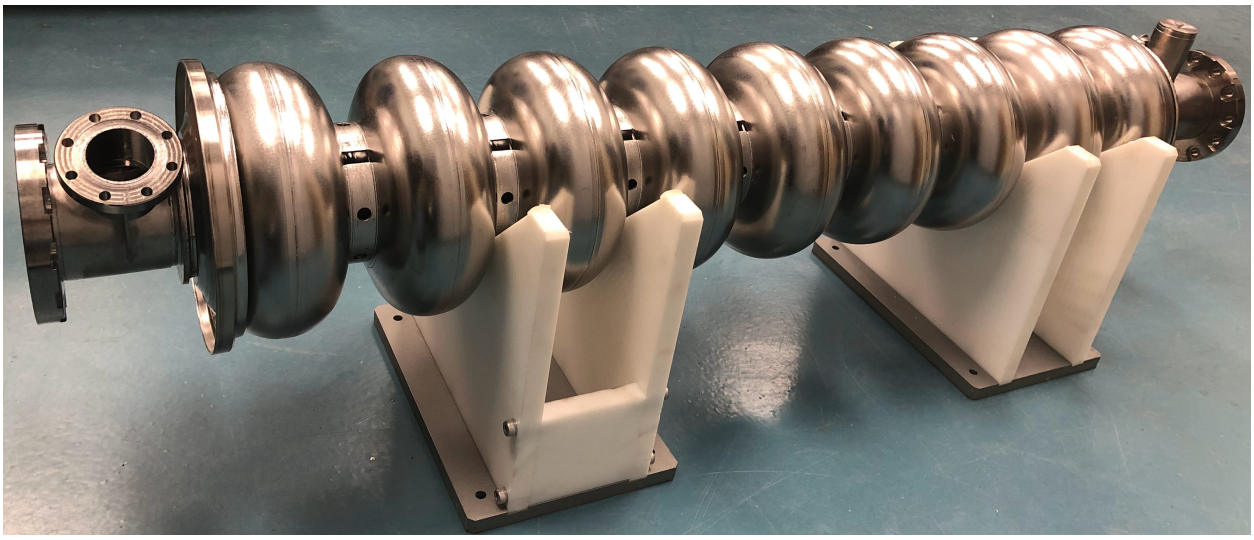

Figure 1.2: Nine cell 1.3 GHz elliptical cavity.

1.2.3 Elliptical Cavities

One commonly used type of SRF cavity is an elliptical cavity. These cavities can be composed of different numbers of elliptical-shaped cells. A nine-cell elliptical cavity is shown in Figure 1.2. Elliptical cavities are similar to pill-box shaped cavities operating in the TM010 mode with the main difference being that elliptical cavities have rounded edges and corners.

Elliptical cavities are one of the most commonly used shapes for superconducting cavities for high velocity particles due to their low peak surface field to accelerating gradient ratios.

Single cell elliptical cavities are mostly used as an accelerator physics research tool. Some of the advantages of single cell over multi-cell elliptical cavities are that their cleaning and preparation is less demanding. Multi-cell elliptical cavities are typically preferred for acceleration due to their lower cost per unit length [10]. Single cell elliptical cavities can be used as a research tool to optimize the cavity shape and design that provides the most efficient acceleration [11].

1.2.4 Coaxial Cavities

Another possible shape for SRF cavities, which will be the focus of this thesis, is the coaxial cavity. The basic geometry of a coaxial cavity consists of conducting end walls on a coaxial line with an inner and outer conductor as shown in Figure 1.3. For this type of cavity, resonance can occur for TEM modes when the boundary condition of $E_r = 0$ at both ends of the cavity is satisfied. For this to occur, the frequency of the cavity must be equal to $f = pc/2h$ where c is the speed of light and $p = 1, 2, 3....$ Hence, the height of the cavity must be $h = pc/2f$ and the resonant frequency of the cavity is determined by its height. This type of cavity is called a half wave resonator (HWR), and its lowest mode corresponds to $p = 1$ [9].

For a HWR, the non-zero electric and magnetic fields are

$$\begin{aligned} E_\rho &= -2i\sqrt{\tfrac{\mu_0}{\epsilon_0}}\tfrac{I_0}{2\pi\rho}\sin(p\pi z/h)\exp[i\omega t] \\ H_\phi &= \tfrac{I_0}{\pi\rho}\cos(p\pi z/h)\exp[i\omega t] \end{aligned} \tag{1.12}$$

where $\omega = \frac{p\pi c}{h} = 2\pi f$. The voltage on the inner conductor can be found by integrating the radial electric field between the inner and outer conductors

$$V = \int_a^b E_\rho d\rho = \sqrt{\frac{\mu_0}{\epsilon_0}}\frac{I_0}{\pi}\ln\left(\frac{b}{a}\right)\sin(p\pi z/h)\exp[i\omega t] \tag{1.13}$$

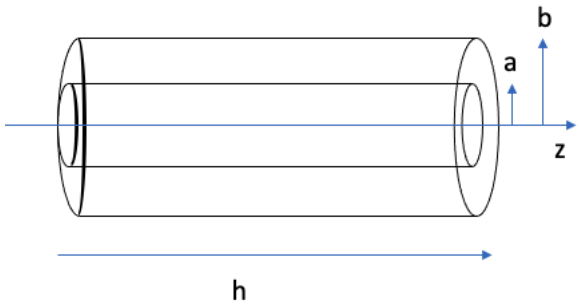

Figure 1.3: Sketch of a coaxial cavity.

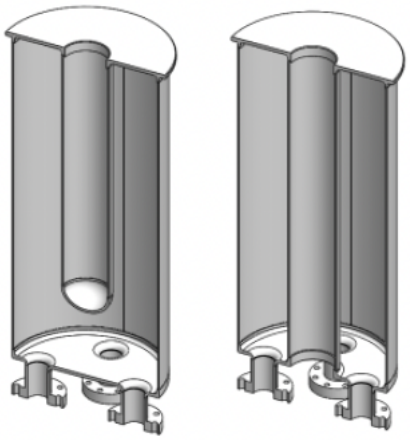

Figure 1.4: Cut out view of QWR (left) and HWR (right)

where a and b are the radii of the inner and outer conductors, respectively [9]. A HWR can be used to accelerate charged particles by placing beam ports through the inner and outer conductors in the center of the cavity. The height of the beam port should be $z = h/2$ so that the voltage and electric fields are at a maximum.

When a charged particle travels through the two gaps of the HWR, it will see an accelerating field on either side between the inner and outer conductor, and no field when it is inside the inner conductor. For efficient acceleration, the accelerating field should reverse sign when the particle is within the inner conductor.

Another type of coaxial cavity is the Quarter Wave Resonator (QWR). In this cavity the inner conductor is open at one end and terminated with part of the cavity material at the other end, shortening its length. The QWR has a resonant frequency of approximately $f = (1 + 2p)c/(4h)$ where $p = 0, 1, 2...$ [9]. As with the HWR, the resonant frequencies of the QWR are also determined by the cavity height h. The lowest accelerating mode of a QWR corresponds to $p = 0$. Figure 1.4 shows a cut out of a HWR and QWR [12].

In a QWR the electric field used for acceleration exists between the inner and outer conductor. Beam ports are typically placed closer to the capacitive end of the QWR where the radial electric field is high. For a QWR, the exact resonance wavelengths cannot be solved analytically like those of the HWR [13]. Modern QWR's (and most other rf cavities) are designed using numerical simulation software such as CST Microwave Studio [14].

1.2.5 Figures of Merit

One of the most important characteristics of an SRF cavity is the unloaded quality factor Q_0. The quality factor is defined as the ratio of the energy stored in the electromagnetic fields to the energy lost in the walls of the cavity in one RF period and is a measure of power loss in the cavity walls. This can be expressed as

$$Q_0 = \frac{\omega_0 U}{P_c}, \tag{1.14}$$

where ω_0 is the angular frequency of the accelerating mode, U is the stored energy in the cavity, and P_c is the power dissipated in the cavity walls.

The Q_0 is a measurement of a cavities' energy efficiency. A higher Q_0 means that the cavity will be more energy efficient with lower operating costs. One would like to make the quality factor as high as possible in order to cut down on capital and operation costs of particle accelerators.

The time averaged stored energy in the cavity is given by

$$U = \frac{1}{2}\mu_0 \int_V |\mathbf{H}|^2 dv = \frac{1}{2}\epsilon_0 \int_V |\mathbf{E}|^2 dv. \tag{1.15}$$

These integrals of the magnetic and electric fields over the volume of the cavity have this relation since the cavity energy oscillates between its electric and magnetic field.

The walls of a cavity have current flowing through them which dissipates energy due to the cavities' finite surface resistance. This power loss can be written as

$$P_c = \frac{1}{2}\int_S R_s |\mathbf{H}|^2 ds \tag{1.16}$$

where R_s is the cavity surface resistance, and the integral is taken over the cavity surface.

By combining equations 1.14, 1.15 and 1.16 the quality factor can be written as

$$Q_0 = \frac{\omega_0 \mu_0 \int_V |\mathbf{H}|^2 dv}{\int_S R_s |\mathbf{H}|^2 ds}. \tag{1.17}$$

If the surface resistance R_s is uniform it can be moved outside the integral in equation 1.17. Then Q_0 can be written as

$$Q_0 = \frac{G}{R_s^*}, \tag{1.18}$$

where G is a frequently used constant known as the geometry constant defined as

$$G = \frac{\omega_0 \mu_0 \int_V |\mathbf{H}|^2 dv}{\int_S |\mathbf{H}|^2 ds}. \tag{1.19}$$

Equation 1.18 is an approximation of the quality factor that assumes a constant surface resistance [8]. However, this approximation is not always accurate in which case the surface resistance must be corrected. This will be discussed later in Section 3.1.1.

Another important Figure of merit is the accelerating voltage, V_{acc}. This is defined as the quotient of the maximum amount of energy that a charged particle can gain as it traverses the cavity, and the charge of the particle. The average accelerating electric field can then be defined as

$$E_{acc} = V_{acc}/l \tag{1.20}$$

where l is equal to $\beta\lambda$ for a two gap structure.

The highest electric and magnetic surface fields that a cavity can maintain are called E_{pk} and H_{pk}, respectively. H_{pk} needs to stay below a certain threshold or the cavity will quench. During a quench at least part of the cavity will absorb the stored energy within the cavity and become normal conducting (see Section 1.3). It is important that E_{pk} is not too high or the cavity will experience field emissions. Field emissions occur when electrons are emitted from the cavity surface, causing a significant decrease in quality factor [8].

1.3 Superconductivity

Some elements such as niobium can be cooled down to temperatures so low that they become superconducting. When a conducting material becomes a superconductor, its DC electrical resistance vanishes and the material will repel any magnetic fields. DC current can flow through superconductors without dissipating any energy, which gives them zero surface resistance. RF currents however are still dissipative with an rf surface resistance, but one that is very small compared to normal conducting materials. There are two types of superconductors called type I and type II. Modern superconducting radio frequency (SRF) cavities are made of niobium, which is a type II superconductor. An advantage of using niobium is that it becomes superconducting at the high temperature of 9.2 K, which is the highest critical temperature of all the known elements. Niobium is also relatively malleable and available.

Bardeen, Cooper, and Schrieffer came up with a theory for how superconductivity works at a microscopic level known as BCS theory. In the BCS theory, electrons become attracted to each other which leads to a redistribution of the energy levels of a superconductor in which there is a gap between the ground state and excited state energy levels [8]. This theory has been useful in predicting the rf surface resistance of superconducting niobium which can be written as

$$R_s = R_{BCS} + R_0 \tag{1.21}$$

where R_{BCS} is the rf surface resistance predicted by the BCS theory and R_0 is the temperature independent residual resistance [8]. The R_{BCS} term is dependent on the cavity temperature and can be approximated [15] as

$$R_{BCS} = \frac{\mu_0^2 \omega^2 \lambda^3 \Delta}{\rho_s k_B T} \ln\left(\frac{9 k_B T}{2\hbar\omega}\right) \exp\left(\frac{-\Delta}{k_B T}\right) \tag{1.22}$$

where μ_0 is the vacuum permeability, ω is the cavities' resonance frequency, λ is the London penetration depth, Δ is the energy gap, ρ_s is the normal state resistivity, k_B is the Boltzmann constant, T is the temperature of the cavity, and $\hbar$ is the reduced Plank constant.

Below a temperature of 9.2 Kelvin, niobium will become superconducting. Under ideal conditions, when a niobium cavity is cooled below its superconducting transition temperature, any magnetic flux present in the cavity would be abruptly expelled. This phenomenon is called the Meissner effect [8].

Type I superconductors have a critical temperature (T_c) below which they will become superconducting. The superconducting phase is also dependent on the ambient magnetic field due to the Meissner effect. The left graph of Figure 1.5 is a phase diagram showing that below certain magnetic fields ($H_c(T)$) and temperatures (T_c) certain materials can enter the superconducting or Meissner state. When a superconducting material is cooled below its critical temperature in the presence of an external magnetic field, any magnetic flux within the material will be abruptly expelled. When a material is in a Meissner state, an externally applied magnetic field that is less than H_c cannot penetrate the material. When a material becomes superconducting screening currents appear on its surface which cancel the magnetic field inside the material [8]. Figure 1.6 depicts full flux expulsion (Meissner effect) of a superconductor.

Type II superconductors have two critical magnetic fields, a lower (H_{c1}) and upper (H_{c2}) critical field. If the material in a type II superconductor is below the critical temperature and the lower magnetic field, the material will be in the Meissner state, that is, it will be fully superconducting with $\mathbf{B} = 0$. If the material's magnetic field is between the lower and upper critical magnetic fields, it will be in a mixed state in which some of the material is superconducting while other parts of the material contain normal conducting

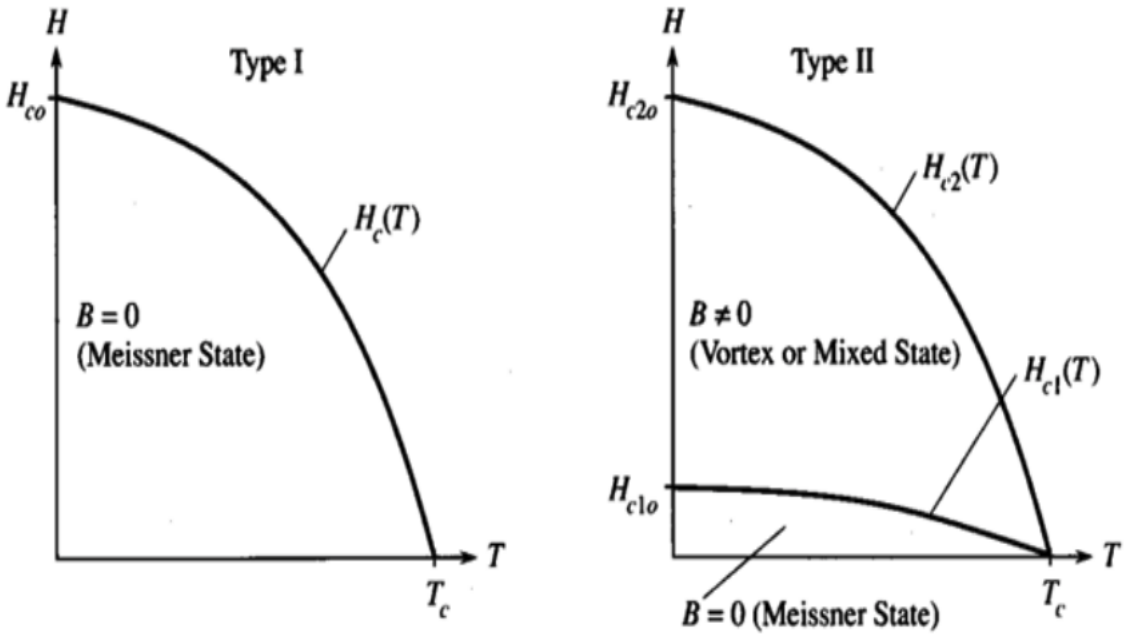

Figure 1.5: Phase diagram for type I (left) and type II (right) superconductors. Image courtesy of [16].

magnetic field vortices. For the superconducting parts it is energetically favourable for magnetic fluxoids and vortices of screening currents to enter the material, bringing the material to a mixed state. A phase diagram for a type II superconductor is shown in the right graph of Figure 1.5 [16].

This small rf resistance of SRF cavities can be explained using a two-fluid model. Below a certain temperature T_c some of the electrons in a superconducting material will join together to form Cooper pairs. Cooper pairs are pairs of electrons that condense to form an entity which can be regarded as a new particle with twice the mass and charge of a single electron. The Cooper pairs can move without friction, and thus form a supercurrent that flows without resistance. The electrons that are unpaired form a normal current, which flows in parallel to the supercurrent [8]. This is why SRF cavities have a very small surface resistance and finite Q_0 even below T_c.

As shown in Section 1.2.5, the cavities' quality factor depends on the surface resistance of its material. A lower surface resistance leads to a higher quality factor. For this reason cavities are made to be superconducting so that the surface resistance is as low as possible. Table 1.1 shows a comparison between parameters for normal conducting and superconducting pill-box cavities of the same size and frequency [17]. A notable parameter in this Table is the power dissipation, which differs by over six orders of magnitude between the normal and superconducting cavities, making the superconducting cavity much more energy efficient.

Real SRF cavities can undergo an incomplete flux expulsion when they are cooled down below superconducting temperatures. In this case some magnetic flux is trapped inside the cavity. One possible cause of flux trapping are impurities and defects in the niobium. Another possible cause is flux pinning, in which some of the magnetic flux is pinned to a certain location on the cavity because it is energetically unfavorable for the flux to move [8]. It is preferable to avoid flux trapping, because this will cause the cavity to have an increased surface resistance and decreased quality factor, making it less energy efficient. This is because trapped magnetic vortices have normal conducting cores which interact strongly with the rf electric fields which flow through the normal conducting regions generating heat, which needs to be cooled with liquid helium [8]. Figure 1.7 shows a diagram of these normal conducting vortices trapped in a superconductor.

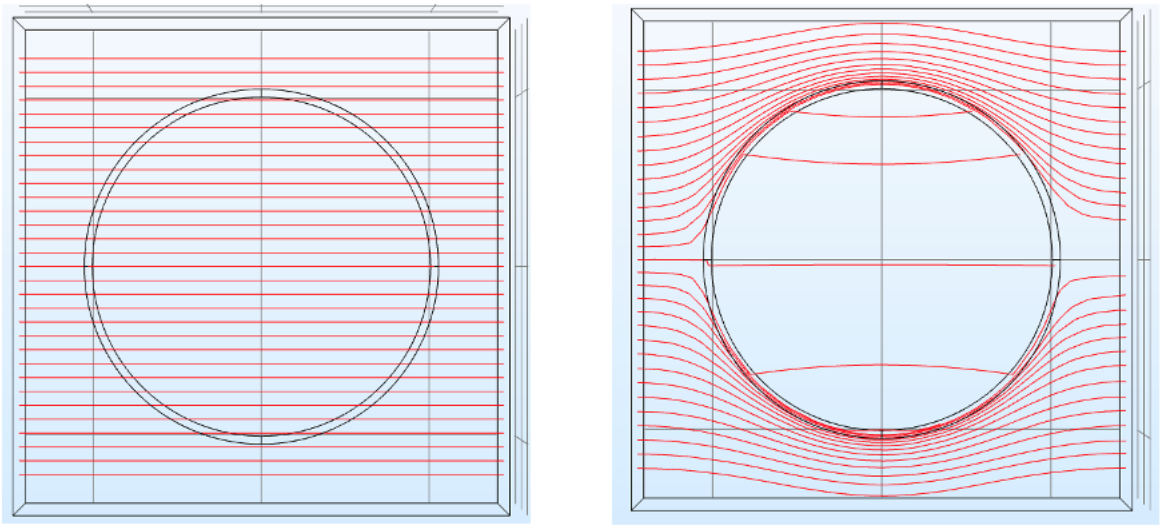

Figure 1.6: Diagram of a near perfect Meissner effect. Red horizontal lines represent magnetic flux. This image was made using COMSOL Multiphysics ®.

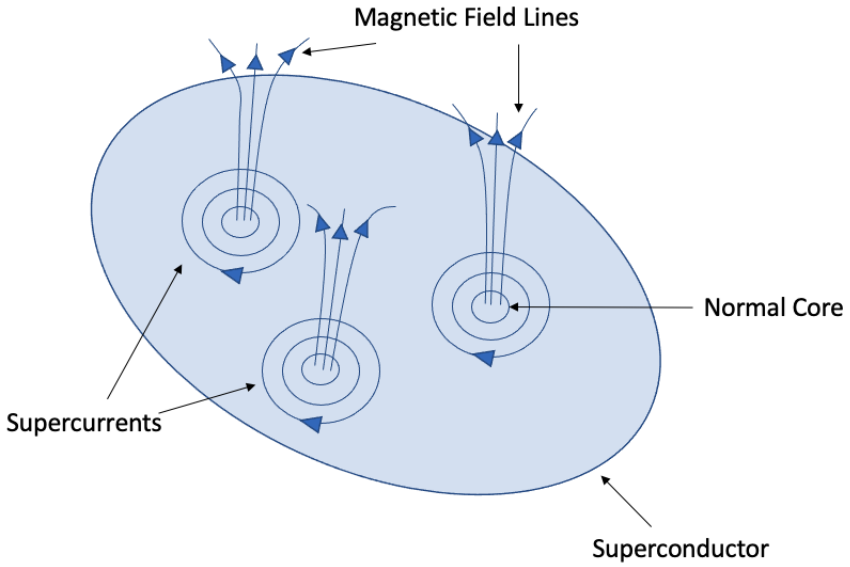

Figure 1.7: Normal conducting vortices and their magnetic flux lines trapped inside a superconductor.

Parameter	Normal Conducting	Superconducting
Length (cm)	10	10
Radius (cm)	7.65	7.65
Frequency (MHz)	1500	1500
Voltage (MV)	1	1
Temperature (K)	300	2
Power Dissipation (W)	198,000	0.4
$R_s(\Omega)$	0.01	2 x 10^{-8}
Q_0	25,500	1.3 x 10^{10}

Table 1.1: Comparison between parameters for a normal conducting and superconducting pill-box cavity. Table values courtesy of [17].

An approximation of the impact of the trapped flux to SRF performance can be derived as follows. If a magnetic field H_{ext} is applied over an area A which is broken up into N fluxoids each with a flux quantum of Φ_0, then H_{ext} can be written as [8]

$$H_{ext} = \frac{N\Phi_0}{A}. \tag{1.23}$$

The contribution to the residual surface resistance from N trapped fluxoids is

$$R_{mag} = N\frac{\pi\zeta_0^2}{A}R_n = \frac{H_{ext}\pi\zeta_0^2\mu_0 R_n}{\Phi_0} \tag{1.24}$$

where ζ_0 is the approximate size of the normal conducting core of the fluxoid, and R_n is the normal-conducting resistance of the material. For Type II superconductors, the upper critical magnetic field can be expressed as

$$H_{c2} = \frac{\Phi_0}{2\pi\mu_0\zeta_0^2}. \tag{1.25}$$

Using these equations R_{mag} can be re-written as

$$R_{mag} = \frac{H_{ext}R_n}{2H_{c2}}. \tag{1.26}$$

A related quantity, magnetic sensitivity, is a measure of how sensitive the surface resistance of a material is to an external magnetic field. The magnetic sensitivity S_{mag} is formulated as

$$S_{mag} = \frac{R_n}{2H_{c2}}. \tag{1.27}$$

1.4 State of the Art

The motivation for this thesis is to study flux trapping in HWR and QWR cavities. The following is a summary of recent developments in flux trapping research.

A study was done by Romanenko [18] to explore the effects of cool-down speeds on flux expulsion for 1.3 GHz TESLA bare niobium cavities. Romanenko found that a slow cool-down leads to higher residual resistance than a fast cool-down due to larger flux trapping (and smaller flux expulsion). The initial results of this experiment are shown in Figure 1.8 in which a single-cell single crystal electropolished cavity undergoes multiple cool-downs through T_c at different speeds. Figure 1.8a on the left shows the residual resistances as a function of accelerating gradient for the different cool-downs while Figure 1.8b on the right shows the corresponding magnetic field measurements at the cavity equator as a function of temperature during the cool-down. The residual resistances are lower for fast cool-downs, and the magnetic field data shows that this is because more of the ambient magnetic field is expelled during the fast cool-downs. Similar results

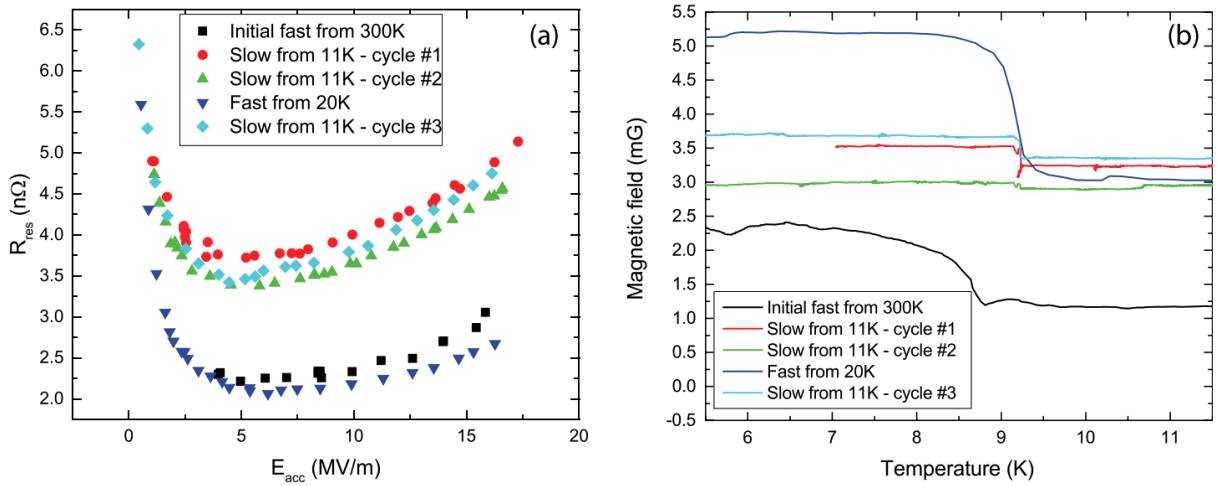

Figure 1.8: Left (a): Residual resistances as a single-cell single crystal after cool-down cycles of different speeds. Right (b): Corresponding magnetic field data measured at the cavity equator during the cool-downs. Figure courtesy of [18].

were obtained for nitrogen doped 9-cell and 1-cell cavities, and 120 ℃ baked and electropolished 9-cell and 1-cell cavities.

A demonstration of complete flux expulsion has been reported by Romanenko [19]. In the study large thermal gradients were created at the NC-SC front during the cool-down. This experiment lead to the achievement of nearly full flux expulsion with a record high quality factor of $Q > 2 \times 10^{11}$. It was found that spatial temperature gradients had a larger effect on flux expulsion than cool-down speed. The spatial temperature gradients needed for efficient flux expulsion were found to be about 0.1-0.2 K/cm.

In this experiment 1.3 GHz TESLA shaped cavities were cooled down in ambient magnetic fields ranging from 2 to 190 mG and from starting temperatures ranging from 12 to 300 K. Measurements of the quality factor and accelerating gradient were done at 2 or 1.5 K. The first result showed that quality factors of up to 2×10^{11} could be achieved for ambient magnetic fields ranging from 2 to 23 mG and starting temperatures of 53 or 300 K. There was little difference in quality factor for the different ambient magnetic fields as shown in Figure 1.9.

Next the temperature distribution along the cavity was changed during cooling cycles while keeping the ambient magnetic field fixed at 10 mG. These results are shown in Figure 1.10 where the residual resistance is plotted as a function of the difference between the temperature of the top iris (T_1) and equator (T_2) measured when the equator reaches T_c. The inner plot in Figure 1.10 shows the corresponding quality factor values. These results are also plotted in Figure 1.11 as a function of cooling rate dT_2/dt in K/min when T_2 reaches T_c. These results show that having a higher temperature gradient at the NC-SC front leads to higher, and in some cases nearly full flux expulsion. The cooling rate does not have any apparent effect on flux expulsion. More recent studies have found that the motion of magnetic flux vortices is affected by temperature gradients, as the temperature gradients help overcome the pinning force [20].

In 2016 further studies were done by Posen [21] on flux expulsion of single-cell 1.3 GHz elliptical niobium cavities. That study analyzed flux expulsion as a function of thermal gradient and cavity preparation. RF measurements were performed on the cavities after they underwent 120, 800, and 1000 ℃ bakes. The cavity that underwent the 1000 ℃ bake showed substantial improvement in quality factor after the heat treatment. When the cavities were being baked, a sample of niobium was baked along with them. After the bake the sample was observed under an electron microscope and compared to another sample that was not baked. The images showed that the grains of niobium crystals increased in size after the heat treatments. The cavities that had the heat treatment also showed an improvement in flux expulsion. This suggested that the bulk structure is a source of flux trapping during the cool-down. If grain boundaries are the locations of flux

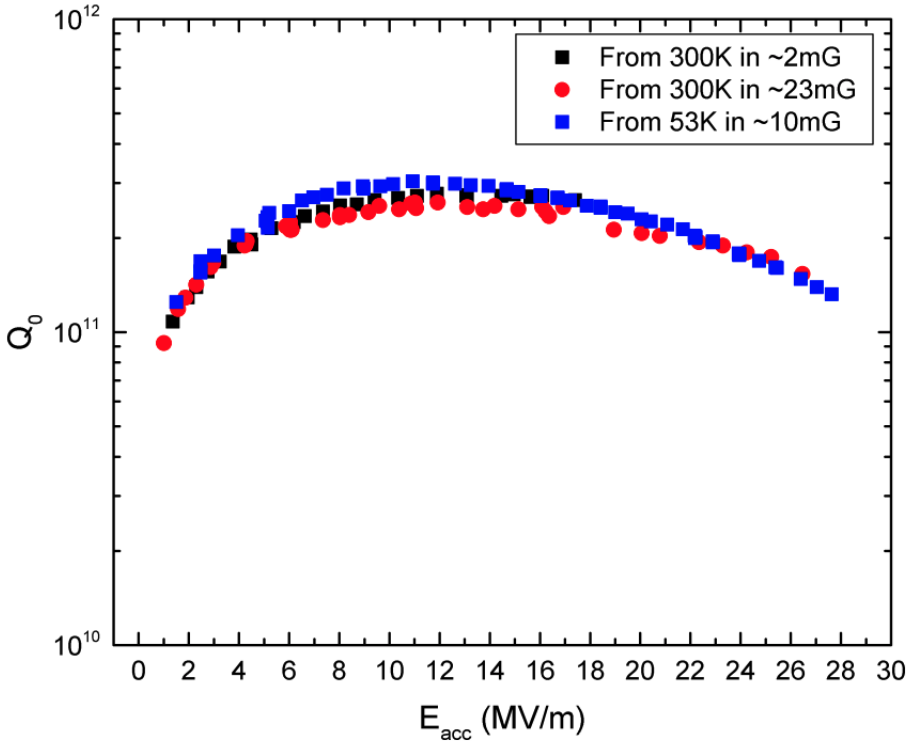

Figure 1.9: Q curves at a temperature of 2 K for three different cool-downs with different applied magnetic fields. Figure courtesy of [19].

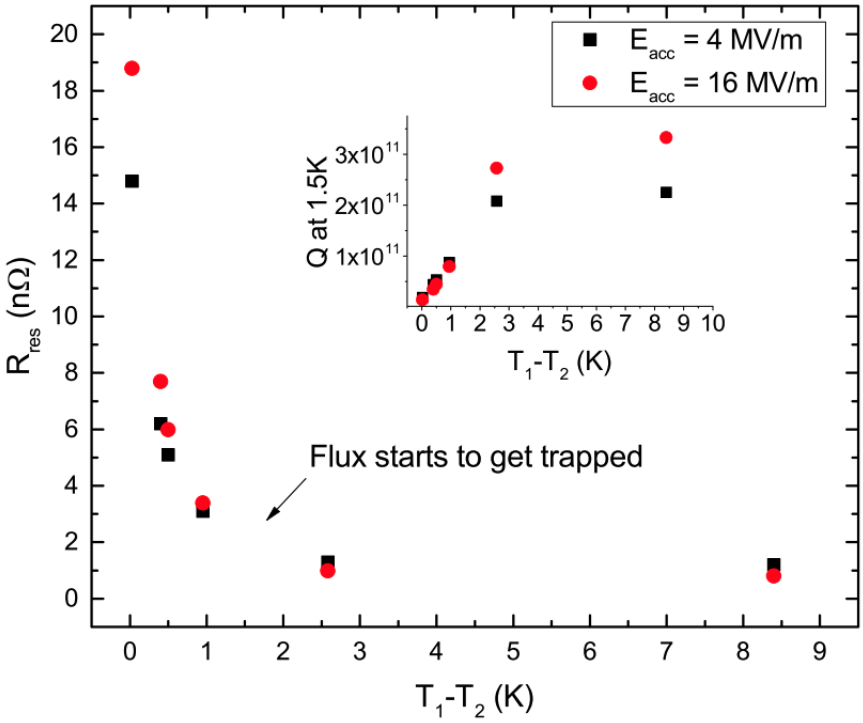

Figure 1.10: Residual resistance at 1.5 K as a function of the temperature gradient measured when the equator reaches T_c. The inner plot shows the corresponding quality factor values. Figure courtesy of [19].

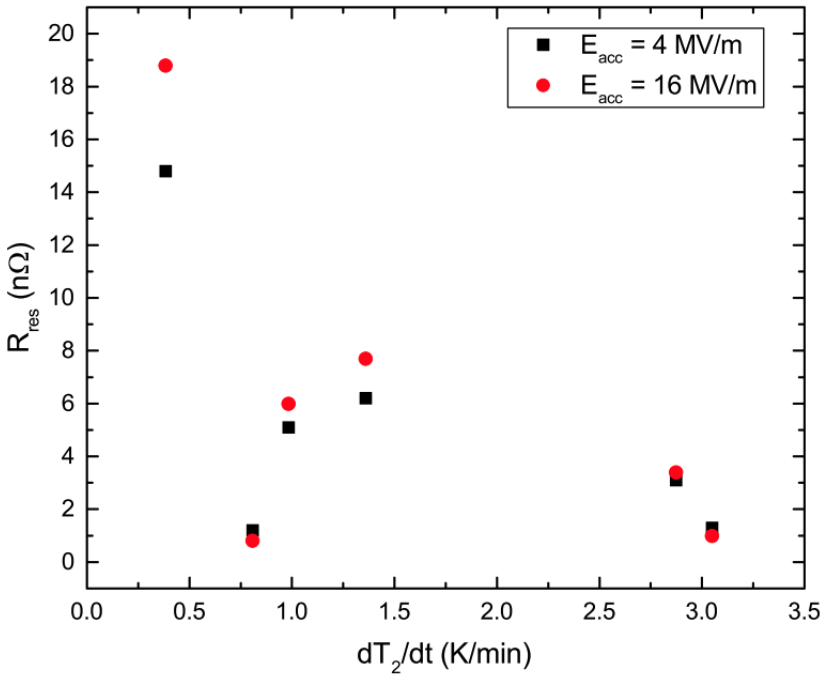

Figure 1.11: Residual resistance at 1.5 K as a function of the cooling rate measured when the equator reached T_c. Figure courtesy of [19].

pinning, then decreasing the number of grain boundaries in the cavity would decrease the amount of flux trapped in the cavity.

The flux expulsion of the cavities in the study was also affected by the thermal gradient. A model was developed to predict the quality factor as a function of gradient. The model was based on measurements of flux expulsion as a function of temperature difference from the bottom to the top of the cavity cell as the cavity passes through T_c during cool-down. An assumption of this model is that the surface resistance arising from flux trapping is added to a certain baseline resistance. The model showed an increase in quality factor with a larger temperature gradient.

A following study was performed by Posen [22] in 2019. The cavities tested were 1.3 GHz elliptical nine-cell cavities for the Linac Coherent Light Source II (LCLS-II) accelerator. In this experiment the authors sought to achieve near complete flux expulsion in their SRF cavities through heat treatments and by cooling the cavities through their superconducting transition with a spatial temperature gradient on the surface.

It was found that heat treatments of at least 900-1000 °C dramatically increased the flux expulsion efficiency and the quality factor of the cavities. The flux expulsion decreased due to a reduction of flux pinning centers through partial annealing. This was not always the case for cavities treated with temperatures of about 800 °C. Applying a large thermal gradient to the cavities during cool-down also improved flux expulsion. These cavities were able to achieve quality factors exceeding about 3×10^{10} under the operating conditions of LCLS-II.

Martinello [23] has done some flux expulsion experiments on horizontally cooled single-cell elliptical cavities with different magnetic field orientations. In this experiment the cavity underwent several fast cool-downs with an applied magnetic field in either the orthogonal or axial direction with respect to the cavity. Figure 1.12 taken from [23] shows the two applied magnetic field orientations used in the experiment.

When the cavity is oriented horizontally with respect to the cryostat axis, the NC-SC front moves along the cavities' equator. Therefore, the final escape location for magnetic flux is at the cavity equator, rather than the beam tube as it is with vertical cool-downs. In elliptical cavities the peak magnetic field is typically located near the equator. When magnetic flux converges near the equator it can lead to magnetic vortices

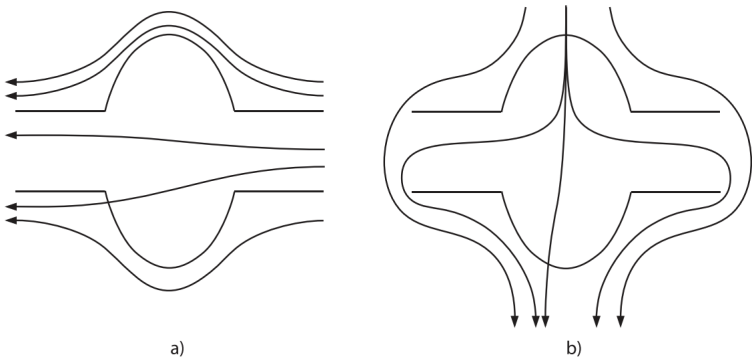

Figure 1.12: Diagram showing the magnetic field lines applied to a singe-cell elliptical cavity in the axial (a) and orthogonal (b) direction. Figure courtesy of [23].

which will contribute more power loss from the normal conducting regions due to the high magnetic fields in that area. One important finding was that with the horizontal cool-down orientation, the temperature gradient of the NC-SC front was decreased as it approached the top of the cavity during the final stage of the cool-down. This leads to more trapped flux in that region since there is a relatively high surface magnetic field in that area.

Another notable finding of this experiment was the difference in cavity performance between the different applied magnetic field directions. When the applied field is perpendicular to the cavity axis (as in Figure 1.12b) during the cool-down to superconducting temperatures, some of the flux lines can end up being squeezed to the cavity equator, where it is not energetically favourable for the flux to escape through the cavity walls. This can lead to an incomplete Meissner effect. The results of this experiment showed that the cavity had a lower quality factor after being cooled with an applied field in the orthogonal direction.

In 2018 a study was done on the frequency dependence of flux trapping in SRF cavities [24]. This study looked at how the sensitivity to trapped flux can depend on the cavity frequency by testing elliptical cavities operating at the different frequencies: 650 MHz, 1.3 GHz, 2.6 GHz, and 3.9 GHz. These cavities also had different surface treatments: electropolished (EP'd), buffer chemical polished (BCP'd), 120 ℃ baked, and Nitrogen doped. Figure 1.13 shows some results from this experiment in which the sensitivity increases with cavity frequency and accelerating gradient for every cavity treatment. The dependence on frequency was much greater for Nitrogen doped cavities as shown in graph c).

This study also found that the magnetic sensitivity has a non-monotonic dependence on electron mean-free-path (l) for 1.3 GHz cavities. The higher magnetic sensitivity values were correlated to intermediate values of mean-free-path. The cause of this mean-free-path dependence is thought to be caused by the competing influences of flux pinning and flux flow dynamics of the rf field for the smaller and larger values of the mean-free-path, respectively.

Another study by Martinello compared magnetic sensitivities of 1.3 GHz cavities after different surface treatments [25]. This study also found that intermediate mean-free-path values corresponded to the highest magnetic sensitivities. Of all the surface treatments used in this study, the 120 ℃ bake resulted in the the lowest magnetic sensitivity and mean-free-path. The cavity treatment with the next-lowest magnetic sensitivity was electro-polishing, and the cavity with this surface treatment had the highest mean-free-path. Other cavities underwent nitrogen doping with varying times of nitrogen exposure. These cavities had intermediate mean-free-path values and higher magnetic sensitivities.

The mean free path of a material is a function of the level of its impurities. For a high concentration of impurities the mean free path is low and for a low concentration of impurities the mean free path is high. Bakes at 120 ℃ produce low mean free paths while doped surfaces tend to produce mean free paths of around 60-70 nm which correspond to high magnetic sensitivities. The surface resistance due to trapped flux vortices increases as a function of the mean free path when the mean free path is low. For higher mean free paths, the surface resistance due to trapped flux vortices decreases as a function of the mean free path [20].

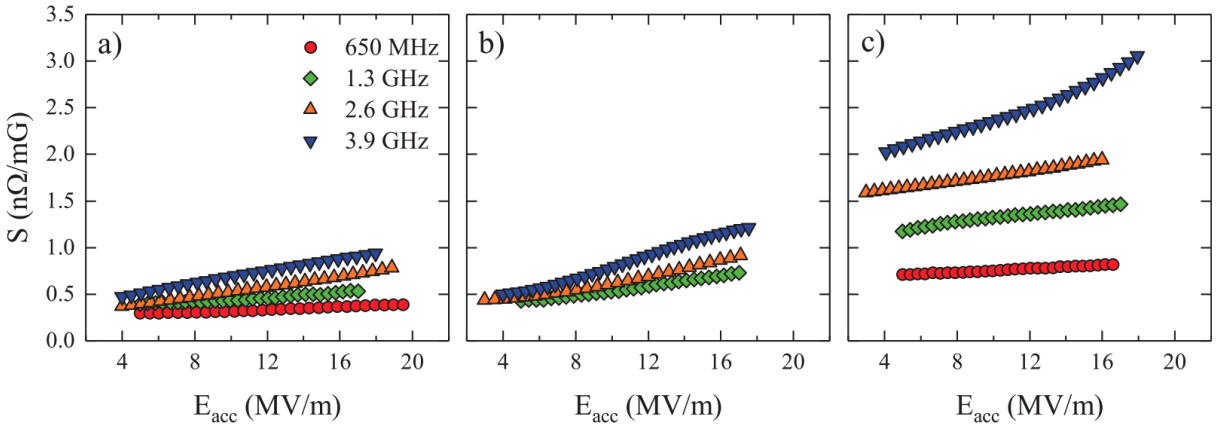

Figure 1.13: Sensitivity as a function of accelerating gradient. Graph a: Cavity treated with 120 ℃ bake. Graph b: Cavity treated with EP and BCP. Graph c: Cavity treated with Nitrogen doping. Figure courtesy of [24].

Most flux trapping studies have involved elliptical cavities. One of the most recent flux trapping studies was done in 2021 by Longuevergne and Miyazaki [26]. This experiment used three different cavity geometries: a QWR operating at a frequency of 88 MHz, a double-spoke resonator (DSR) operating at 352 MHz, and a single-spoke resonator (SSR) also operating at 352 MHz. Longuevergne and Miyazaki proposed a model in which the residual resistance of an SRF cavity (see 1.21) can be written as

$$R_{res} = R_0 + R_{mag} \tag{1.28}$$

where R_0 is caused by material imperfections and R_{mag} can be written as

$$R_{mag} = \mu_0 \eta_{mag} \cdot S_{mag} \cdot H_{res} \tag{1.29}$$

where η_{mag} is a dimensionless flux trapping efficiency, S_{mag} is the magnetic sensitivity with units of $n\Omega/\mu T$, and H_{res} is the residual ambient magnetic field. The aim of this study was to investigate the role of cavity geometry on trapped flux. The magnetic sensitivity is defined as the amount of surface resistance caused by trapped magnetic field [24].

In their experiment, Longuevergne and Miyazaki were able to decouple S_{mag} and η_{mag} by trapping nearly 100 % of the flux and satisfying the condition $\eta_{mag} \sim 1$. The results showed a strong dependence on geometry for S_{mag}. A new method was developed to calculate S_{mag} while taking into account geometrical effects. To do this Longuevergne and Miyazaki identified two possible flux trapping cases. In the first case, flux is trapped perpendicular to the cavity surface and S_{mag} is proportional to the square of the cosine of the polar angle θ between the rf surface and the rf current, that is, $S_{mag} \propto \cos^2\theta$. In the second case, there is no angle dependence for flux trapping. In this case, the magnetic sensitivity is

$$S_{mag} \propto \cos^2\theta + \sin^2\theta \sin^2\phi \tag{1.30}$$

where ϕ is the angle between the trapped flux projected to the rf surface and rf current. These two cases were used to calculate a new magnetic sensitivity that takes into account geometrical dependence. This new sensitivity is

$$S'_{mag} = \frac{\int_S R_{mag}(X,Y,Z) H^2_{rf}(X,Y,Z) dS}{H_{res} \int_S H^2_{rf}(X,Y,Z) dS} \tag{1.31}$$

where (X, Y, Z) are Cartesian coordinates, and H_{rf} is the local rf magnetic field [26].

Another study on the geometry of flux trapping was done by Kramer et al. [27]. This study used 1.3 GHz elliptical cavities which were cooled down repeatedly with magnetic fields applied in different directions. It was observed that the cavity had a higher surface resistance when the applied magnetic field was perpendicular to the cavity surface compared to when the field was parallel.

While most studies on flux trapping have been done on elliptical cavities, the experiment performed by Longuevergne and Miyazaki is one of the few studies done with coaxial cavities. The motivation for the experiments performed for this thesis is to improve the understanding of flux trapping in coaxial cavities.

1.5 Summary of Thesis

The thesis organization is as follows. The second chapter of this thesis discusses the materials and methods used. This chapter contains some detailed specifications on the HWR and QWR. The methods for measuring the quality factor, peak magnetic field and temperature are described. The cavity surface treatments are also discussed.

The third chapter pertains to data analysis and COMSOL simulations. The methods for synthesizing and analyzing datasets are conveyed. COMSOL simulations of superconducting HWR and QWR cavities are shown.

The fourth chapter presents the results from the coaxial cavity experiments. These include results from magnetic field measurements done using fluxgate probes. This chapter also discusses the components of the cavities' temperature dependent and temperature independent surface resistances and how these are affected by cavity surface treatments, applied magnetic fields, and peak rf fields.

One of the major findings of this research is in Section 4.2.1: Fast vs Slow Cool-down. This Section details the results of an experiment in which the QWR is cooled down to superconducting temperatures in the presence of an applied magnetic field at different cool-down speeds and temperature gradients.

Chapter 2

Equipment and Data Taking

2.1 Cavities

The experiments in this thesis were done on two coaxial SRF cavities, a HWR and a QWR. A photo of these cavities is shown in Figure 2.1 [12]. This type of cavity geometry is used in hadron linacs. The cavities used in these experiments are simplified versions of a HWR and QWR without beam ports [28]. The entirety of the cavities including the rinse ports is made from niobium in order to avoid contamination during high temperature treatments. Both cavities have four identical rinse ports on one end cap. These ports are used for rinsing the cavity, vacuum connections, and mounting the variable RF coupler and the pick up antenna.

One design goal of these cavities was to have similar ratios of peak surface magnetic and electric fields, B_{pk}/E_{pk} for each resonant mode [29]. Both cavities have identical dimensions for the rinse ports and inner and outer conductors. The diameters of the inner and outer conductors are 60 and 180 mm, respectively. The inner conductors of the cavities are straight in order to reduce field distortions in higher order modes (HOMs). The top and bottom end plates of the cavities are flat in order to eliminate mulipacting barriers at higher gradients. These design choices also made the cavity fabrication simpler.

The main body of the cavities is made of niobium with a high residual resistivity ratio. Since the bottom plate and rinse ports of the QWR are exposed to only minimal rf fields, these were made from cheaper reactor grade niobium [30]. All parts of both cavities are electron-beam welded together with no removable parts.

The cavities can be excited by a fundamental resonating mode as well as higher harmonics during the same cool-down. This can help gain insights into frequency dependent effects.

2.1.1 HWR

The geometry of the HWR is shown in Figure 2.2 [31]. The inner and outer conductors have a length of 393 mm [32]. The magnetic field distribution of the HWR is shown in Figure 2.3. The fundamental frequency of this cavity is 389 MHz. The next available TEM mode frequencies are 778, 1066, and 1555 MHz [12]. If E_{pk} and B_{pk} are expressed in units of V/m and T, respectively, then the ratio of peak electric and magnetic fields of the HWR is $E_{pk}/B_{pk} = c$ where c is the speed of light [29].

2.1.2 QWR

The geometry of the QWR is shown in Figure 2.4 [31]. The outer and inner conductors of the QWR have lengths of 405 and 325 mm, respectively [33]. The magnetic field distribution of the QWR is shown in Figure 2.5. The fundamental frequency of this cavity is 217 MHz and the next available TEM mode frequency is 648 MHz [28]. These resonant modes are affected by field distortions at the closed end of the inner conductor which generate distorted peak surface fields. The E_{pk}/B_{pk} ratio of the QWR depends on the geometry of the closed end of the inner conductor and is similar to the E_{pk}/B_{pk} ratio of the HWR. This ratio was optimized using simulations, and has a value of 0.47 (MV/m)/mT [29] for the two TEM modes under consideration.

Figure 2.1: Photo of two coaxial cavities. Photo courtesy of [12].

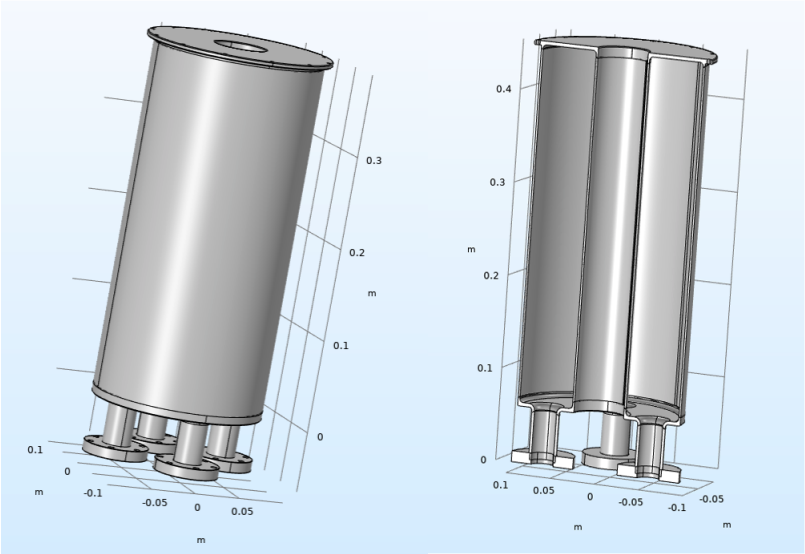

Figure 2.2: 3-Dimensional computer model of the HWR: Full cavity (left) and vertical cut-out (right). This image was made using COMSOL Multiphysics ®

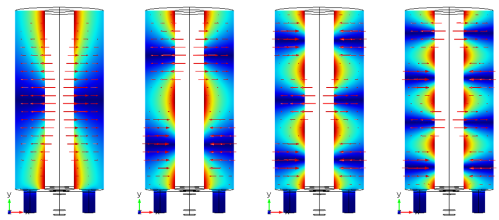

Figure 2.3: Magnetic field distribution of the coaxial HWR. Fundamental mode (left) higher resonant modes (middle and right). Figure courtesy of [12].

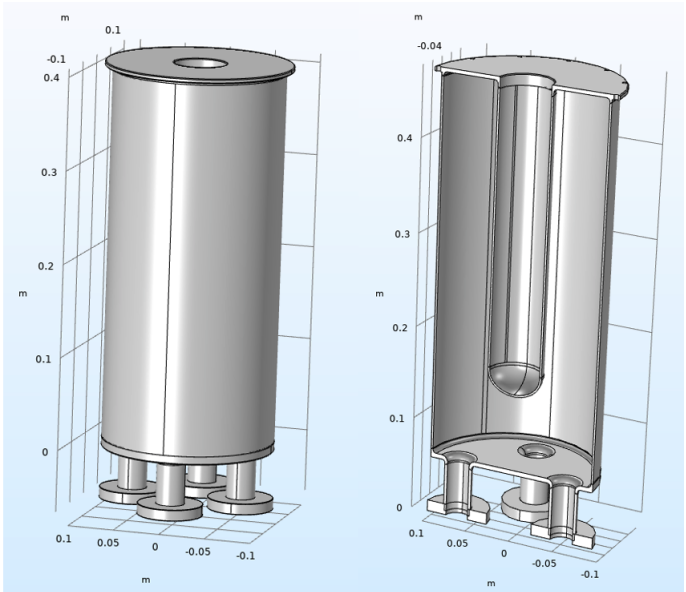

Figure 2.4: 3-Dimensional computer model of the QWR: Full cavity (left) and vertical cut-out (right). This image was made using COMSOL Multiphysics ®

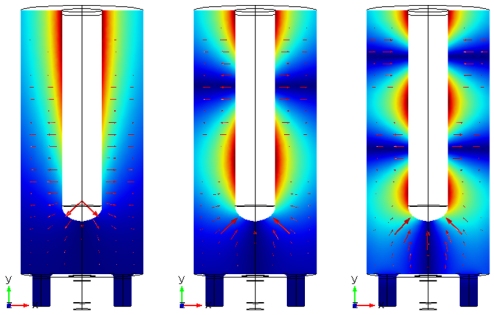

Figure 2.5: Magnetic field distribution of the coaxial QWR. Fundamental mode (left) higher resonant modes (middle and right). Figure courtesy of [12].

Table 2.1 shows some rf parameters for both the HWR and QWR in the TEM modes of interest [29]. These parameters include the resonant mode, numerically calculated values for the peak electric and magnetic field ratio, the ratio of stored energy in the cavity and the square of the peak magnetic field (U/B_{pk}^2), and the cavity geometry factor. These values have been determined using simulations.

Cavity	Frequency [MHz]	E_{pk}/B_{pk} [(MV/m)/mT]	U/B_{pk}^2 [mJ/mT^2]	G [Ω]
QWR	217	0.4796	0.4208	37.47
QWR	648	0.4679	0.4350	113.7
HWR	389	0.2975	0.4675	60.39
HWR	778	0.2981	0.4681	120.77
HWR	1166	0.2981	0.4692	181.8

Table 2.1: RF parameters for both coaxial cavities in the TEM modes of interest. Table values courtesy of [29].

2.1.3 Q Measurements

One of the most important parameters that needs to be determined during a cavity test is the unloaded quality factor of a cavity, Q_0, which is defined in Chapter 1 as

$$Q_0 = \frac{\omega_0 U}{P_c} \tag{2.1}$$

where ω_0 is the angular frequency of the cavity, U is the energy stored in the electromagnetic fields of the cavity, and P_c is the energy dissipated in the cavity walls in one rf period [8]. Another useful Figure of merit is the loaded quality factor, Q_L defined as

$$Q_L = \frac{\omega_0 U}{P_{tot}} \tag{2.2}$$

where P_{tot} is the total power draining from the cavity including wall losses and losses into the fundamental power coupler and rf pick up. When the rf drive for the cavity is turned off, the energy in the cavity will decay exponentially according to

$$U(t) = U_0 \exp\left(\frac{\omega_0 t}{Q_L}\right) \tag{2.3}$$

where U_0 is the cavity energy at time $t = 0$. The energy in the cavity is proportional to the square of the voltage, and so the voltage decay is

$$V = V_0 \exp\left(-\frac{\omega_0 t}{2Q_L}\right). \tag{2.4}$$

The voltage decay constant is

$$\tau = \frac{2Q_L}{\omega_0}. \tag{2.5}$$

The decay constant τ is determined with an oscilloscope by turning off the rf power and measuring the voltage as a function of time. A fit of equation 2.4 is done on the $V(t)$ data obtained from the oscilloscope and used to extract the decay constant. The angular frequency of the cavity ω_0 is measured with a frequency counter and these values are used to calculate Q_L.

When the cavity is turned off, in addition to power being dissipated through the cavity walls (P_c), power can also leave the cavity through the fundamental power coupler (P_{fpc}) and through the pick up probe (P_{pu}) [8, 32]. The total power dissipation is

$$P_{tot} = P_c + P_{fpc} + P_{pu}. \tag{2.6}$$

The power dissipated in the cavity walls is

$$P_c = P_F - P_R - P_{pu} \tag{2.7}$$

where P_F is the forward power being sent to the cavity and P_R is the reflected power. P_F and P_R are determined through direct measurements. Additional quality factors can be assigned for each power loss mechanism defined as

$$Q_{fpc} = \frac{\omega_0 U}{P_{fpc}} \text{ and } Q_{pu} = \frac{\omega_0 U}{P_{pu}}. \tag{2.8}$$

The loaded quality factor can then be written as

$$\frac{1}{Q_L} = \frac{1}{Q_0} + \frac{1}{Q_{fpc}} + \frac{1}{Q_{pu}}. \tag{2.9}$$

Coupling parameters are defined as

$$\beta_{fpc} = \frac{Q_0}{Q_{fpc}} \text{ and } \beta_{pu} = \frac{Q_0}{Q_{pu}}. \tag{2.10}$$

The coupling parameters are equal to the ratio of power dissipated out the coupler or pick up and the power flowing through the cavity:

$$\beta_{fpc} = \frac{P_{fpc}}{P_c} \text{ and } \beta_{pu} = \frac{P_{pu}}{P_c}. \tag{2.11}$$

Critical coupling occurs when a coupling parameter is equal to one. Thus, the coupling parameters are a measure of how strongly the couplers interact with the cavity [8].

In the test setup at TRIUMF, $P_{fpc} = P_c + P_{pu}$ at critical coupling, which implies that $P_{tot} = 2(P_{fpc} + P_{pu})$. Plugging this into equation 2.2 gives

$$Q_L = \frac{\omega_0 U}{2P_{fpc} + 2P_{pu}}. \tag{2.12}$$

This equation can be re-written as

$$\frac{1}{Q_L} = \frac{2P_{fpc}}{\omega_0 U} + \frac{2P_{pu}}{\omega_0 U}. \tag{2.13}$$

The term $\frac{P_{pu}}{\omega_0 U}$ on the right is known from measurements and subtracted from both sides of equation 2.13. By doing this and using equation 2.1, the unloaded quality factor can be written as

$$Q_0 = \left(\frac{1}{2Q_L} - \frac{P_{pu}}{\omega_0 U} \right)^{-1}. \tag{2.14}$$

Since Q_L is known from measurements of τ_L and ω_0, equation 2.14 can be used to calculate Q_0.

Once Q_0 is known, the peak rf field in the cavity (B_p) can be determined. P_c is measured using power meters, and ω_0 has been determined with a frequency counter. U can then be calculated using these values and equation 2.1. B_p is then determined from U and a geometry constant equal to U/B_p^2 which is determined from simulations.

Measuring the decay constant for every quality factor measurement during a cavity test would take a very long time. Therefore, a calibration constant, k_p is introduced. This calibration constant is defined as

$$k_p = \frac{B_p}{\sqrt{P_{pu}}} \tag{2.15}$$

where B_p is the peak rf field. The calibration constant is determined from the initial decay time measurement. Once the calibration constant is known, B_p and Q_0 can be determined by measuring the forward and reverse powers and cavity frequency.

2.2 RF Equipment

2.2.1 Couplers

The QWR and HWR use different variable rf couplers [29]. The HWR uses a coupler with a loop antenna that couples to the cavity's magnetic field, while the QWR uses a straight antenna coupler that couples to the electric field. This is because the coupler is located near the end of both cavities where the HWR has strong magnetic fields and the QWR has strong electric fields. The couplers can be moved in or out of the cavities to reach critical coupling for a wide range of Q_0 values. This improves the overall accuracy of the cavity measurements by virtually eliminating the reflected power since a wide range of Q_0 values are measured during the various cavity tests. A photo of the couplers is shown in Figure 2.6.

2.2.2 Low Level RF System

A self excited loop (SEL) is used in the low level rf (LLRF) system. The LLRF system provides the low level signal to the amplifier that drives rf power into the system. The LLRF can run in open loop (no regulation), with amplitude regulation, or with amplitude and phase regulation. The SEL keeps track of the resonant mode of the cavity. A low level rf board controls the rf power that is sent to the cavity. This board allows for either pulsed or continuous wave (cw) operation. The LLRF board operates at 140 MHz because it was originally designed for the ISAC-II accelerator [34]. To account for this, an intermediate frequency is used to convert the cavity frequency to 140 MHz for input to the LLRF system, and to convert the output signal to the cavity [35]. This frequency converter uses a bandpass filter to select specific frequencies. A different filter is used for each resonant mode.

The rf signal travels from the cavity to the LLRF system via a pick up cable [36]. The signal is split four ways with a power splitter before it reaches the LLRF system and goes to the frequency counter, pick-up power meter, oscilloscope, and amplifier. These devices (with the exception of the oscilloscope) are pictured in Figure 2.7. The signal that goes to the amplifier is boosted to ensure that the LLRF has sufficient signal strength. This signal then goes to the frequency mixer, which converts the frequency to and from 140 MHz as described in the previous paragraph. Finally, the drive signal is sent to a high power amplifier which is needed to boost the signal from the LLRF system by about three to five orders of magnitude so that it is strong enough to drive the cavity.

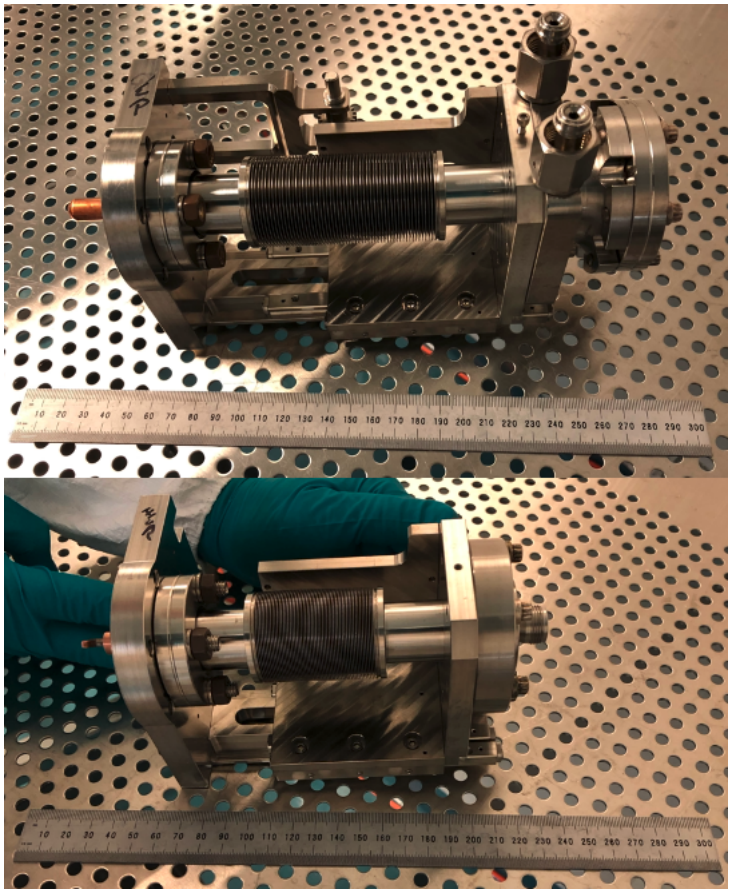

Figure 2.6: Couplers for the QWR (top) and HWR (bottom).

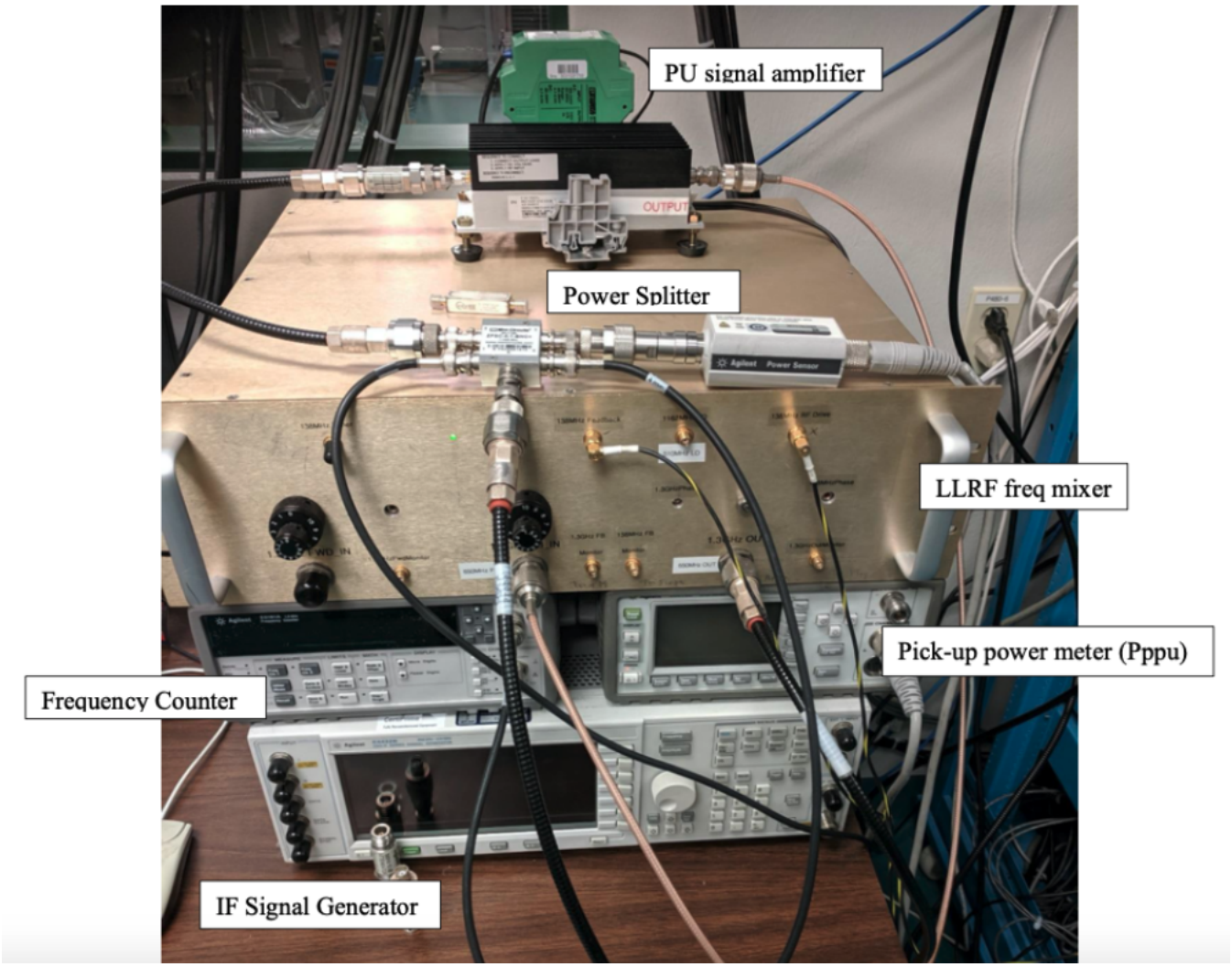

Figure 2.7: Pick up signal distribution to the LLRF system. The LLRF board is not shown. Figure courtesy of [36].

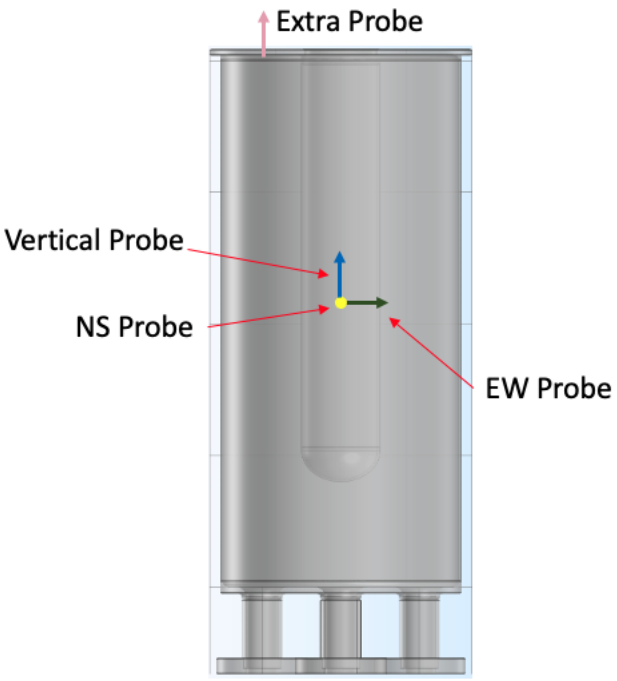

Figure 2.8: Locations and directions of fluxgate probes in the QWR. The red arrows connect the labels to the multi-coloured arrows representing the probes.

2.3 Cryostat

During an experiment, the cryostat contains a coaxial cavity, Helmholtz coils, fluxgate probes, temperature sensors, and liquid helium. The cryostat is located in a class 1000 clean room environment. The cryostat is capable of operating at temperatures of 4.3 to 1.5 K. Temperatures below 4.2 K are reached by lowering the pressure of the liquid helium bath using an external pump on the exhaust side. Cooling down to 2.0 K involves pumping the atmospheric helium to decrease the vapor pressure. Some of the condensed helium evaporates, cooling the remaining liquid. This process is repeated until the helium is cooled to 2.0 K.

2.3.1 Diagnostics

Fluxgate Probes and Helmholtz Coils

Several fluxgate probes are placed in and around the cavities to measure the magnetic fields while the cavities are cooled down to superconducting temperatures. These probes measure the vertical and horizontal magnetic fields near the cavities. The experimental set up consists of three fluxgate probes in the center of the inner conductor of the cavity, and one on an end plate, shown in Figure 2.8. The fluxgate probes used in these experiments are commercially available Bartington Single Axis Fluxgate Magnetometers [37].

The ambient field near the cavity is controlled by three pairs of Helmholtz coils, shown in Figure 2.9. The direction of the applied magnetic field is controlled by changing the currents in each pair of Helmholtz coils, which can be controlled independently for all three spatial dimensions [29]. The fluxgate probes are used to monitor the fields produced by the Helmholtz coils.

During a cavity cool-down the real-time fluxgate probe readings are monitored on a laptop using a custom made Labview program that also controls the currents through the coils. Cooling the cavity down from room temperature can take roughly one hour. During this time the fluxgate probe readings may drift from their initial settings. This drift is compensated for using the Labview program until the cavity gets close to its critical temperature.

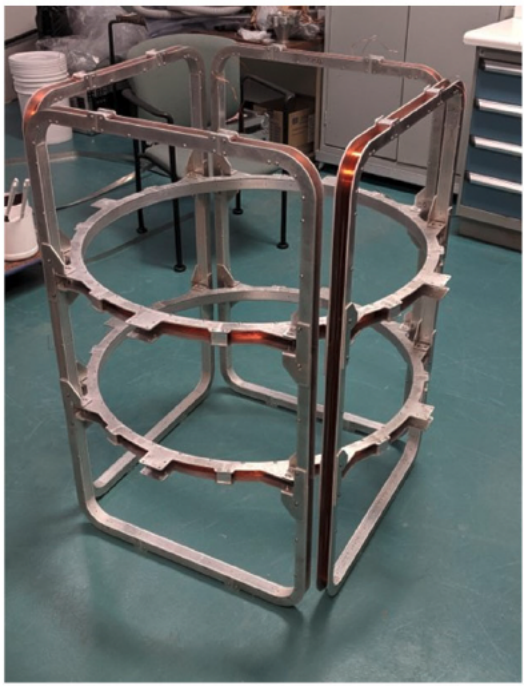

Figure 2.9: Photo of Helmholtz coils. Photo courtesy of [29].

A COMSOL simulation was performed to analyze the uniformity of the magnetic field produced by the Helmholtz coils. The simulation was set up with one Ampere of current in each pair of coils, and the normal conducting QWR placed in the centre. The average magnetic field on the cylindrical surface of the cavity, including the inner conductor, was computed. The deviation from the average magnetic field is shown in Figure 2.10. The centre of the cavity has a lower deviation from the average magnetic field than the top and bottom.

The deviation from the average magnetic field along a vertical line through the centre of the cavity is plotted in Figure 2.11. The x-axis correspond to a line which begins at the centre of the bottom plate, goes through the inner conductor, and ends at the centre of the top plate of the cavity. The largest deviations from the average magnetic field are at the top and bottom of the cavity, where the deviation is about 4 %. Near the geometric centre of the cavity, the deviation from the average magnetic field is close to zero.

Temperature Sensors

The temperature sensors used are two Cernox ^{TM} sensors. The sensors are located on the top and bottom of the cavity. A photo of one of the temperature sensors is shown in Figure 2.12. The temperature sensors are not located directly on the cavity, but rather on aluminum boards that are mounted to the cavity. These temperature sensors are calibrated to give accurate measurements of the absolute value of the temperature of the liquid helium in which the cavity is submerged. It is assumed that the cavity temperature is the same as the liquid helium temperature since niobium has a reasonably high thermal conductivity.

2.4 Cavity Treatments

Different treatments are done on the coaxial cavities in order to compare the cavities' performance before and after the treatments. These can be either surface treatments or heat treatments (bakes).

One of the standard surface treatments performed on the cavities is buffered chemical polishing (BCP) [38]. BCP is done with a 1:1:2 mixture of hydrofluoric acid, nitric acid, and phosphoric acid. When in contact with the niobium, the BCP mixture removes the surface layer at a rate of about 1 μm/minute. BCP

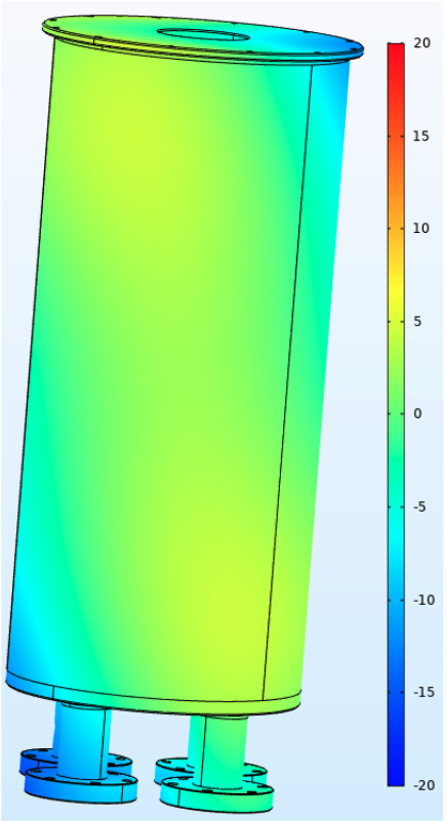

Figure 2.10: Simulation of the QWR in a magnetic field induced by the Helmholtz coils. The colour map represents the difference between the magnetic field and the average magnetic field, divided by the average magnetic field. The average magnetic field is taken over the surface of the cylindrical surface of the cavity, including the inner conductor. For most of the cavity surface the deviation from the average magnetic field is below 5%.

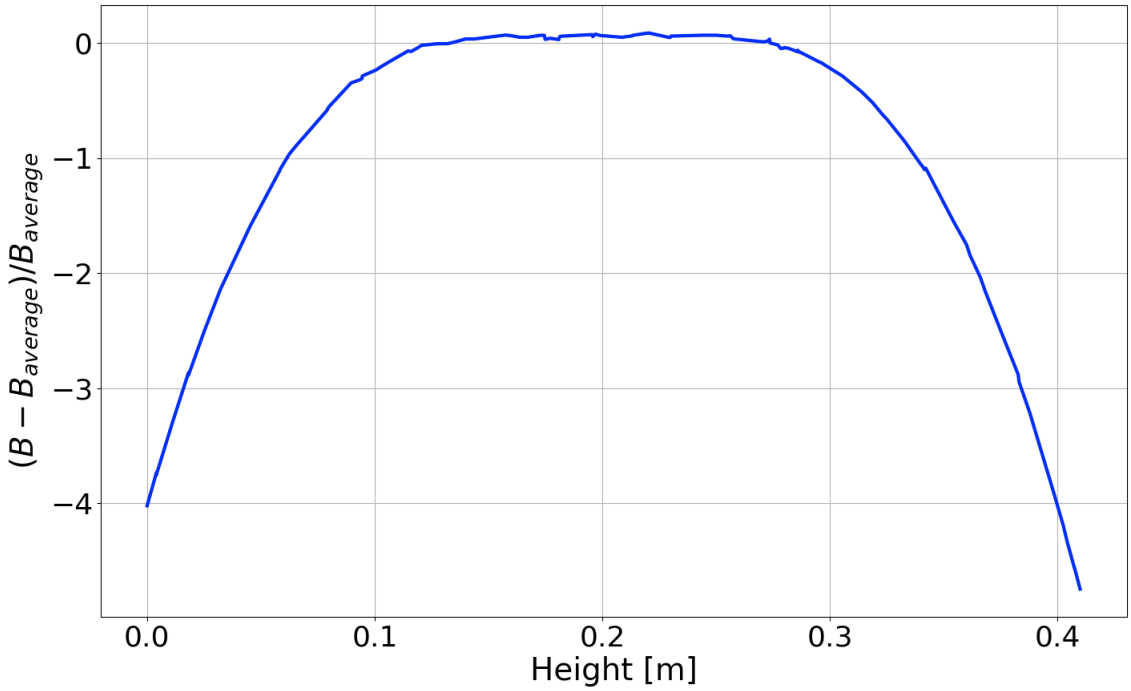

Figure 2.11: Percent deviation of the average magnetic field along a vertical line through the centre of the QWR, from the top plate to the bottom plate. The geometric centre of the cavity corresponds to a height of approximately 0.2 m, at which the deviation from the average magnetic field is close to zero. The data for this plot was extracted from the simulation shown in Figure 2.10.

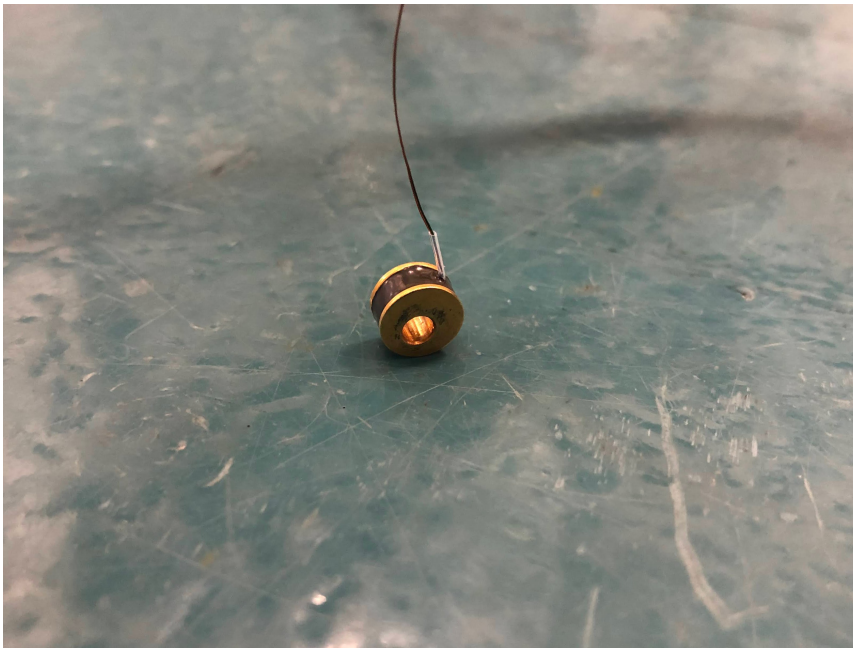

Figure 2.12: Photo of a temperature sensor.

is always used after fabrication to get rid of the damaged layer with a removal of about 120 microns. BCP can also be used to reset the cavity surface between tests. The acid mixture is pumped through a pipeline manifold to the bottom of the cavity with a diffuser. The setup for the BCP treatments was designed so that the entire rf surface of the cavity is in contact with fresh acid flowing through the cavity. During the treatment the temperature of the cavity and acid is regulated to be less than 15 ℃ with a chiller and the chilled water is passed through a jacket surrounding the cavity.

The cavities were designed with a cylindrical wall thickness of 2mm, and an end plate thickness of 4 mm. This gives enough material for surface resets via chemical etching, in which the superconducting surfaces are cleaned [38]. For a surface reset, about 30 μm of material is removed from the cavity surface. Approximately 0.7 mm of material can be removed from the cavities's surface without compromising its structural integrity [29].

The baseline surface treatment that the cavities undergo before a heat treatment consists of a bulk surface removal via BCP of 120 μm, 800 ℃ degassing in the TRIUMF induction furnace, and a 15 μm BCP surface etch. These treatments can prevent Q disease by removing hydrogen from the cavity [39]. Q disease is a mechanism of power loss caused by dissolved hydrogen in the bulk niobium precipitating as hydrides at the rf surface [8].

Heat treatments including 800, 400, and 300 ℃ bakes are performed in the TRIUMF induction furnace. This furnace works by heating a niobium susceptor via rf induction and transferring the heat to the cavity via radiation [40]. During the bake niobium caps are placed on the cavity ports to reduce the risk of contamination. These bakes aim to improve the cavity performance by manipulating the near surface of the superconductor where the rf currents flow. Customized baking/doping has been found to achieve higher quality factors.

A heat treatment commonly used as part of the preparation for SRF niobium cavities is a low temperature bake of 90-150 ℃ done while the cavity is under vacuum [41]. Treatments in this temperature regime have been found to eliminate the high field Q slope (HFQS) in electro-polished 1.3 GHz cavities. HFQS refers to a phenomenon in which cavities experience anomalous field dependence of their quality factors at high rf fields [42]. The exact cause of HFQS's is not known, but they are believed to be related to diffusion of hydrogen and oxygen in the cavities' inner surface. Low temperature bakes have been found to reduce the temperature dependent surface resistance and increase temperature independent surface resistance in elliptical cavities [43]. Baking the cavity at 120 ℃ diffuses oxygen from the oxide layer in the near surface of the niobium, reducing its mean free path. These bakes were also shown to reduce the concentration of free hydrogen in the cavity's surface. It is suggested that this reduction in free hydrogen concentration is caused by the elimination vacancy hydrogen (Vac-H) complexes. The Vac-H complexes are thought to dissociate during low temperature bakes and then diffuse and annihilate in the near-surface of the cavity, leaving much fewer sites for hydride nucleation. The low temperature heat treatment done on the coaxial cavities at TRIUMF is a 120 ℃ bake done for 48 hours while the cavity is in the cryostat and heated with resistive heaters while under vacuum.

Other treatments that have been found to be effective on niobium cavities are mid-temperature furnace bakes between about 250 to 500 ℃ [44]. Mid-temperature bakes have been shown to increase the quality factor in 9-cell elliptical niobium cavities, while bakes of 300 ℃ in particular result in very high quality factors. It has been demonstrated that mid-temperature bakes significantly reduce a cavity's temperature dependent surface resistance in a manner similar to nitrogen doping. After a mid-temperature bake a cavity does not require electro-polishing or nitrogen doping. Mid-temperature bakes cause the oxide layer to break down at the surface and diffuse into the bulk [45]. Both nitrogen doped and mid-temperature baked cavities have a higher magnetic sensitivity [46, 47].

High temperature bakes are those in which a cavity is baked at 600-800 ℃ [48]. These high temperature bakes have been shown to decrease a cavity's temperature independent surface resistance, while the temperature dependent surface resistance was not significantly reduced in the study described in reference [48]. Temperatures of 800 ℃ and above can be used to partially or fully anneal the niobium, reducing pinning centers that can lead to flux trapping.

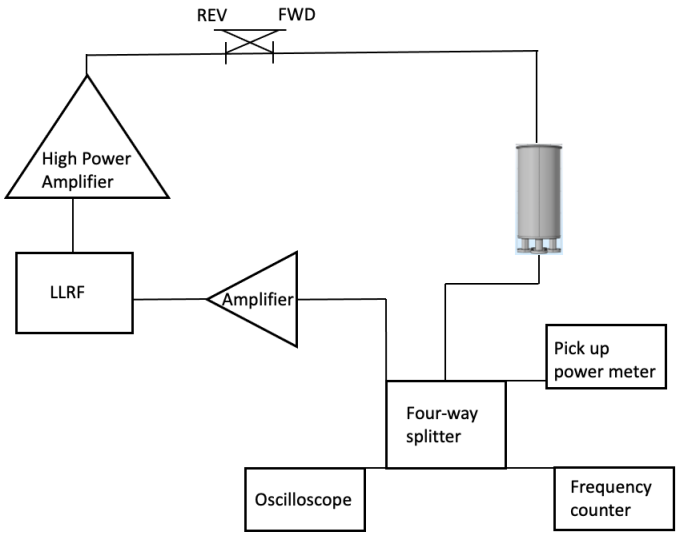

Figure 2.13: Circuit diagram for the coaxial cavity experimental setup.

One surface treatment for SRF niobium cavities is nitrogen-doping [49]. In this process, nitrogen is infused into an SRF cavity while it is in a furnace at a temperature of 800 ℃. The nitrogen is diffused into the bulk of the cavity surface which leads to improved quality factors by decreasing the cavity's temperature dependent surface resistance. Nitrogen-doping is not currently available at TRIUMF.

Before each cavity test, the coaxial cavities undergo a high pressure rinsing to rid them of surface particulates that could result in field emission. After rinsing, the cavities are dried and assembled with the rf coupler and pick up. These steps are all done in a clean room.

2.5 Collecting Data

The measurements of Q_0 and B_p begin after the cryostat has been filled with 4.2 K liquid helium and the cavity has reached a constant temperature of 4.2 K [28]. At a pressure of one atmosphere, helium becomes liquid at 4.2 K. Measurements of Q_0 are done for a wider range of B_p values until a quench field is reached. The cavity is then slowly cooled down to 2.0 K by pumping on the liquid helium in the cryostat. A pressure of 30 mbar is required to reach 2.0 K. During the cool-down, Q_0 and temperature measurements are taken for fixed values of B_p in order to collect field dependent data on the cavity surface resistance. Once the cavity reaches 2.0 K, another set of fixed temperature measurements is taken for a wider range of B_p values until a quench field is reached. The cavity is then cooled down below 2.0 K during which time Q_0 and temperature measurements are taken for fixed values of B_p until the measured Q_0 values stop changing. These measurements are done for each resonant mode of the cavities.

2.5.1 Circuit Diagram

Figure 2.13 shows a circuit diagram for the experimental setup used to drive the coaxial cavities and record quality factor and peak rf field data. The diagram shows the path of the RF power during a cavity test. The RF power travels clockwise around the self-excited loop.

2.5.2 Changing Parameters

During a cavity test, some parameters are changed to explore how they affect cavity performance. In addition to the surface treatment, the cavity temperature, and the cavity rf field, the varied parameters are the cool-down rate, cavity frequency, and applied magnetic field. During some cavity tests, the cavity was

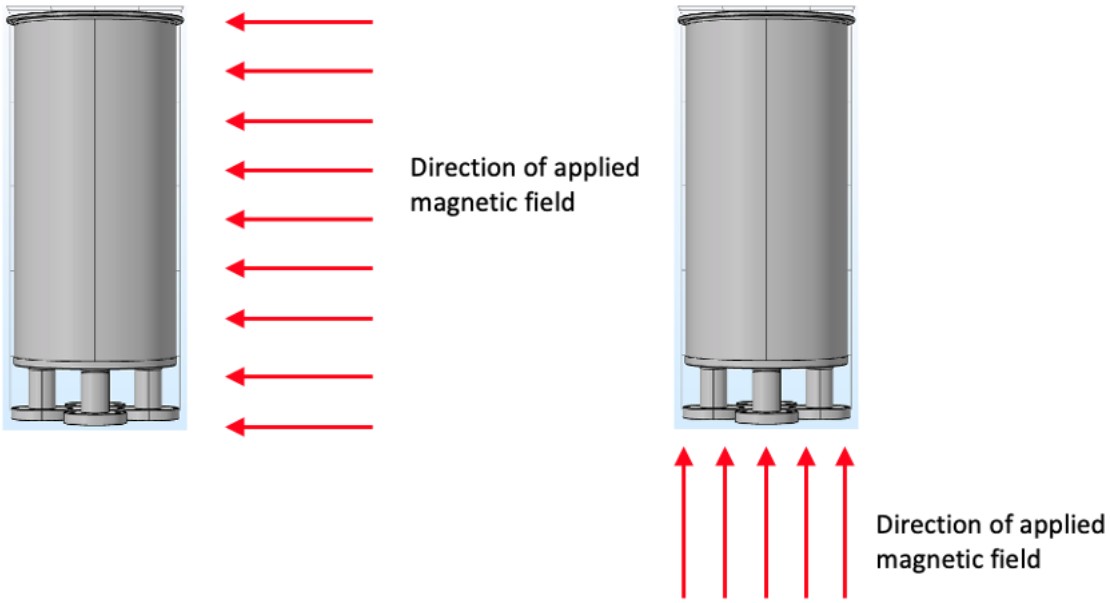

Figure 2.14: Arrows showing the directions of the applied magnetic fields on a coaxial cavity. Left: Applied magnetic field orthogonal to the cavities axis (horizontal field). Right: Applied magnetic field parallel to the cavities's axis (vertical field).

cooled down through its critical temperature at a faster or slower rate to see how this would affect the flux expulsion efficiency. These varied parameters are compared to the baseline cool-down in which the cavity is cooled fast with approximately zero external magnetic fields. For most experiments, the HWR cavity parameters are measured for the resonant modes 389, 778, and 1166 MHz, while the QWR parameters are measured for the resonant modes 217 and 648 MHz.

For some experiments, an external magnetic field is applied to the cavity using the Helmholtz coils in order to see how well or how poorly a cavity can expel magnetic flux at different cool-down speeds or after different treatments. For these experiments an external magnetic field of 10, 20, or 40 μT is applied to the cavity in either the horizontal direction or vertical direction. For the horizontal direction, the applied magnetic field is orthogonal to the cavity's axis as shown on the left of Figure 2.14. For the vertical direction, the applied magnetic field lines are parallel to the cavity's axis as shown on the right of Figure 2.14. These fields are applied continuously as the cavities' are cooled down through the critical temperature. These measurements can be compared to the cavities' performance after it is cooled down with a "zero" field in which the Helmholtz coils are used to bring the ambient magnetic field at the field probes to a minimum value.

2.5.3 Uncertainties

The cavity measurement uncertainties of Q_0 and B_p, described in Section 2.1.3 are dominated by the directivity errors of the directional coupler antennas [29, 50]. This results in a mismatch of the quality factors of the coupler and cavity, which leads to errors in the calibration constant. This will lead to errors in B_p and Q_0 since the calibration constant is used to calculate these values.

The measurement uncertainties of the calibration constant are quantified as deviations of the standing wave ratio from unity [32]. The SWR is calculated using the forward and reverse powers [51] according to

$$\mathrm{SWR} = \frac{\sqrt{P_{forward}} \pm \sqrt{P_{reverse}}}{\sqrt{P_{forward}} \mp \sqrt{P_{reverse}}}, \tag{2.16}$$

where the above equation corresponds to an overcoupled input coupler, and the plus and minus signs would be reversed for an undercoupled input coupler. The uncertainties in the measurements of B_p and Q_0 are determined by the standing wave ratio (SWR). If the SWR is greater than one, the uncertainties in B_p and Q_0 are

$$\frac{\delta B_p}{B_p} = \frac{\mathrm{SWR} - 1}{4} \quad \text{and} \quad \frac{\delta Q_0}{Q_0} = \frac{\mathrm{SWR} - 1}{2} \tag{2.17}$$

respectively.

Another source of error for Q_0 and B_p is the uncertainty in the decay time measurement. As described in Section 2.1.3, the decay constant τ is determined with a fit of voltage vs time performed with an oscilloscope. The fitting range is chosen to be small enough that τ is accurate to within 1 ms. For most experiments performed in this thesis the value of τ is at least 100 ms. Therefore, the measured τ value is expected to be accurate to within 1 %. By fitting only a small range starting right after the rf is turned off, changes in Q_0 as a function of the changing rf amplitude are minimized. Thus, the value of Q_0 is approximately constant during the decay time measurement. However, if Q_0 were to change during the decay time measurement this would add additional uncertainty as τ would itself become a function of time. It was determined in a study by Melnychuk that the error due to variations in the Q_0 slope during τ measurements is negligible [52]. The accuracy of the decay constant is also limited by the finite sampling rate of the oscilloscope. Other sources of uncertainty from the τ measurement include random instrument error of the oscilloscope and uncertainties in the voltage vs time fit.

Additional sources of error for the B_p and Q_0 measurements are the finite precision of the power meters and frequency counter used in Q measurements, as well as random error associated with variations in the hardware. The power meter used is an Agilent E4419B EPM Series Power Meter, with an accuracy of ± 0.02 dB [53]. The frequency counter is an Agilent 53181A Frequency Counter, with an accuracy of about $1\text{x}10^{-2}$ Hz [54]. These instrument errors are negligible compared to the errors associated with the directional couplers. Variations in the hardware can include variations in the bending and tightness of the rf cables. This source of error is thought to be small due to the consistency of measured cable attenuations.

The non-corrected surface resistance, R_s^* (described in Section 3.1.1) is defined as $R_s^* = G/Q_0$. The geometry factor is a constant of the cavity computed using a finite element code. For this reason the geometry factor contributes a systematic error and not a random measurement error. The systematic error in G is constant and small compared to the Q measurement uncertainties. Therefore, the relative uncertainty in R_s^* is equal to the relative uncertainty in Q_0 [55].

Chapter 3

Simulations and Data Processing

3.1 Data Processing

3.1.1 Rs* to Rs

After a cavity measurement is completed, the non-field corrected surface resistance, henceforth referred to as R_s^* is computed using equation 1.18, where the geometry factor is derived in equation 1.19. The values for the geometry factors can be found in Table 2.1. The R_s^* approximation assumes that the cavity has a constant surface resistance and no field dependence, which is not the case for the TRIUMF coaxial test cavities. When SRF cavities are superconducting their surface resistance typically has a dependence on the local rf surface magnetic field. In coaxial cavities (see Figures 2.3 and 2.5) the rf magnetic field varies from high values at the root of the inner conductor and very low values at the tip of the inner conductor for the QWR and at the midpoint of the inner conductor for the HWR. Therefore if the surface resistance has a dependence on the magnetic field, then the surface resistance is also non-uniform and the assumption used to drive equation 1.19 is incorrect. Therefore R_s^* must be converted to the field corrected surface resistance value, henceforth referred to as R_s. These two resistances are related by

$$R_s^* \int |H^2| ds = \int R_s |H^2| ds \tag{3.1}$$

where the integral is taken over the entire cavity surface area. This method of computing R_s was developed by Delayen [56] and a summary follows.

$R_s^*(B_p)$ can be expressed as a polynomial function

$$R_s^*(B_p) = \sum_{\alpha_i} r_{\alpha_i} B_p^{\alpha_i} \tag{3.2}$$

where the coefficients r_{α_i} are fit parameters, and the values of α_i used are 0,1,2, and 3.

It follows that $R_s(B_p)$ can also be expressed as a polynomial function

$$R_s(B_p) = \sum_{\alpha_i} \beta(\alpha_i) r_{\alpha_i} B_p^{\alpha_i} \tag{3.3}$$

where the r_{α_i} coefficients determined with equation 3.2 are corrected via a multiplication with appropriate $\beta(\alpha_i)$ values which have been calculated numerically and are listed in Table 3.1. The correcting beta values are characteristic of the field variation over the rf surface of the cavity and are thus geometry dependent. Coaxial cavities have more localized magnetic field distributions than elliptical cavities. Figure 3.1 is an example of the difference between R_s and R_s^* in which both surface resistances are plotted on the vertical axis as a function of peak rf field. The corrected surface resistance values have larger vertical error bars due to the uncertainties in the fit functions used to compute those values.

The blue points in Figure 3.1 are the result of evaluating the $R_s(B_p)$ new polynomial in equation 3.3 at the measured B_p values.

Cavity, Resonant Frequency	$\beta(0)$	$\beta(1)$	$\beta(2)$	$\beta(3)$
QWR, 217 MHz	1.0	1.432	1.778	2.061
QWR, 648 MHz	1.0	1.473	1.871	2.213
HWR, 389 MHz	1.0	1.463	1.857	2.193
HWR, 778 MHz	1.0	1.461	1.857	2.502
HWR, 1166 MHz	1.0	1.463	1.862	2.206

Table 3.1: $\beta(\alpha_i)$ values for QWR and HWR at different resonant frequencies. Table values courtesy of [29].

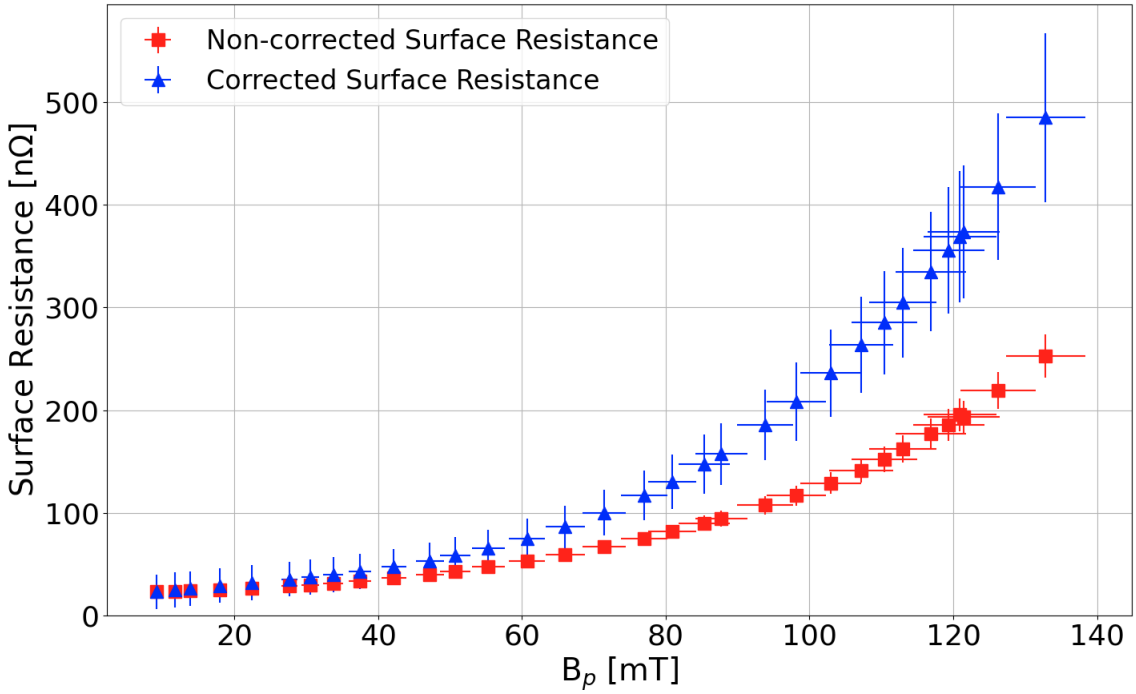

Figure 3.1: Corrected (blue triangles) and Non-corrected (red squares) surface resistance as a function of peak rf field for the QWR in the 217 MHz mode at 4K. The field corrected R_s values have a stronger dependence on peak rf field.

3.1.2 BCS Fits

In order to extract the temperature dependence of R_s from the cavity measurements, the quality factor and cavity temperature are determined for some number of fixed B_p values in intervals of 10mT during the cool-down. The cavity temperature is obtained by measuring the temperature of the helium bath with the assumption that the cavity is at the same temperature. For example, during a cool-down the temperature and quality factor may be measured for sets of B_p values from 10-100 mT in intervals of 10mT. These measurements are done repeatedly throughout the entire cool-down from about 4.2 to 2 K yielding data approximately every ten milli-Kelvin. During each measured set spanning the full B_p range, the temperature changes by less than 0.1 K since the cavity cools down slowly. Each data set is individually converted to R_s^* using equation 1.18, fit to equation 3.2, and finally converted to R_s using equation 3.3.

The cavity surface resistance R_s can also be expressed as a function of temperature as in equation 1.21 [8]. Equation 1.21 can be parametrized and rewritten as

$$R_s(T) = R_{BCS}(T) + R_0 = \frac{a_0}{T}\ln\left(\frac{4k_BT}{\hbar\omega}\right)\exp\left(\frac{-a_1(T)T_c}{T}\right) + a_2 \tag{3.4}$$

where a_0 and a_2 are free fit parameters, and T_c is the critical temperature of niobium, 9.2 K. The parameter

$a_1(T)$ represents the energy gap Δ in equation 1.22, and a_2 represents R_0. The function $a_1(T)$ is defined as

$$a_1(T) = a_1\sqrt{\cos\left(\frac{\pi}{2}\left(\frac{T}{T_c}\right)^2\right)} \tag{3.5}$$

where a_1 is a free fit parameter [57].

Equation 3.4 assumes that the rf surface is isothermal and is equal to the liquid helium temperature, which is a good approximation when the liquid helium is below a temperature of 2.175 K. At temperatures below 2.175 K, helium becomes a superfluid, which means that it has zero viscosity [58]. When the helium bath is in the superfluid state there is more efficient heat transfer between the cavity and the helium. When the helium bath is at higher temperatures, there is less efficient heat transfer to the cavity, and thus the cavity is more susceptible to local heating caused by finite thermal conductance in niobium and at the niobium-helium interface [59, 60]. This leads to a small discontinuity in $R_s(T)$ at 2.175 K with slightly higher resistances above the superfluid temperature. To take this into account, a new parameter, ΔR_s is added, modifying equation 3.4 to

$$R_s(T) = R_{BCS}(T) + R_0 = \frac{a_0}{T}\ln\left(\frac{4k_BT}{\hbar\omega}\right)\exp\left(\frac{-a_1(T)T_c}{T}\right) + a_2 + \Delta R_s \cdot \theta(T - 2.175), \tag{3.6}$$

where $\theta(T - 2.175)$ is a step function defined as

$$\theta(T - 2.175) = \begin{cases} 0 & T > 2.175\text{K} \\ \\ -1 & T \leq 2.175\text{K}. \end{cases}$$

Figure 3.2 shows an example of R_s data fitted to equation 3.6. The fit equation is represented by dashed lines while the data points are circles. The superfluid transition temperature, or lambda point is labeled with a gray vertical dashed line. It can be seen in Figure 3.2 that for some field amplitudes the fit function has a discontinuity at the lambda point. This discontinuity is larger for the larger field amplitudes because at higher field amplitudes there is more power dissipated per unit area and therefore a larger temperature difference across the rf to liquid helium interface.

For these fits, the natural logarithm of the temperature data is fit to the natural logarithm of equation 3.6 and the parameters a_0, a_1, a_2, and ΔR_s are extracted from this fit. Equation 3.6 is then plotted using the extracted fit parameters and temperature values. This is done to improve the quality of the fits near the lambda point. The fits done with and without the use of natural logarithms are compared by calculating the percent difference between the experimental data points and the corresponding values of the fit function. This percentage is described by the expression

$$|R_{s\ \text{fit}} - R_{s\ \text{measured}}| \times \frac{100}{R_{s\ \text{measured}}} \tag{3.7}$$

where $R_{s\ \text{measured}}$ is the experimental R_s value at a given peak rf field, and $R_{s\ \text{fit}}$ is the value of the fit function evaluated at the same peak rf field. The averages of these residual percentages for each field amplitude are listed in Table 3.2

For all field amplitudes, the residual percentages are much lower for the fits that were done using the natural logarithm technique. In general the residuals tend to increase with field amplitude. This may be because the fit equation does not take field amplitude into account.

3.2 COMSOL Cavity Simulations

COMSOL Multiphysics ® is a simulation software capable of mulitphysics modeling [31]. Version 5.4 of COMSOL Multiphysics ® is used for all simulations. The purpose of performing COMSOL simulations is to see what parts of the cavities' surface has higher or lower levels of magnetic flux when the cavity is superconducting, and to better understand the movement of flux during the superconducting transition.

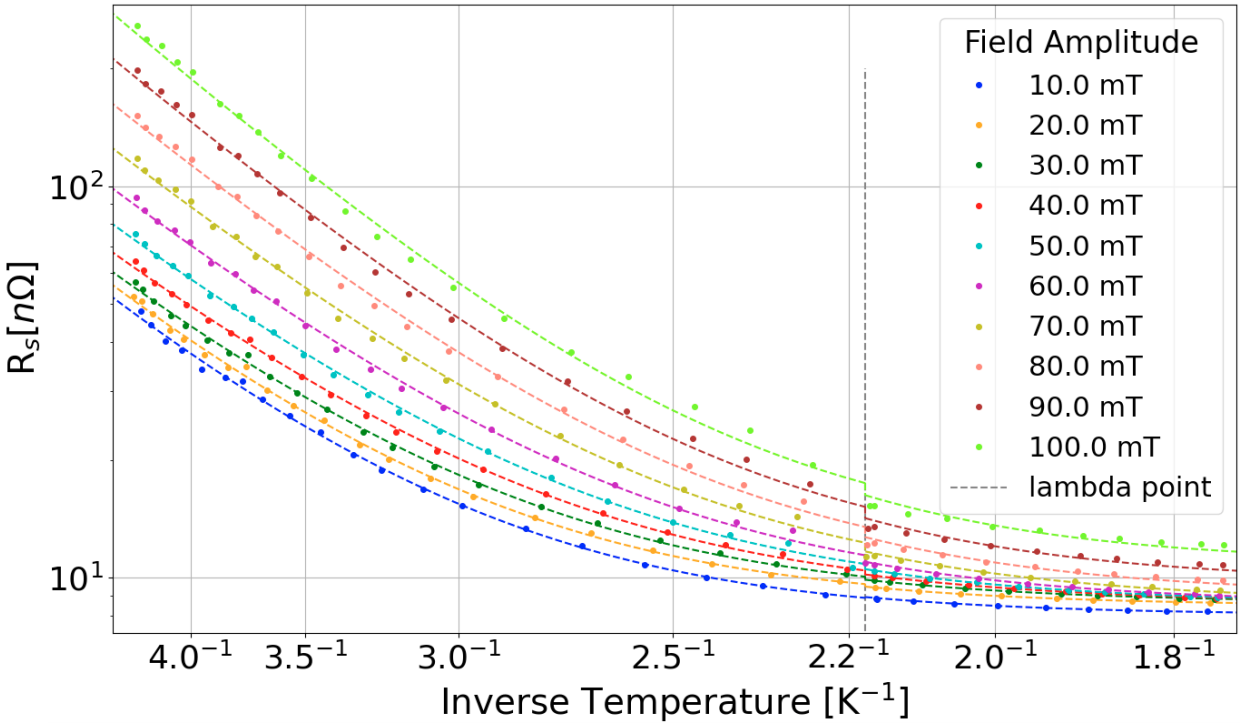

Figure 3.2: R_s vs inverse temperature data set from the HWR in the 389 MHz mode fitted to the BCS formula. The vertical gray line marks the helium superfluid transition temperature, at which there is a discontinuity in the R_s values. When the helium is in a superfluid state there is more efficient heat transfer between the cavity and the helium, leading to lower surface resistances.

Field Amplitude [mT]	Average residual percentage using natural logarithms	Average residual percentage without using natural logarithms
10	9.0E-3	1.9E-1
20	8.7E-3	2.1E-1
30	9.0E-3	2.3E-1
40	9.3E-3	2.3E-1
50	1.2E-2	2.8E-1
60	1.6E-2	3.8E-1
70	1.9E-2	4.4E-1
80	2.4E-2	5.1E-1
90	2.7E-2	6.2E-1
100	2.9E-2	7.1E-1

Table 3.2: Average residual percentages for the BCS fits shown in Figure 3.2.

These simulations can also be used to suggest locations of interest for placing magnetic field probes on the physical cavities.

For the COMSOL simulations, three dimensional models of both the HWR and QWR are made. These models have the exact geometrical dimensions as the actual cavities. To simplify the modeling, the small bolt holes on the rinse port flanges and top end plate of the cavities are removed from the simulated cavities. The cavities are placed inside a simulated box of material with a relative magnetic permeability of one.

The COMSOL physics module "Magnetic Fields, No Currents" is used for all simulations. To simulate the superconducting state of the cavities, the cavity material is assigned a relative permeability of 1×10^{-14}, while the box of air surrounding the cavities is assigned a relative permeability of 1. The cavity material is assigned a relative permeability of 1×10^{-14} instead of zero because if a value of zero is assigned, COMSOL produces a divide by zero error in the magnetic field calculation and the simulation cannot be completed. In the Magnetic Fields, No Currents module, magnetic fields can be applied to the cavity in any spatial dimension.

3.2.1 Time Independent Simulations

Time independent simulations are performed on the HWR and QWR in which the magnetic fields and relative permeabilities do not change with time. These studies aim to demonstrate the behavior of a idealized SRF cavity upon entering a Meissner state.

HWR Results

The simulation of the HWR with a vertical applied field of $10\,\mu$T, is shown in Figure 3.3. Black flux lines are plotted in the mid-plane of the cavity. The heat map on the right of the plot shows the magnetic flux in μT. In the area on the right and left sides of the cavity the magnetic flux is about $10\,\mu$T, represented by the orange colour in the heat map. There is less magnetic flux around the top and bottom parts of the cavity because the diamagnetic cavity material repels the flux. Inside the inner conductor the field is enhanced to a value of about $12\,\mu$T due to the flux being pushed away from the superconducting cavity walls and into the inner conductor.

The HWR is also simulated with a horizontal magnetic field of $10\,\mu$T, shown in Figure 3.4. In this simulation most of the magnetic flux is bent around the cavity. The magnetic flux on the left side of the image, far from the cavity was found to be the same as the magnetic flux on the right side of the image far from the cavity, even though the plot shows more magnetic flux lines on the left than on the right. This is believed to be a peculiarity of how COMSOL plots magnetic flux lines. The flux in the center of the cavity is found to be about $0\,\mu$T, indicative of the fact that the outer and inner conductor shield the sensor from the magnetic field when in the Meissner state.

QWR Results

The QWR is simulated with applied fields of $10\,\mu$T in the vertical and horizontal directions shown in Figures 3.5 and 3.6, respectively. In the vertical simulation the field in the inner conductor is zero due to the shielding at the bottom of the inner conductor.

The results of the horizontal simulation are similar to those of the HWR, in which the magnetic flux is mostly bent around the cavity and the field at the location of the sensor is zero when the cavity is in the Meissner state.

3.2.2 Time Dependent Simulations

The static simulations show how an idealized SRF cavity would behave after entering a Meissner state. However, in reality the entire cavity does not enter the superconducting state instantaneously. Instead a superconducting front moves continuously along the cavity surface as the cavity is gradually cooled to superconducting temperatures. This superconducting front pushes magnetic flux as it moves along the cavity. To account for this, time dependent simulations are performed.

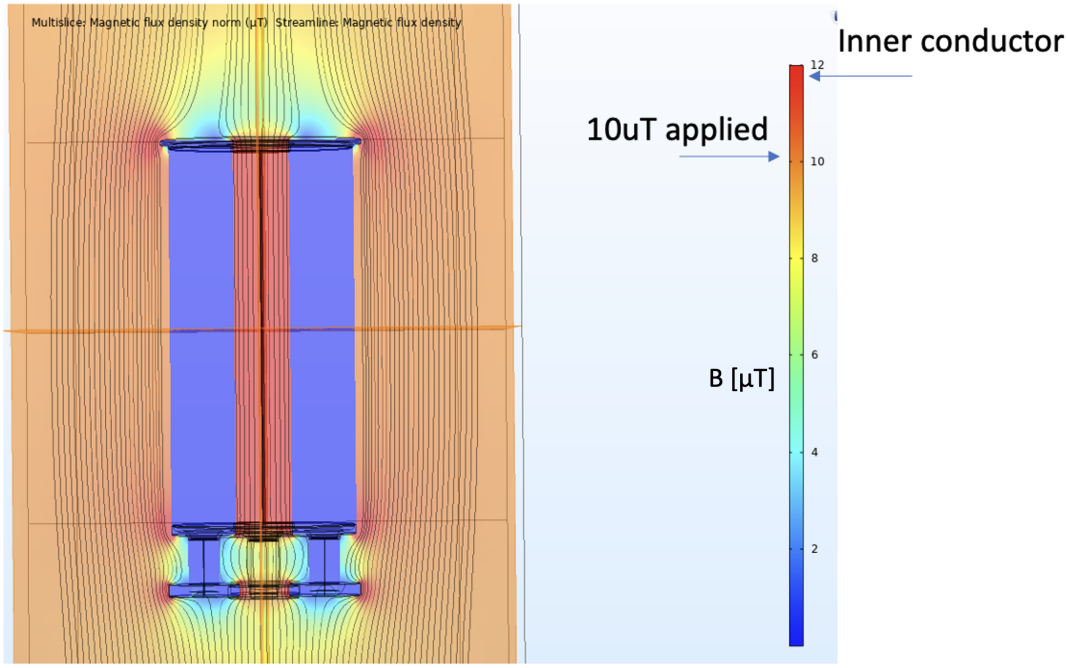

Figure 3.3: COMSOL ® simulation of 10 μT applied to the HWR in the vertical direction with the cavity in the Meissner state. Some magnetic flux is funneled into the inner conductor, giving it a field enhancement of about 20%.

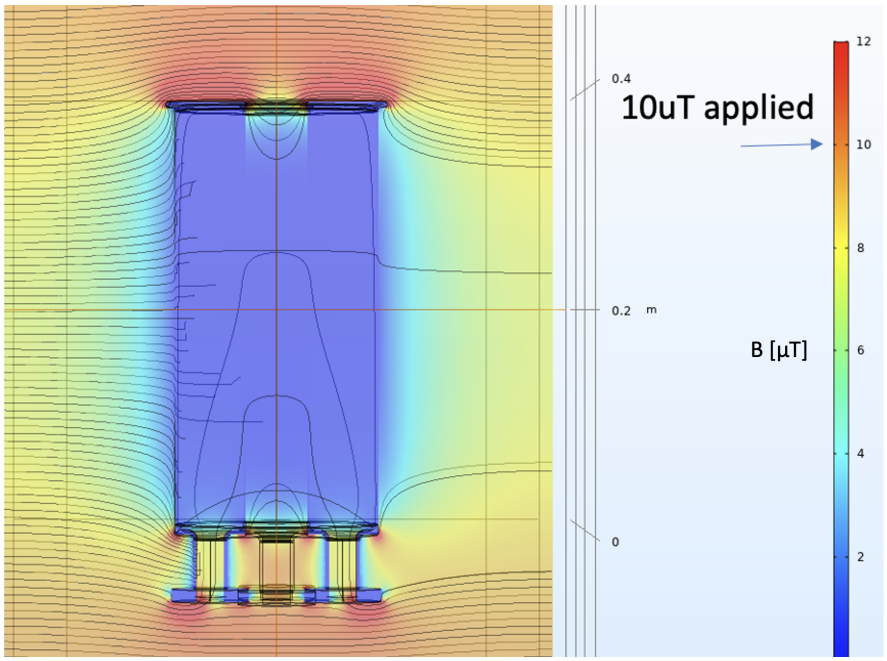

Figure 3.4: COMSOL ® simulation of 10 μT applied to the HWR in the horizontal direction with the cavity in the Meissner state. There is no magnetic flux in the center of the inner conductor since it is shielded by the outer conductor for this applied field orientation.

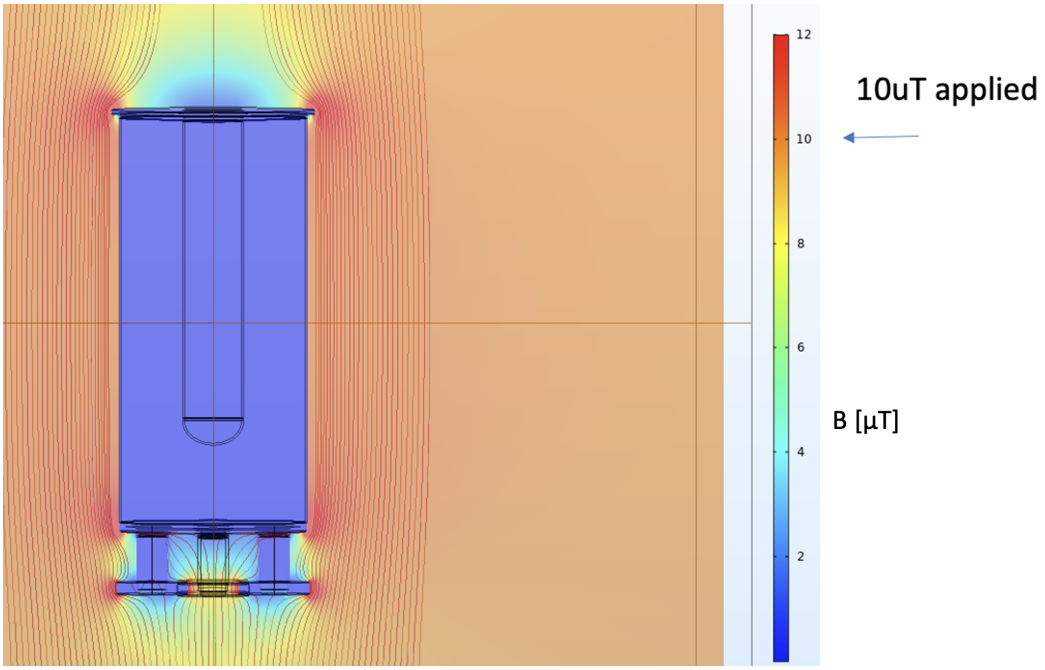

Figure 3.5: COMSOL ® simulation of 10 μT applied to the QWR in the vertical direction with the cavity in the Meissner state. This simulation does not show any flux trapping within the cavity.

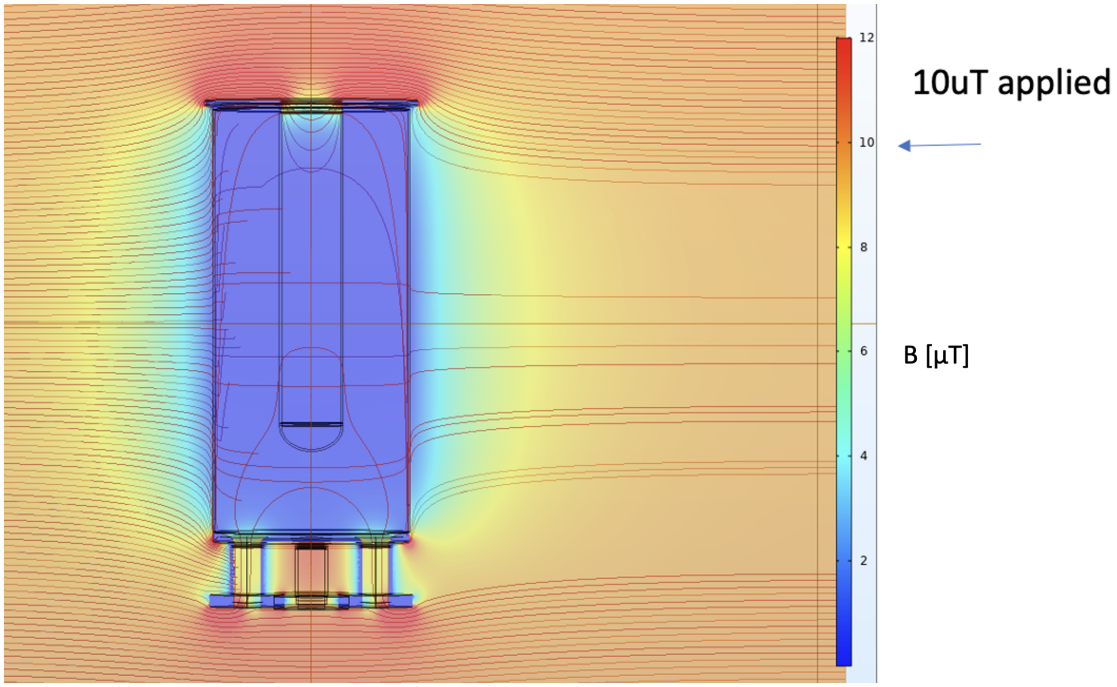

Figure 3.6: COMSOL ® simulation of 10 μT applied to the QWR in the horizontal direction with the cavity in the Meissner state.

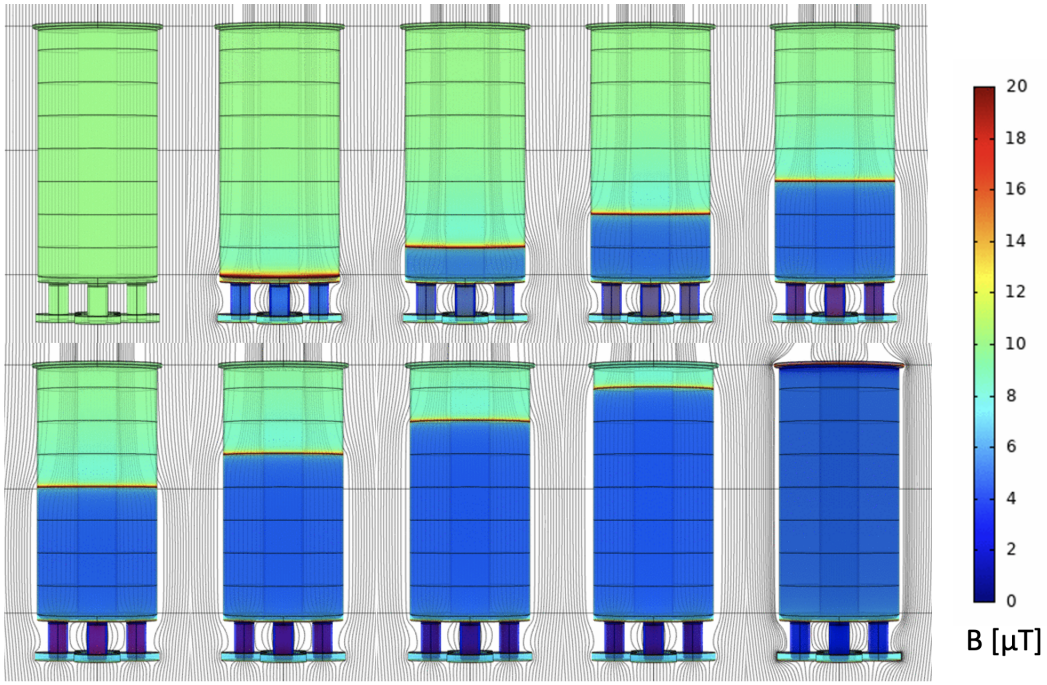

Figure 3.7: Time dependent COMSOL ® simulation of 10 μT applied to the HWR in the vertical direction. The superconducting phase front moves up the cavity as it is cooled from bottom to top. The colour legend on the right shows the magnetic flux in μT in the vertical plane. In the last image, the cavity is fully superconducting and matches the results of the time independent simulation in Figure 3.3.

These time dependent simulations of the cavities are done by changing the relative permeability of the cavities sequentially given a prescribed cooling time evolution. For these simulations, the cavity is sliced horizontally into different sections. These sections are changed from non-magnetic to diamagnetic material sequentially in the presence of an applied magnetic field, assuming a particular cool-down sequence. This is similar to what happens in a real cavity cool-down in which parts of the cavity become superconducting before others as the cryostat is filled with helium.

HWR Results

When the HWR is cooled down, liquid helium is first transferred into the bottom of the bath cryostat. Before the liquid helium builds up, cold gas collects at the bottom, which cools the bottom of the cavity. Heat is mostly transferred via conduction in the cavity walls, resulting in a temperature distribution in which the superconducting phase front moves from bottom to top. The COMSOL ® simulations model this cool-down sequence. A time dependent simulation of the HWR in a vertical magnetic field is shown in Figure 3.7. The simulation assumes that as the cavity cools down, a superconducting front moves up the cavity, pushing flux out of and away from the cavity.

Starting at the top left of Figure 3.7, all sections of the cavity have a relative permeability (μ_r) equal to one. As the images progress left to right on the top row, and then left to right on the bottom row, the μ_r of each cavity Section is changed to nearly zero to replicate a diamagnetic state. As the sections of the cavity become diamagnetic, the flux lines are pushed away from the cavity, and some are squeezed into the rinse ports or inner conductor. The last time step of this simulation matches the results of the time independent HWR vertical field simulation with the cavity fully in the Meissner state. A cut out view of the HWR vertical applied field cool-down is shown in Figure 3.8.

The magnetic field at the location of the fluxgate probes in the inner conductor is plotted in Figure 3.9. Each unit of time on the horizontal axis corresponds to one slice of the cavity entering the Meissner state as in Figure 3.7. The vertical magnetic field is depicted by the green line labeled Bz. As the cavity cools

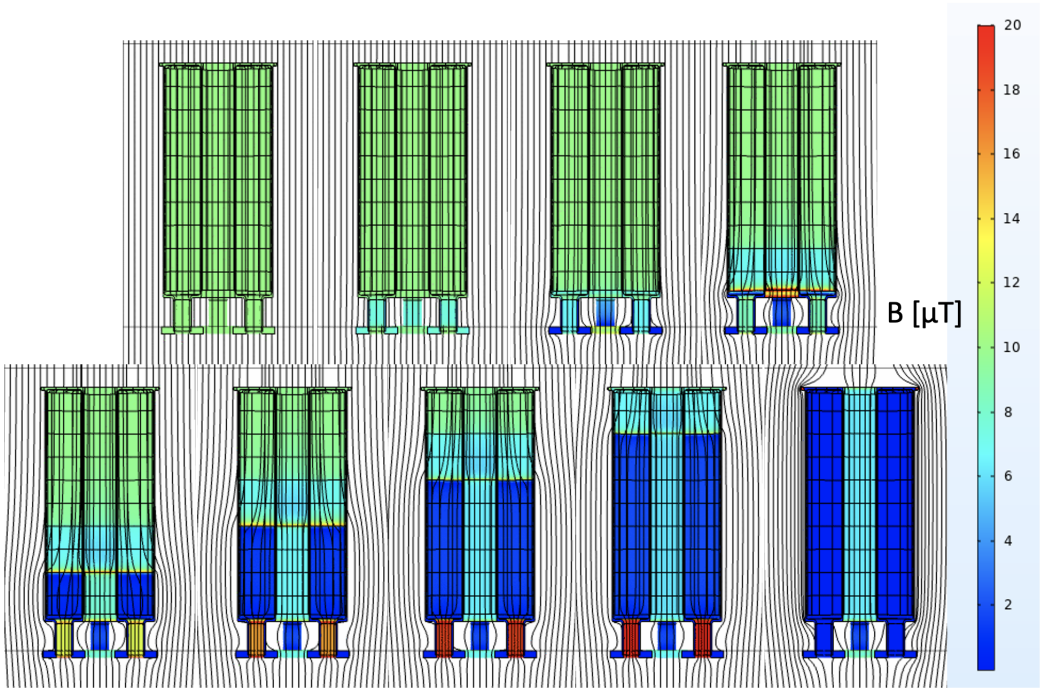

Figure 3.8: Time dependent COMSOL ® simulation of 10 μT applied to the HWR in the vertical direction. This simulation is similar to the one shown in Figure 3.7 with the main difference being that this figure shows a cut out image of the inside of the HWR.

the magnetic field in the center of the inner conductor initially decreases, and then increases after the superconducting phase front has passed. The field increases by about 20% over the applied field. This is because magnetic flux is funneled into the center of the inner conductor where the probes are located. The end results of this time dependent simulation are in agreement with the results of the time independent simulation.

A time dependent simulation of the HWR cooling down with a horizontal applied field is depicted in Figure 3.10. This simulation was made in a manner similar to the simulation in Figure 3.7, with the main difference being that in Figure 3.10 the cavity has been sliced in half along its vertical axis, and only half of the cavity is simulated. This was done because simulating half of a cavity is much less time consuming. To model this symmetry cut, the magnetic insulation node is used as a boundary condition on all sides of the box containing the cavity. For this boundary condition, the normal component of the magnetic flux density is zero ($\hat{\mathbf{n}} \cdot \mathbf{B} = 0$) [61]. In this simulation flux lines are diverted away from the diamagnetic cavity sections towards nearby normal-conducting sections. As with the vertical case, the last time step of this simulation matches the results of the time-independent simulation of the HWR with a horizontal field.

As the HWR in Figure 3.10 becomes superconducting, the horizontal magnetic field at the location of the fluxgate probes in the inner conductor reduces to about zero, which can be seen from the blue line labeled Bx in Figure 3.11.

QWR Results

For the time-dependent simulations of the QWR cool-downs, the outer conductor is first cooled from bottom to top, followed by the inner conductor which is cooled from top to bottom. For these experiments only two temperature readings are available from the temperature sensors located at the top and bottom of the cavity. This models the assumed cool-down dynamics of the real QWR, which is different from the HWR cool-down sequence in which the inner and outer conductors are both cooled from bottom to top at the same time. The reason for this is that the inner conductor of the QWR is thermally connected only at

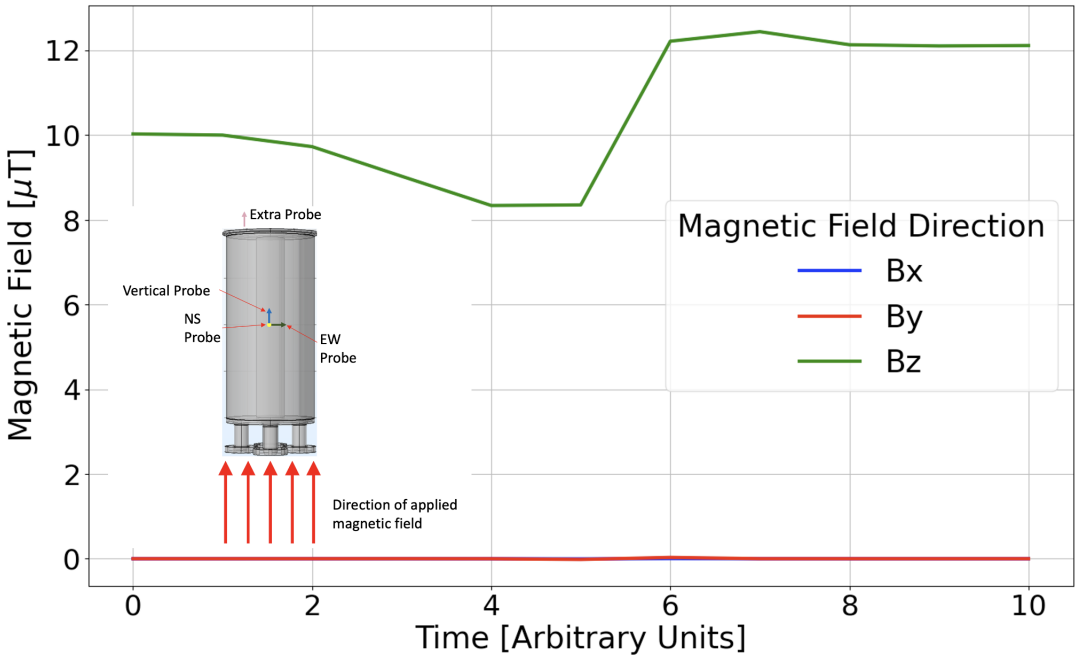

Figure 3.9: Magnetic field in the center of the inner conductor during the time-dependent COMSOL ® simulation of the HWR being cooled down with an applied field in the vertical direction depicted in Figure 3.7. The green line labeled Bz shows the values of the magnetic field in the vertical direction, which is increased by about 20% at the end of the simulation. The magnetic fields in the two horizontal directions are depicted by the blue and red line labeled Bx and By, respectively. These magnetic fields do not have noticeable changes at this scale, thus the blue line is hidden behind the red line.

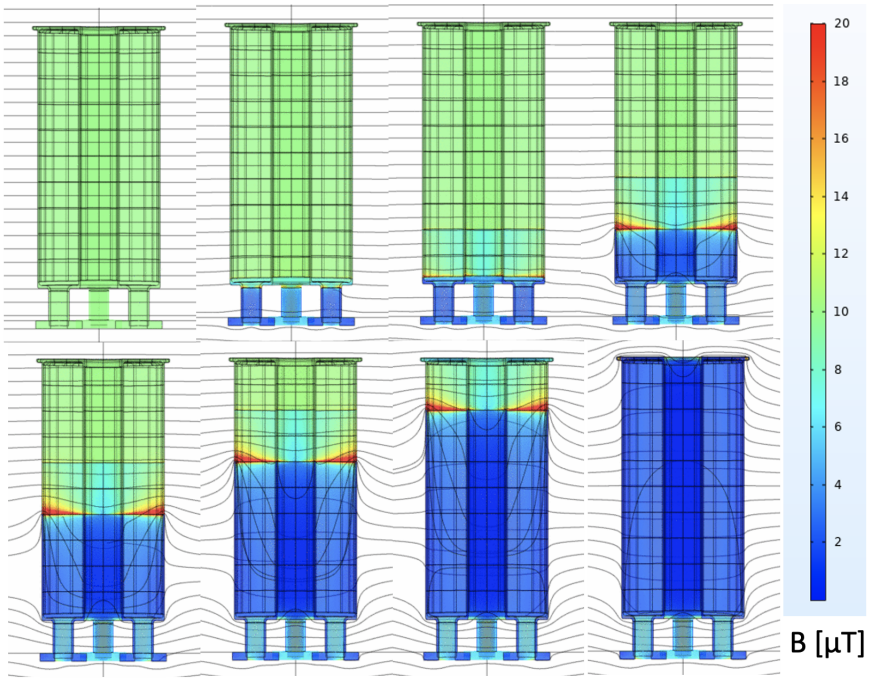

Figure 3.10: Time dependent COMSOL ® simulation of 10 μT applied to the HWR in the horizontal direction as the cavity is cooled from bottom to top. For this field orientation the inner conductor does not see a field enhancement at the end of the simulation because it is shielded by the outer conductor, as is the case with the time-independent simulation.

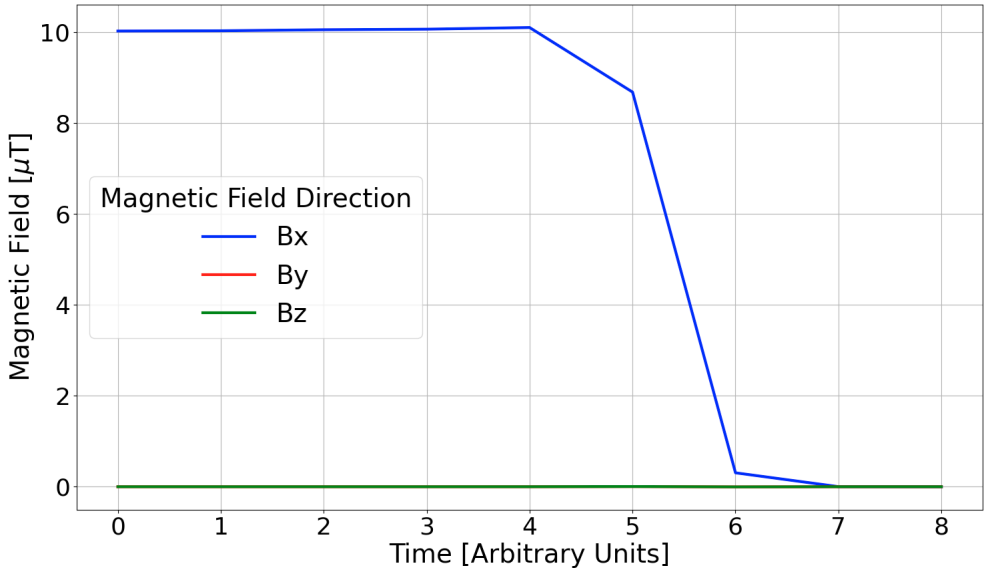

Figure 3.11: Magnetic field in the center of the inner conductor during the time-dependent COMSOL ® simulation of the HWR being cooled down with an applied field in the horizontal direction shown in Figure 3.10. The blue line labeled Bx depicts the magnetic field in the same horizontal direction of the applied field, which is reduced to zero during the simulation. The red and green lines labeled By and Bz represent the magnetic fields in the other two orthogonal spatial directions. The red line is hidden behind the green line.

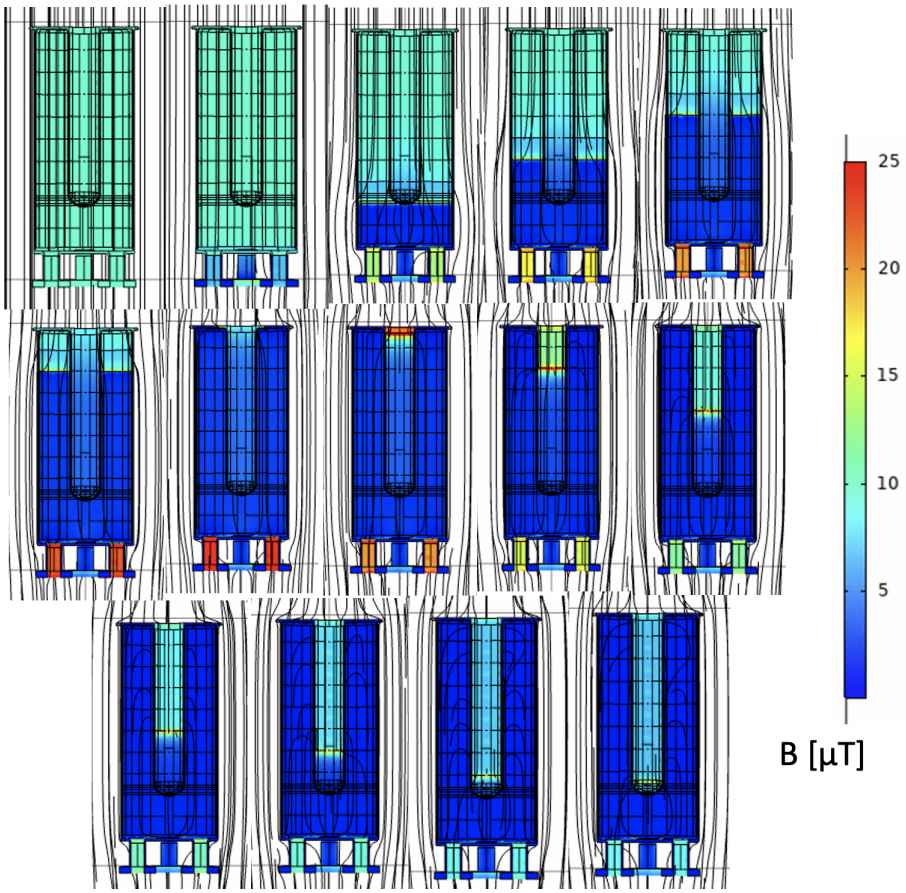

Figure 3.12: Time dependent COMSOL ® simulation of 10 μT applied to the QWR in the vertical direction. The outer conductor is cooled from bottom to top, and then the inner conductor is cooled from top to bottom. As the cavity cools the superconducting front is pushed up the outer conductor and then down the inner conductor.

the top of the cavity, while the HWR's inner conductor is connected at both ends and provides a channel for cold helium gas to flow from the bottom providing a thermal path for conduction cooling. The only thermal path for the QWR's inner conductor to cool down via conduction is from the top since the bottom is blocked from direct helium vapor by the lower flange. Thus, it is assumed that the cold front does not reach the inner conductor while the bottom of the outer conductor is cooled. After the entire outer conductor of the QWR is cooled, the inner conductor can be cooled by conduction from the top of the cavity, and the inner conductor is then cooled from top to bottom.

A simulation of this cool-down with a vertical applied field is shown in Figure 3.12. During the cool-down some flux is pushed down to the tip of inner conductor. At the end of this simulation all magnetic flux disappears, as the inner conductor tip reaches the Meissner state. In reality flux that is forced to the tip of the inner conductor would tend to get trapped since it has nowhere to go. A more realistic end to the simulation would be the second to last time step in which nearly all of the cavity is superconducting but some flux still remains trapped in the tip of the inner conductor. This is a major difference compared to the stationary simulations which show no flux in the inner conductor.

The numerical values of the magnetic fields simulated by COMSOL during the QWR cool-down depicted in Figure 3.12 are plotted in Figure 3.13. Note that some of the simulation timestamp images were omitted from Figure 3.12 for clarity as the area of the tip of the inner conductor is divided into many thin slices. In Figure 3.13 the vertical field, Bz, initially decreases as the outer conductor becomes superconducting. The field then increases as the inner conductor becomes superconducting due to flux being pushed down the inner

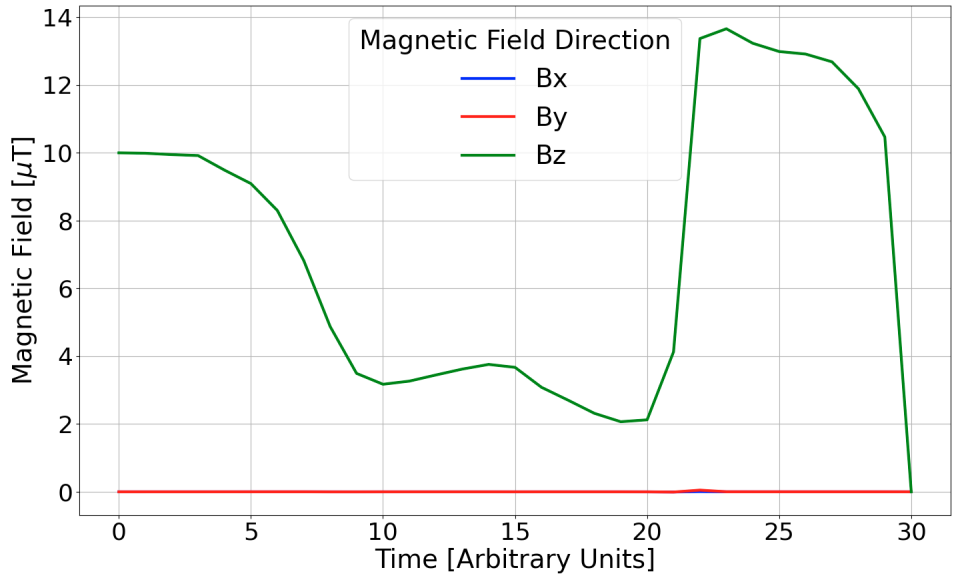

Figure 3.13: Magnetic field in the center of the inner conductor during the time-dependent COMSOL ® simulation of the QWR being cooled down with a vertical applied field depicted in Figure 3.12. The green line labeled Bz represents the magnetic field in the vertical direction, which first decreases as the outer conductor becomes superconducting, and then increases when the superconducting phase front starts to move down the inner conductor. The blue and red lines labeled Bx and By represent the magnetic fields in the horizontal directions. These fields do not show noticeable changes at this scale, so the blue line is hidden behind the red line.

conductor. Near the end of the cool-down the vertical field at the center of the inner conductor decreases as the flux is stopped when the end of the inner conductor becomes superconducting. As mentioned, in reality the flux would tend to get trapped near the end of the inner conductor.

The horizontal QWR cool-down simulation is shown in Figure 3.14. The cavity sections of this simulation become superconducting in the same order as in Figure 3.12 with the outer conductor being cooled from bottom to top followed by the inner conductor being cooled from top to bottom. With the horizontally applied field less flux lines are diverted into the rinse ports or inner conductor. Once the outer conductor passes through transition the simulation results do not change. Therefore, time steps in which the inner conductor is transitioning are omitted from Figure 3.14. This indicates that no flux is moved once the outer conductor is superconducting regardless of the state of the inner conductor. The end of this time-dependent simulation matches the result of the corresponding time-independent simulation.

For the horizontal QWR cool-down, flux does not get pushed down the inner conductor, which can be seen numerically in Figure 3.15. In Figure 3.15, the horizontal field, Bx decreases to about zero as the outer conductor becomes superconducting and does not change as the inner conductor becomes superconducting. For the horizontal simulation flux does not become trapped in the inner conductor since the superconducting outer conductor provides shielding.

3.2.3 Discussion of Simulation Limitations

In the previous simulations there is perfect flux expulsion, which is not the case in actual experiments. In reality the superconductor is imperfect and flux can be trapped in pinning centers or weaknesses in the superconducting topology. Flux enters and is trapped in the material at normal conducting vortices, which are difficult to simulate. COMSOL does not actually simulate a superconductor, but rather a diamagnetic material. Diamagnetic material is similar to a perfect superconductor in that is has near zero magnetic permeability [62], and magnetic flux cannot permeate this material. Hence, COMSOL is considered to be

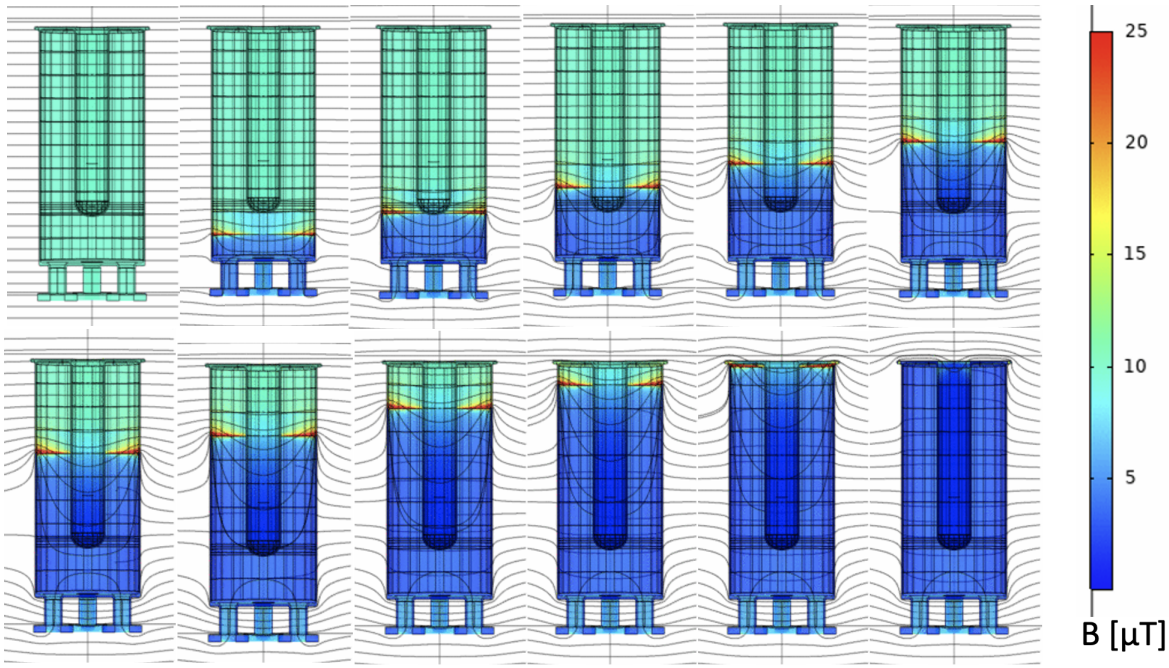

Figure 3.14: Time dependent COMSOL ® simulation of $10\,\mu$T applied to the QWR in the horizontal direction. The outer conductor is cooled from bottom to top, and then the inner conductor is cooled from top to bottom. The superconducting front is not seen going down the inner conductor since the inner conductor is shielded by the outer conductor for the horizontal field orientation.

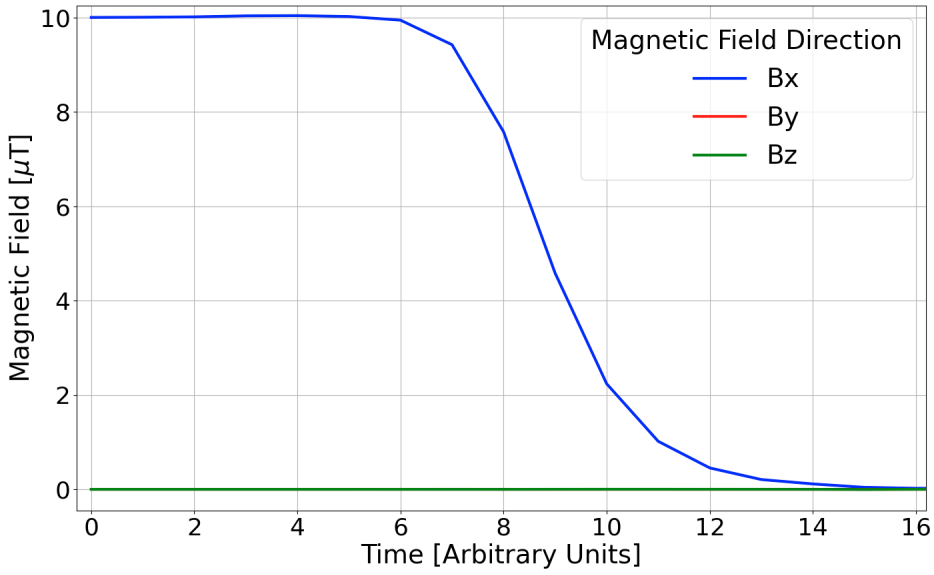

Figure 3.15: Magnetic field in the center of the inner conductor during the time-dependent COMSOL ® simulation of the QWR being cooled down with a horizontal applied field depicted in Figure 3.14. The blue line labeled Bx shows the magnetic field in the same horizontal direction as the applied magnetic field, which decreases to nearly zero as the outer conductor is cooled, and remains the same as the inner conductor is cooled. The red and green lines labeled By and Bz show the magnetic fields in the other two orthogonal spatial directions that do not have an applied magnetic field. The red line is hidden behind the green line.

a simulation of complete flux expulsion for material below the critical temperature. This will be discussed further in the next chapter.

Chapter 4

Results and Discussion

This chapter presents an analysis of cavity cool-down speed, the added surface resistance due to trapped flux, R_{mag}, and rf field dependence. For the cool-down speed analysis the responses of the magnetic field sensors during cool-down and quality factor vs peak rf field curves are compared for fast and slow cool-down rates. R_{mag} is computed for different surface treatments and rf frequencies. The γ coefficients, which are a measure of the field dependence of the surface resistance, are introduced. The γ coefficients for different rf frequencies and surface treatments are compared.

4.1 Magnetic Field Measurements During Cool-down

SRF cavities are typically shielded from surrounding magnetic fields such as the Earth's ambient magnetic field while they are cooled down. This can be achieved with either passive magnetic shielding using high μ metals or active compensation using Helmholtz coils. In the cryostat used for the experiments in this thesis, Helmholtz coils are used to maintain a background magnetic field as close to zero as can reasonably be achieved during some cool-downs. Cavity measurements with these conditions are referred to as zero field cooled (ZFC) and are used as a baseline against which other measurements are compared.

Figure 4.1 shows an example of fluxgate probe data during a cool-down. Three of the fluxgate probes are located in the geometric centres of the cavities inside the inner conductors while one of the fluxgate probes referred to as the extra probe is located on the top plate half way between the inner and outer conductors as shown in Figure 2.8. This example is a dataset from the QWR being cooled with no applied magnetic field. The magnetic fields, represented by dashed lines, are plotted on the left vertical axis in μT while temperature, represented by solid lines, is plotted on the right vertical axis in Kelvin. Both the magnetic field and temperature measurements are plotted over time on the horizontal axis. The horizontal red line is the critical temperature of niobium, 9.2 K. The black and gray solid lines are the measured temperatures of the bottom and top of the cavity, respectively.

The dashed lines representing magnetic fields in Figure 4.1 show changes in the magnetic flux in the cavity happening around the same time as the superconducting transition. In particular, the vertical magnetic field (blue dashed line) shows an increase in magnetic flux, while the extra probe (salmon dashed line) shows a decrease in magnetic flux. The time difference between when the bottom and top of the cavity become superconducting and the speed of the cool-down can be determined from these datasets. The fast cool-downs in this experiment can be characterized by the rate of cooling at transition, dT/dt, and the spatial gradient dT/dz of the temperature across the cavity. This type of dataset is collected for each cool-down through the cavities' critical temperature. In this example dT/dt is 648 mK/min for the top of the cavity, and 545 mK/min for the bottom of the cavity, and dT/dz is 0.10 K/cm given that the top and bottom sensors are 0.4 meters apart.

Fast and slow cool-downs are somewhat arbitrarily defined as having cool down speeds greater than 1,000 mK/min for the fast cool-down, and less than 500 mK/min for the slow cool-down. A cool-down with a speed between 500 and 1,000 mK/min would be considered medium-speed.

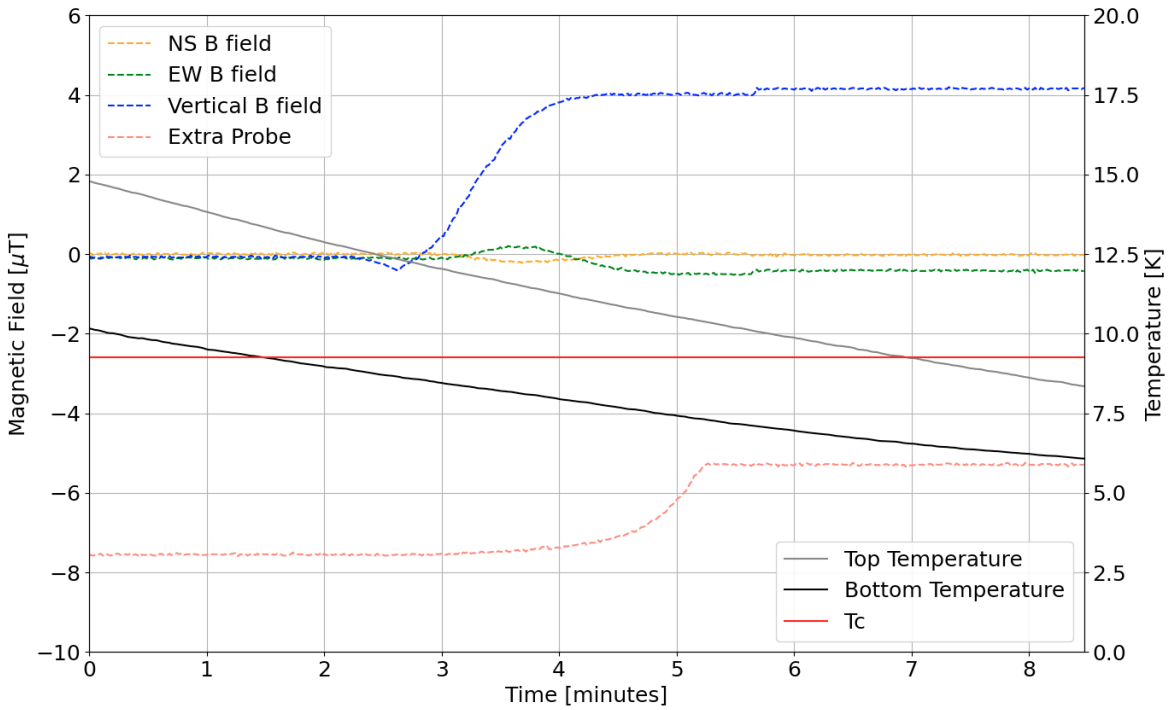

Figure 4.1: Fluxgate probe readings and cavity temperature plotted over time while the QWR cavity is cooled through its critical temperature. The applied field is zero and thus represents the zero field cooled (ZFC) case. The fluxgate probes measure changes in the magnetic fields between the times at which the bottom and top of the cavity become superconducting.

The magnetic field measurements in Figure 4.1 indicate that the magnetic field in the cavity was not zero throughout the entire cavity. This is shown by the jump in field as the cavity enters the Meissner state. The change in magnetic field measured by the extra probe and vertical probe indicate that about 4 μT of flux was moved from one part of the cavity to another during the superconducting transition. In the case of the QWR, it is assumed that the flux is redistributed from the top of the cavity to the bottom of the inner conductor.

The uniformity of the magnetic fields produced by the Helmholtz coils was analyzed in Section 2.3.1. This analysis shows that the magnetic field is homogeneous in the center of the cavity where three of the fluxgate probes are located. However, at the top and bottom of the cavity there are deviations from the average magnetic field by up to about 4 %.

4.2 Measurements of the Cavity Surface Resistance

Table 4.1 is a summary Table of cavity tests that were completed (or not completed) for this thesis. These tests are characterized by different surface treatments applied to the HWR and QWR, as well as the different resonant modes available for each cavity. The fourth column of Table 4.1 lists the magnetic field applied to the cavity for a given test. The label ZFC indicates a Zero Field Cooled magnetic field setting described in Section 4.1. The other magnetic field settings found in the fourth column are the applied field value in either the vertical or horizontal direction relative to the cavity.

The fifth column of Table 4.1 specifies the temperature(s) for which peak rf field and quality factor data are available. The label “4 K” indicates that data was taken while the cavity was at a constant temperature of about 4.3 K, while the label “Cooldown and 2 K” indicates that Q was measured at specific fields as the temperature was lowered. In the latter case a finely resolved Q curve was measured at 2.0 K. Columns six

and seven indicate whether or not this specific test was completed for a fast or slow cooldown, respectively (a green "Y" indicates that the test was completed while a red "N" indicates that the test was not completed). The fast and slow cool-downs will be described in Section 4.2.1. Note that only a small subset of the tests explored the speed of cool-downs - only the QWR after undergoing a baseline treatment and 120 °C bake. The Table will be useful for defining future tests with the cavities. In summary the results in this thesis concentrated on fast and slow cool-downs for the QWR and different heat treatments for the HWR, both with applied magnetic fields in the vertical and horizontal direction.

Surface Treatment	Type of cavity	Modes [MHz]	Applied magnetic field [micro-Tesla]	Temperature Data	Test Completed? (Y/N)	Slow Cooldown Completed?
300C/3hr bake	HWR	389	ZFC	Cooldown and 2K	N	N
				4K	N	N
			10 vertical	Cooldown and 2K	N	N
				4K	N	N
			10 horizontal	Cooldown and 2K	N	N
				4K	N	N
		778	ZFC	Cooldown and 2K	N	N
				4K	N	N
			10 vertical	Cooldown and 2K	N	N
				4K	N	N
			10 horizontal	Cooldown and 2K	N	N
				4K	N	N
		1166	ZFC	Cooldown and 2K	N	N
				4K	N	N
			10 vertical	Cooldown and 2K	N	N
				4K	N	N
			10 horizontal	Cooldown and 2K	N	N
				4K	N	N
	QWR	217	ZFC	Cooldown and 2K	Y	N
				4K	Y	N
			10 vertical	Cooldown and 2K	Y	N
				4K	Y	N
			10 horizontal	Cooldown and 2K	Y	N
				4K	Y	N
		644	ZFC	Cooldown and 2K	Y	N
				4K	Y	N
			10 vertical	Cooldown and 2K	Y	N
				4K	Y	N
			10 horizontal	Cooldown and 2K	Y	N
				4K	Y	N
400C/3rh bake	HWR	389	ZFC	Cooldown and 2K	Y	N
				4K	Y	N
			10 vertical	Cooldown and 2K	Y	N
				4K	Y	N
			10 horizontal	Cooldown and 2K	Y	N
				4K	Y	N
		778	ZFC	Cooldown and 2K	Y	N
				4K	Y	N
			10 vertical	Cooldown and 2K	Y	N
				4K	Y	N
			10 horizontal	Cooldown and 2K	Y	N
				4K	Y	N
		1166	ZFC	Cooldown and 2K	Y	N
				4K	Y	N
			10 vertical	Cooldown and 2K	Y	N
				4K	Y	N
			10 horizontal	Cooldown and 2K	Y	N
				4K	Y	N
	QWR	217	ZFC	Cooldown and 2K	Y	N
				4K	Y	N
			10 vertical	Cooldown and 2K	Y	N
				4K	Y	N
			10 horizontal	Cooldown and 2K	Y	N
				4K	Y	N
		644	ZFC	Cooldown and 2K	Y	N
				4K	Y	N
			10 vertical	Cooldown and 2K	Y	N
				4K	Y	N
			10 horizontal	Cooldown and 2K	Y	N
				4K	Y	N

800C + flash BCP + 120C 48hr bake	HWR	389	ZFC	Cooldown and 2K	Y	N
				4K	Y	N
			10 vertical	Cooldown and 2K	Y	N
				4K	Y	N
			10 horizontal	Cooldown and 2K	Y	N
				4K	Y	N
		778	ZFC	Cooldown and 2K	Y	N
				4K	Y	N
			10 vertical	Cooldown and 2K	Y	N
				4K	Y	N
			10 horizontal	Cooldown and 2K	Y	N
				4K	Y	N
		1166	ZFC	Cooldown and 2K	Y	N
				4K	Y	N
			10 vertical	Cooldown and 2K	Y	N
				4K	Y	N
			10 horizontal	Cooldown and 2K	Y	N
				4K	Y	N
	QWR	217	ZFC	Cooldown and 2K	Y	N
				4K	Y	N
			10 vertical	Cooldown and 2K	N	N
				4K	N	N
			10 horizontal	Cooldown and 2K	N	N
				4K	N	N
		644	ZFC	Cooldown and 2K	Y	N
				4K	Y	N
			10 vertical	Cooldown and 2K	N	N
				4K	N	N
			10 horizontal	Cooldown and 2K	N	N
				4K	N	N
New Baseline	QWR	217	ZFC	Cooldown and 2K	N	N
				4K	Y	N
			40 vertical	Cooldown and 2K	N	N
				4K	Y	N
			20 vertical	Cooldown and 2K	N	N
				4K	Y	N
			40 horizontal	Cooldown and 2K	N	N
				4K	Y	N
		644	ZFC	Cooldown and 2K	N	N
				4K	Y	N
			40 vertical	Cooldown and 2K	N	N
				4K	Y	Y
			20 vertical	Cooldown and 2K	N	N
				4K	Y	N
			40 horizontal	Cooldown and 2K	N	N
				4K	Y	Y
New 120C/48hr bake	QWR	217	ZFC	Cooldown and 2K	N	N
				4K	Y	Y
			40 vertical	Cooldown and 2K	N	N
				4K	Y	Y
			40 horizontal	Cooldown and 2K	N	N
				4K	Y	Y
		644	ZFC	Cooldown and 2K	N	N
				4K	Y	Y
			40 vertical	Cooldown and 2K	N	N
				4K	Y	Y
			40 horizontal	Cooldown and 2K	N	N
				4K	Y	Y

Table 4.1: Summary Table of cavity tests

4.2.1 Fast vs Slow Cool-down

The effects of cool-down speeds and temperature gradients in flux expulsion and trapping has been explored widely in both material samples and elliptical cavities [18, 19, 21, 63]. It was found that for elliptical cavities a fast cool-down leads to more flux expulsion than a slow cool-down. A fast cool-down tends to produce large spatial temperature gradients which produce more efficient flux expulsion. A present speculative interpretation on the role of temperature gradient and cool-down speed is that for certain cavity treatments, after a fast cool-down the superconducting phase front efficiently sweeps out magnetic flux,

whereas a slow cool-down leads to normal conducting "islands" in the cavity where the flux is stuck and it is not energetically favourable for the flux contained in these islands to be expelled [18]. For fast cool-downs and large temperature gradients magnetic flux vortices are de-pinned by the superconducting phase front. The measurements in this section examine the impact of cavity cool-down speed and temperature gradient on flux trapping in coaxial resonators as informed by COMSOL simulations. For this the QWR after a baseline treatment and 48 hour 120 °C bake is used and the impact of a fast and slow cool-down on flux expulsion is presented.

As can be seen in Table 4.1, a sub-set of the experiments include a comparison between fast and slow cool-downs. Specifically, the data was taken for the baseline surface treatment for the 644 MHz QWR mode and for a 120 °C bake for the 217 and 644 MHz modes. In all cases both vertical and horizontal applied fields were considered. The cool-down speed can be manipulated by reducing or increasing the flow of liquid helium into the cryostat [64] and starting the cool-down with a well thermalized cavity just above the transition temperature.

Fast vs Slow Cool-down for Baseline Treatment

The results presented here are from measurements taken of the QWR after a baseline surface treatment. The QWR is cooled down through its critical temperature in the presence of a 40 μT magnetic field applied in the vertical direction for fast and slow cool-downs. The external applied field was set to 40 μT because smaller fields did not have a particularly noticeable effect on the cavity surface resistance at 4 K. The temperature and fluxgate probe readings for these cooldowns are shown in Figures 4.2 and 4.3. For the fast cool-down, the time between the superconducting transitions for the top and bottom of the cavity is four minutes and 32 seconds, and for the slow cool-down it is twelve minutes and twelve seconds. The cool-down speeds of the top and bottom of the cavity for the fast cool-down are 2375 and 3208 mK/min, respectively, while for the slow cool-down these speeds are 337 and 304 mK/min, respectively. The spatial gradients for the fast and slow cool-downs are about 0.56, and 0.13 K/cm, respectively. However, it should be noted that the temperature at the tip of the inner conductor is unknown. The applied vertical field can be seen on the left of the plots where the blue dashed line labeled Vertical B field is at about 40 μT.

Comparatively, the fast cool-downs done by Romanenko et al. have speeds of 1800 to 2400 mK/min while the slow cool-downs had speeds of 120 to 300 mK/min [18]. The cool-downs performed by Vogt et al. had cooling speeds ranging from about 180 to 3000 mK/min [63].

Based on the fluxgate probe readings, both the fast and slow vertical field cool-downs did not lead to strong flux expulsion. After the superconducting transitions the measured vertical fields are increased to 42.5 and 43 μT for the fast and slow cool-downs, respectively. If there were strong flux expulsion, one would expect the vertical magnetic field to get much closer to zero after the superconducting transition. An explanation of this result is that as the cavity is cooled from bottom to top the phase front pushes magnetic flux in front of itself as it moves along the outer conductor and then into the inner conductor. At the end of the cool-down flux is forced towards the tip of the inner conductor, as seen in the COMSOL simulation in Figure 3.12. The second to last time step of the COMSOL simulation shows a moderate field enhancement which is comparable to the experimental results. The last time step of the COMSOL simulation shows perfect flux expulsion, which is not realistic. For this reason the second to last time step is used for comparison. A more detailed comparison between COMSOL and experimental results can be found in Section 4.2.1.

After the fast and slow cool-downs, quality factor measurements are taken in the 644 MHz mode.[1] The cavity was only cooled down to about 4.2 K rather than 2.0 K due to a global helium shortage causing limitations in available helium.

Figure 4.4 shows the cavity surface resistance plotted as a function of peak rf field for ZFC, and 40 μT vertical applied field for fast and slow cool-downs. The datasets for the 40 μT applied fields both have higher surface resistance than the ZFC case. There is no significant difference between the surface resistances for the fast and slow cool-downs. This is consistent with the magnetic field data since neither the fast or slow cool-down showed significant flux expulsion of the 40 μT vertical applied field. A possible explanation is that

[1] Other modes were unavailable due to a malfunctioning of one of the rf amplifiers.

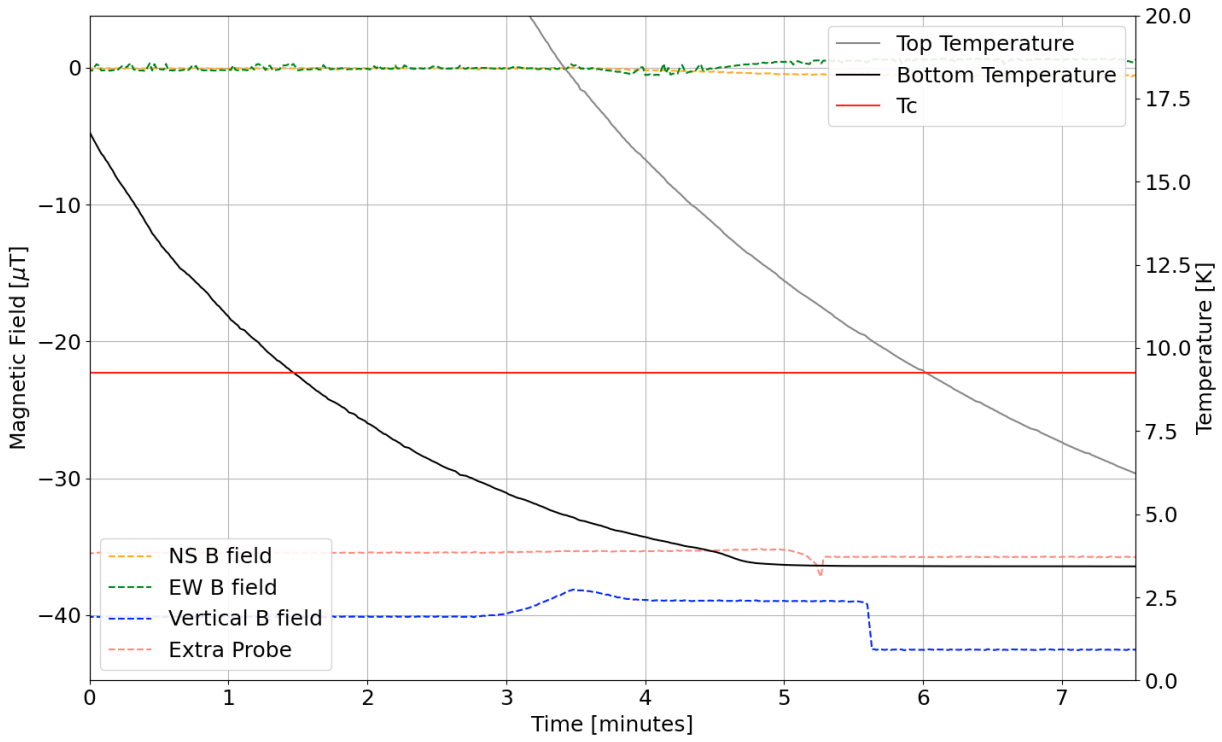

Figure 4.2: Fluxgate probe readings and cavity temperature plotted over time for the baseline treated QWR undergoing a fast cool-down with a vertical applied magnetic field of 40 μT. From the COMSOL simulation an increase in the vertical field of 14 μT would be expected, but only 2.5 μT is measured.

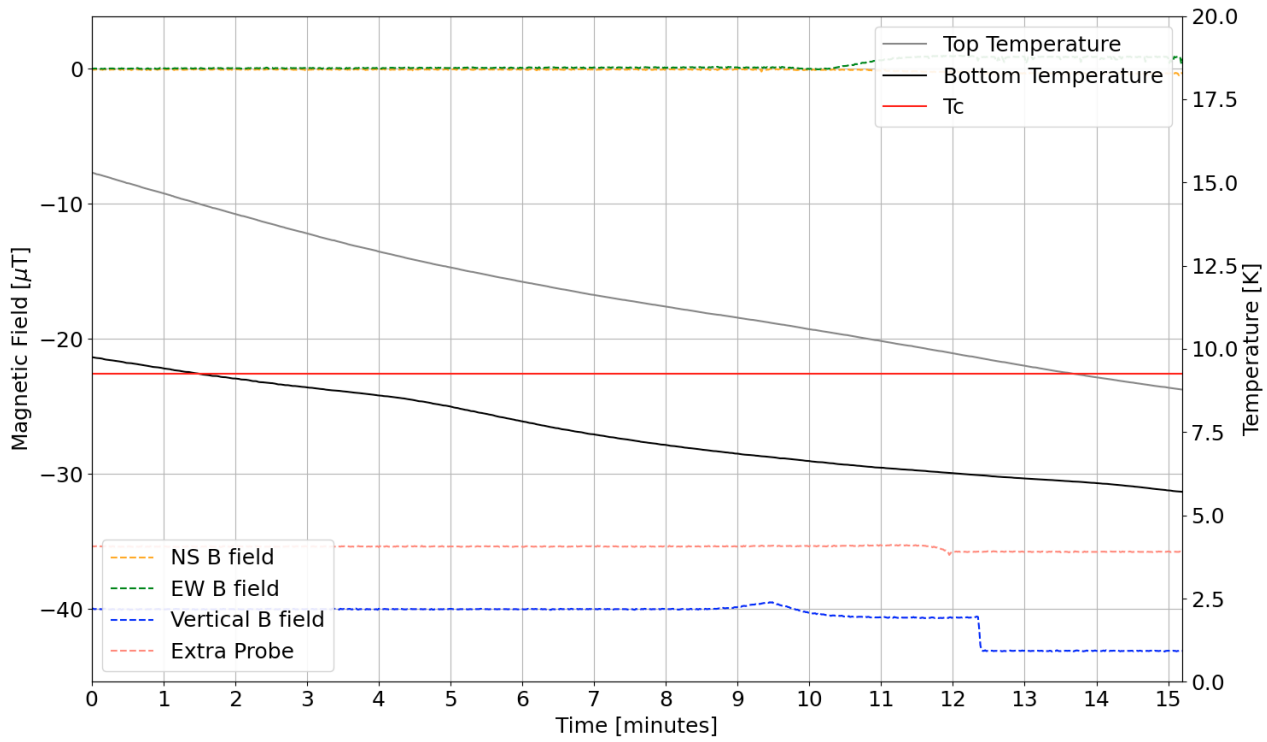

Figure 4.3: Fluxgate probe readings and cavity temperature plotted over time for the baseline treated QWR undergoing a slow cool-down with a vertical applied magnetic field of $40\,\mu$T. A field enhancement of about $3\,\mu$T is measured in the vertical field probe after the superconducting transition.

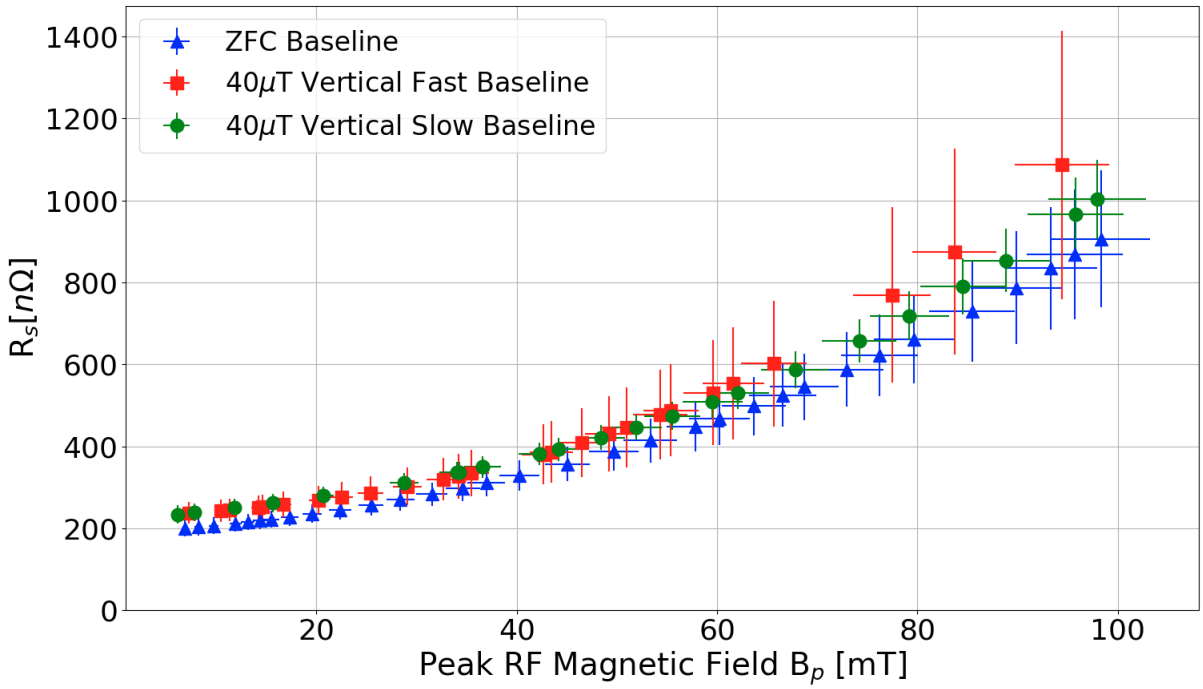

Figure 4.4: Surface resistance as a function of peak rf field for the baseline treated QWR in the 644 MHz mode. The surface resistance is similar for the fast and slow cool-downs, which is consistent with the similar levels of trapped flux observed during the cool-downs.

since the inner conductor is cooled conductively, even though the outer conductor is cooled down in a fast or slow mode, the inner conductor cool-down does not change appreciably, and thus flux trapped in the inner conductor does not change. The error bars in Figure 4.4 come from the standing wave ratio, described in Section 2.5.3, and from the fit functions used in converting R_s^* to R_s, which is described in Section 3.1.1. The uncertainties from the standing wave ratio is a systematic error that will shift each of the three curves in Figure 4.4 by the same amount. Thus the differences between the three curves is more significant than it appears given the error bars. This is also the case for the other plots of R_s as a function of peak rf field in this section.

Fast and slow cool-downs were also done with a horizontal applied magnetic field. The temperature and fluxgate probe readings for these cool-downs are plotted in Figures 4.5 and 4.6. The spatial gradients of the fast and slow cool-downs are about 0.66 and 0.11 K/cm, respectively. The applied horizontal field can be seen on the left of the plots where the green dashed line labeled EW B field is at about 40 μT. The cool-down speeds of the top and bottom of the cavity for the fast cool-down are 2766 and 4326 mK/min, respectively, while for the slow cool-down these are 301 and 225 mK/min, respectively. For the fast cool-down the time between superconducting transitions at the top and bottom of the cavity is four minutes and seventeen seconds, and for the slow cool down it is thirteen minutes and seven seconds.

For the fast cool-down, as the cavity is cooled through its superconducting temperature, the horizontal field drops down below 5 μT. This is a demonstration of very strong flux expulsion in which most of the magnetic flux in the cavity is expelled during the superconducting transition. The results of the slow cool-down are significantly different from the results of the fast cool-down. For the slow cool-down the horizontal field is only reduced to about 28 μT. The COMSOL simulation simulates perfect superconducting behavior with no flux trapping. Thus, if the experimental results differ from the COMSOL simulation, that is an indication that flux trapping has occurred. It has been shown in COMSOL simulations that the flux reaching the inner conductor is expelled as the outer conductor transitions into the Meissner state from bottom to top. This removal of flux is thought to be more effective for the fast cool-down because the larger temperature gradient helps overcome the pinning force and reduces flux trapping [19, 20]. Any flux reaching the inner

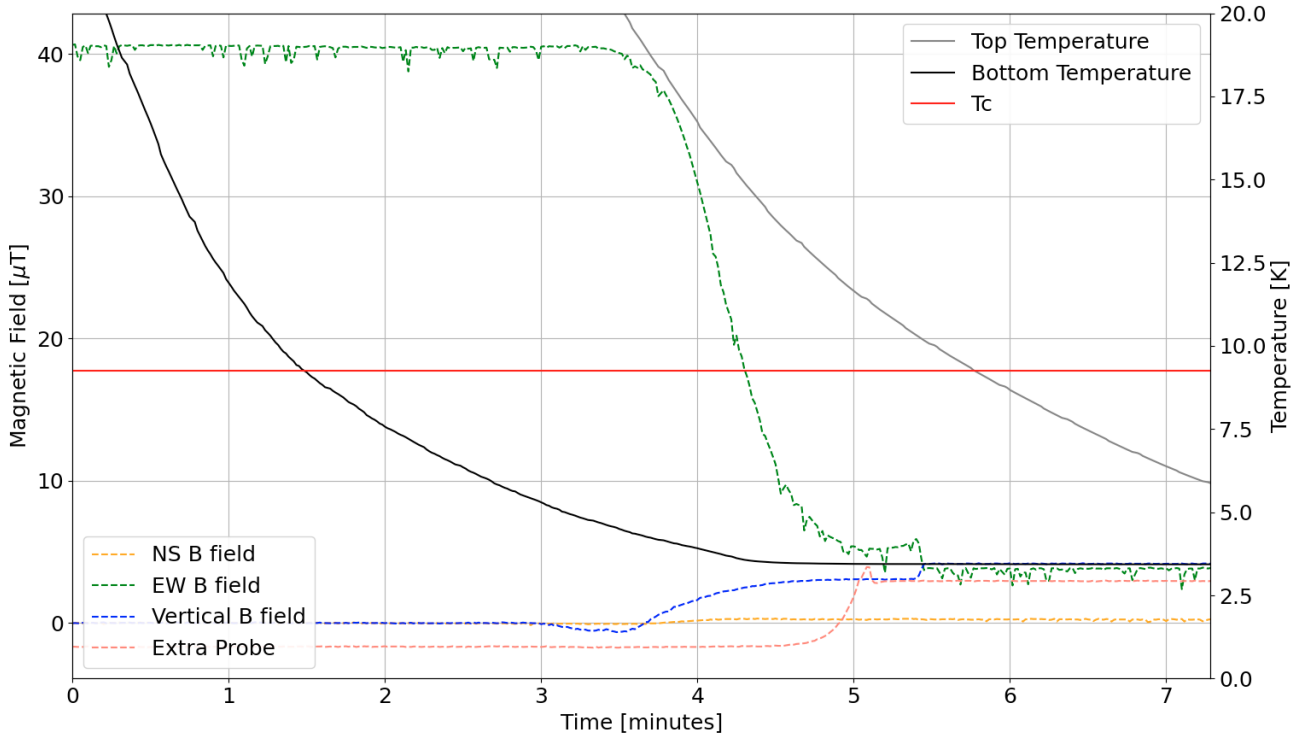

Figure 4.5: Fluxgate probe readings and cavity temperature plotted over time for the baseline treated QWR undergoing a fast cool-down with a horizontal applied magnetic field of 40 μT. Very strong flux expulsion is observed during the superconducting transition as the vertical field goes from about 40 to 5 μT.

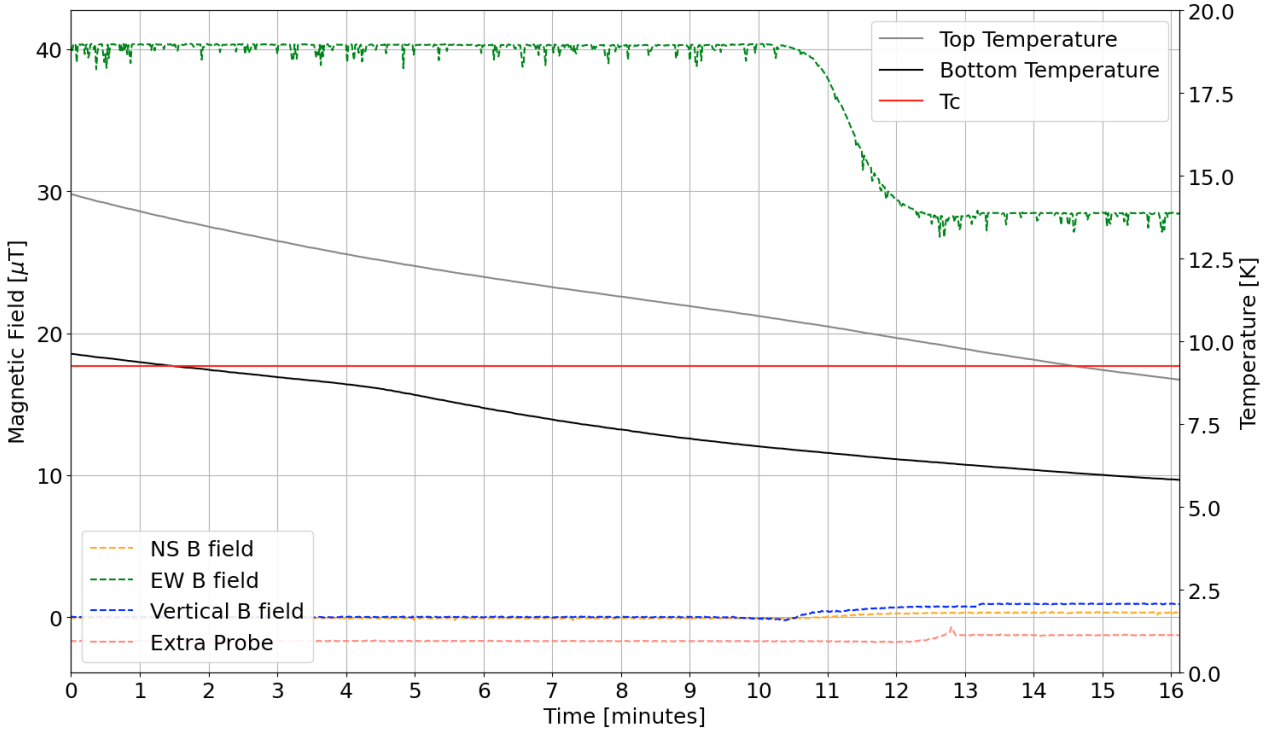

Figure 4.6: Fluxgate probe readings and cavity temperature plotted over time for the baseline treated QWR undergoing a slow cool-down with a horizontal applied magnetic field of 40 μT. This cool-down results in much less flux expulsion than the fast horizontal cool-down, and only about 11 μT of flux is expelled.

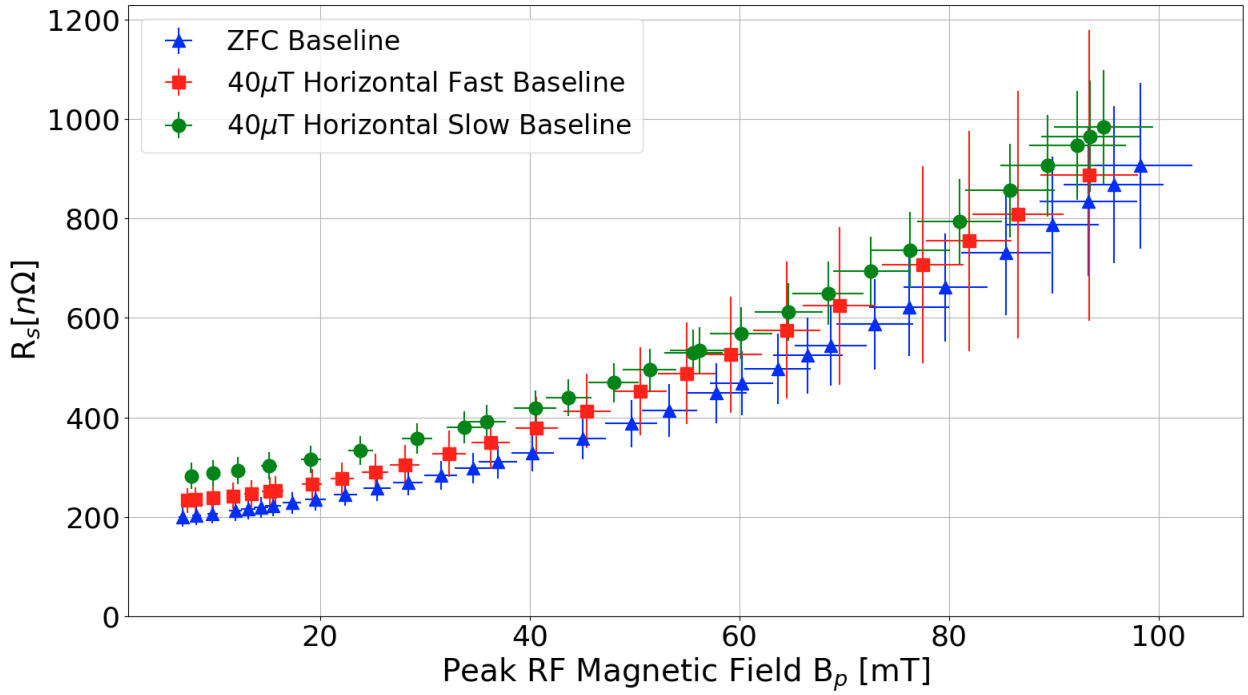

Figure 4.7: Surface resistance as a function of peak rf field for the baseline treated QWR in the 644 MHz mode. The slow cool-down shows somewhat higher surface resistance than the fast cool-down indicating that more flux was trapped in the cavity after the slow cool-down.

conductor is a sign that flux trapping has occurred. It is though that for the fast horizontal cool-down most flux does not reach the inner conductor.

The horizontal field cooled surface resistance results for the fast and slow cool-downs are plotted in Figure 4.7. As with the vertical applied field case, both the fast and slow horizontal applied field data sets both have higher surface resistance than the ZFC data set. However, for the horizontal applied field, the slow cool-down leads to significantly higher surface resistance than the fast cool-down. This is because the fast cool-down is better at expelling flux from the cavity than the slow cool-down, as noted in the cool-down data analysis.

Fast vs Slow Cool-down for 120 °C Bake

Similar measurements were done with the same QWR after a 120 °C bake. Figures 4.8 and 4.9 depict the temperature and fluxgate probe readings for the QWR during fast and slow cool-downs, respectively, in the presence of a 40 μT magnetic field applied in the vertical direction. The QWR was cooled down through its critical temperature after undergoing a 120 °C bake. The time between the superconducting transitions for the top and bottom of the cavity was two minutes and seven seconds for the fast cool-down and three minutes and 40 seconds for the slow cool-down. The cool-down speeds for the top and bottom of the cavity during the fast cool-down were 6119 and 6767 mK/min, respectively, while during the slow cool-down they were 219 and 250 mK/min, respectively. The spatial gradients for the fast and slow cool-downs were approximately 0.53 and 0.022 K/cm, respectively.

According to the fluxgate probe readings, neither the fast nor the slow vertical field cool-downs resulted in significant flux expulsion. Instead, a moderate field enhancement was observed in the vertical field, which is evident in the right-hand side of the plots shown in Figures 4.8 and 4.9, where the vertical field measurement exceeds 40 μT. The fast cool-down results in a larger field enhancement compared to the slow cool-down. This result is nearly identical to the behavior observed in the vertical cool-downs after a baseline treatment described previously. The most significant difference in the vertical field cooled results for the

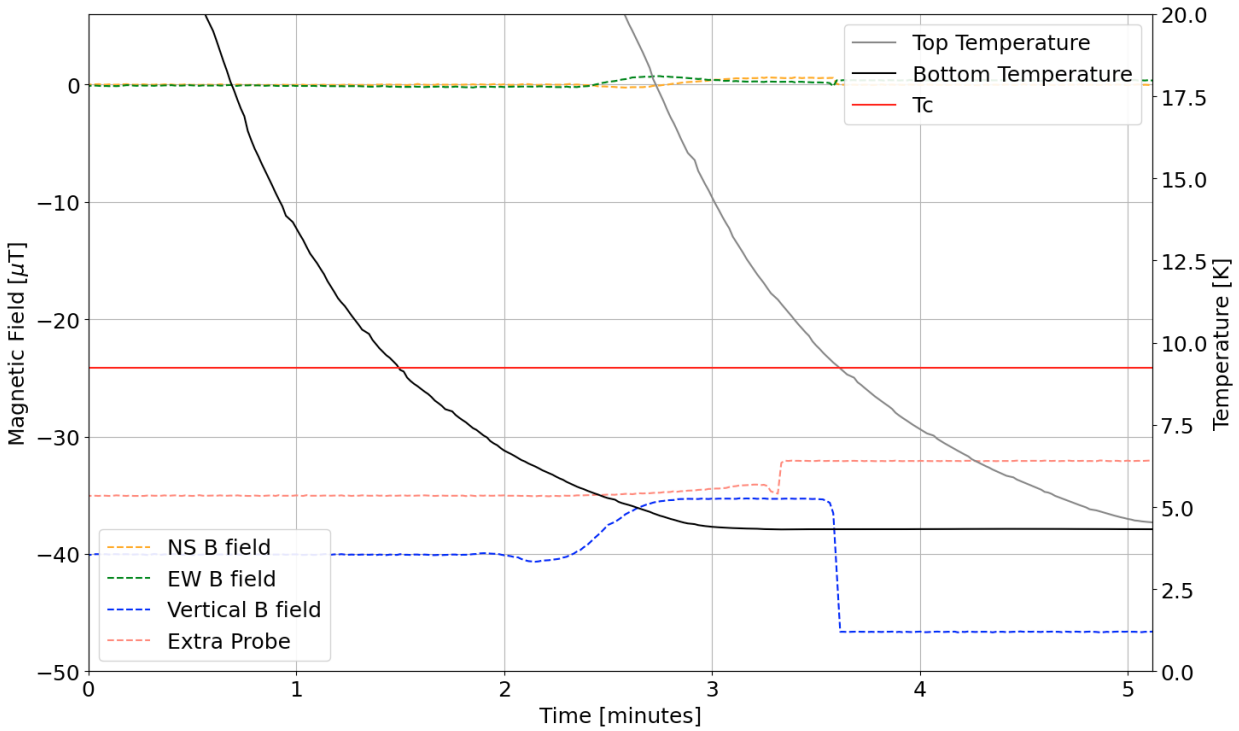

Figure 4.8: Fluxgate probe readings and cavity temperature plotted over time for the 120 °C baked QWR undergoing a fast cool-down with a vertical applied magnetic field of 40 μT. From the simulation an increase in the vertical field of 14 μT would be expected, but only about 7 μT is measured.

baseline treatment and 120 °C bake is that the fast cool-down for the baseline treatment resulted in a field enhancement of about 7 μT, while the fast cool-down for the 120 °C bake showed a field enhancement of about 2.5 μT.

After the fast and slow cool-downs, quality factor measurements are taken in the 217 and 644 MHz mode at 4.2 K. The surface resistance of the QWR in the 217 MHz mode is plotted as a function of peak rf field along with 40 μT vertical applied fields for fast and slow cool-downs in Figure 4.10. No significant difference in surface resistance is observed between the fast and slow cool-downs. This is in agreement with the magnetic field data, which indicates that both the fast and slow cool-downs result in comparable small field enhancements.

The surface resistance for the 644 MHz mode is shown in Figure 4.11. The fast and slow cool-downs do not show a significant difference in surface resistance. This is consistent with observations from the 217 MHz mode and the baseline treatment data.

The QWR underwent fast and slow cool-downs with a horizontally applied magnetic field. The cool-down speeds for the top and bottom of the cavity during the fast cool-down were 5203 and 6680 mK/min, respectively, while during the slow cool-down these were 233 and 251 mK/min, respectively. The time elapsed between the superconducting transitions at the top and bottom of the cavity was two minutes and nine seconds for the fast cool-down and three minutes and 30 seconds for the slow cool-down. Spatial temperature gradients of approximately 0.51 and 0.022 K/cm were observed for the fast and slow cool-downs, respectively. These cool-down characteristics are similar to the ones obtained for the vertical cool-downs, and are plotted in Figures 4.12 and 4.13. For the horizontal applied field, there is very strong flux expulsion in the fast cool-down, and significantly less flux expulsion for the slow cool-down. This is very similar to the results of the horizontal cool-down performed after the baseline treatment.

Figures 4.14 and 4.15 depict the surface resistances for the fast and slow cool-downs with a horizontal

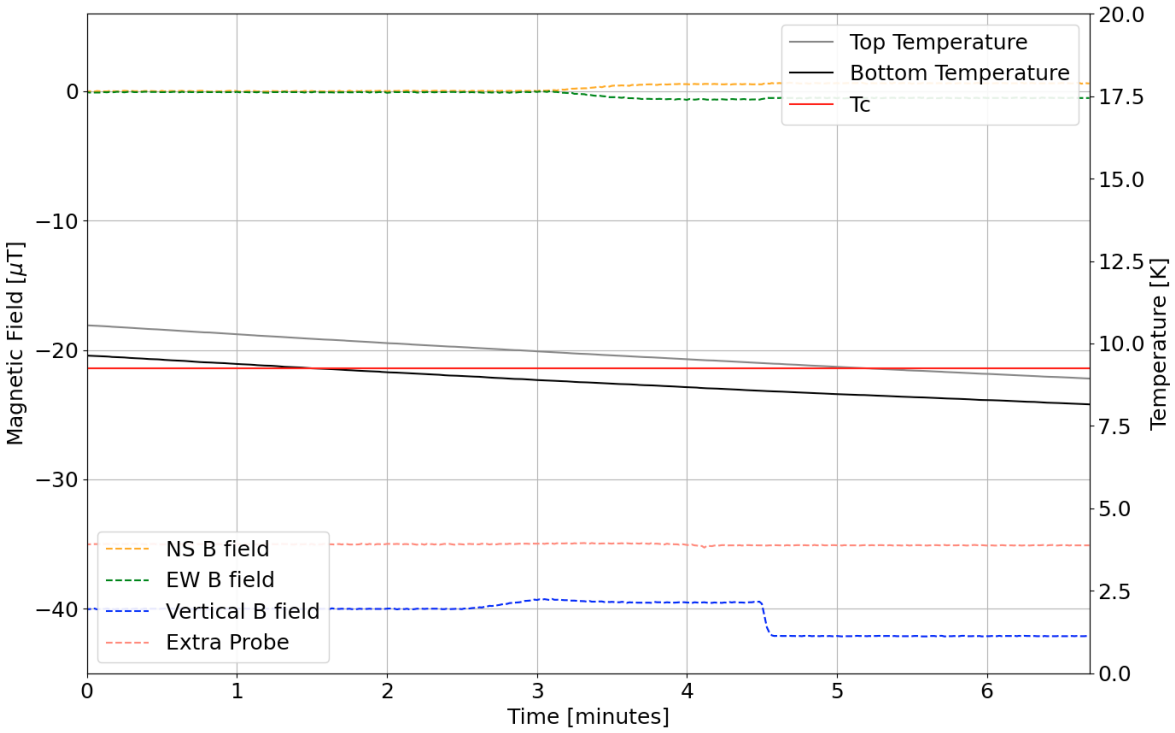

Figure 4.9: Fluxgate probe readings and cavity temperature plotted over time for the 120 ℃ baked QWR undergoing a slow cool-down with a vertical applied magnetic field of 40 μT. A small enhancement of the vertical field is observed for this cool-down.

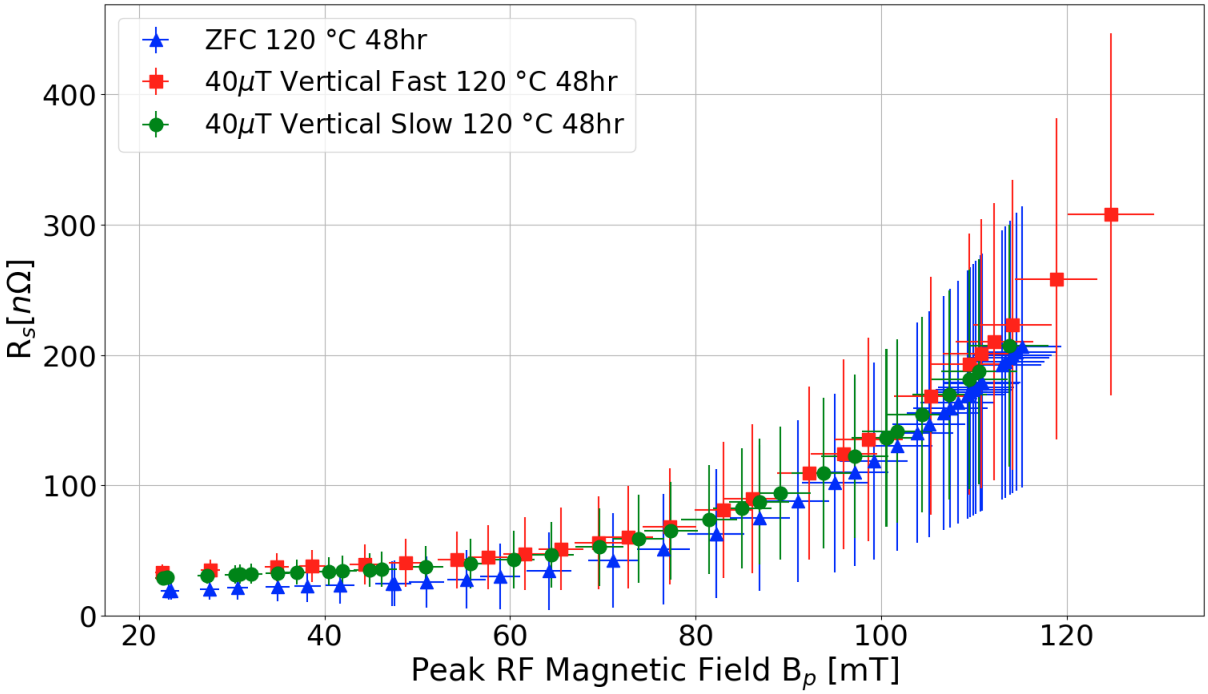

Figure 4.10: Surface resistance as a function of peak rf field for the 120 ℃ baked QWR in the 217 MHz mode. The fast and slow cool-downs show similar values of surface resistance. The large error bars are due to the difficulty in fitting the data to a polynomial function.

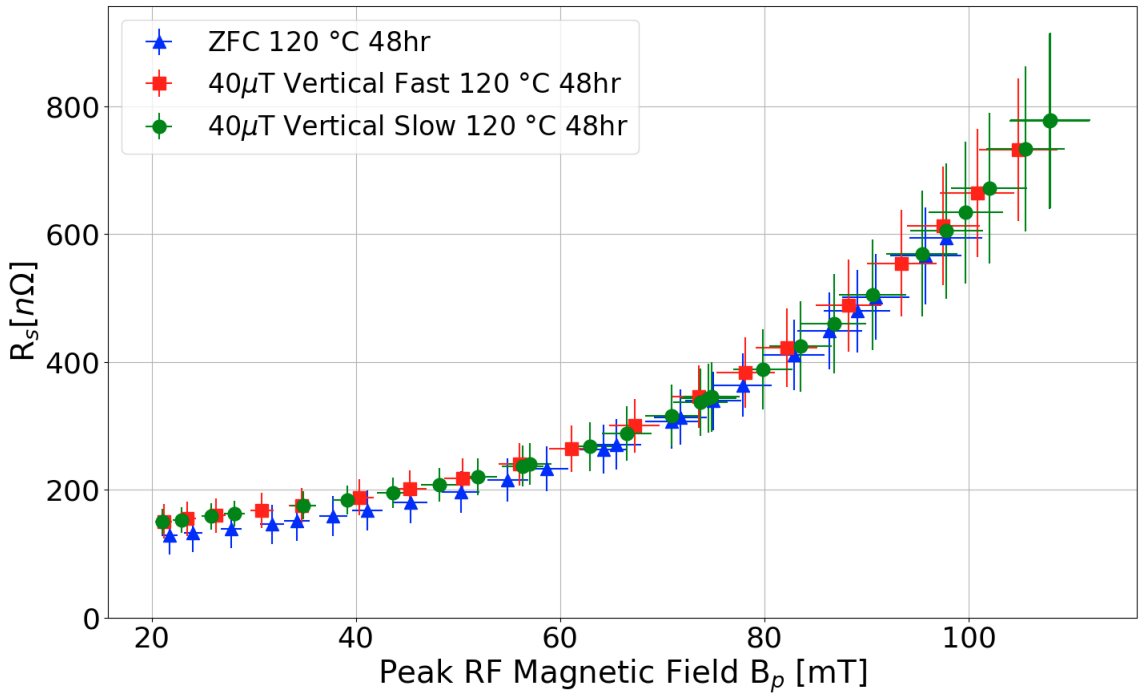

Figure 4.11: Surface resistance as a function of peak rf field for the 120 °C baked QWR in the 644 MHz mode. There is no significant difference in surface resistance between the fast and slow cool-downs for the vertical applied field.

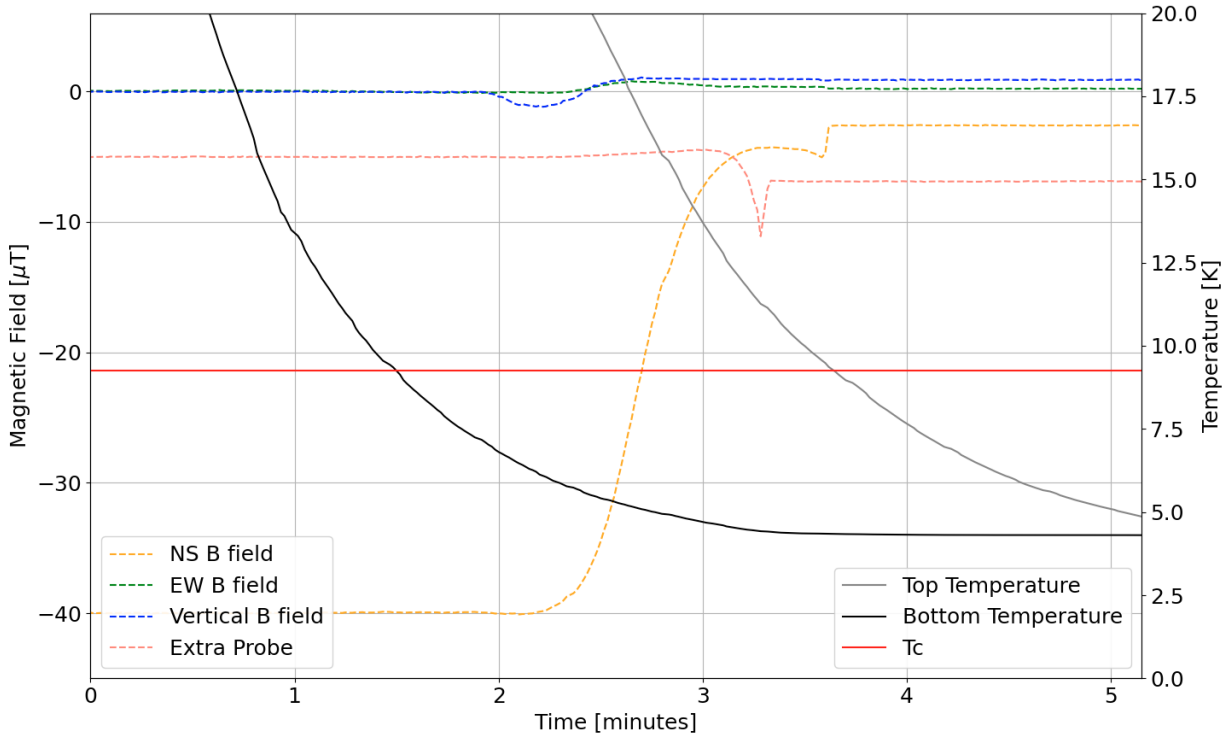

Figure 4.12: Fluxgate probe readings and cavity temperature plotted over time for the 120 °C baked QWR undergoing a fast cool-down with a horizontal applied magnetic field of 40 μT. This result is consistent with the baseline horizontal fast cool-down shown in Figure 4.5 in which there is about 95 % flux expulsion.

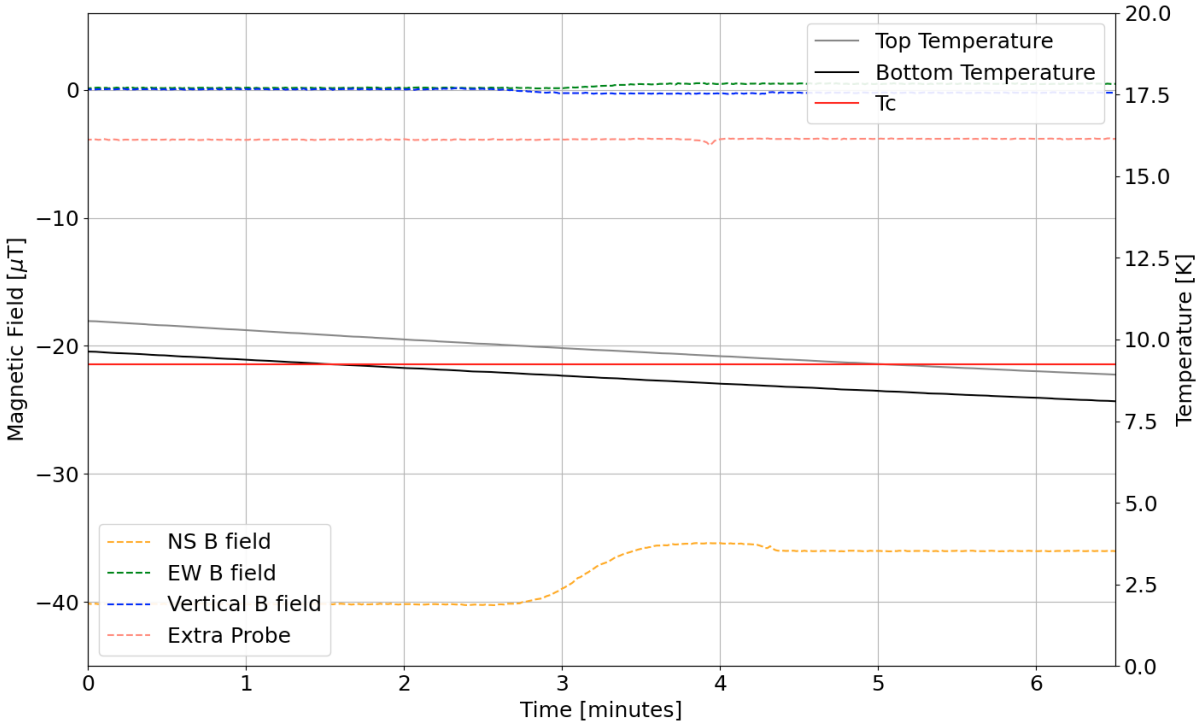

Figure 4.13: Fluxgate probe readings and cavity temperature plotted over time for the 120 °C baked QWR undergoing a slow cool-down with a horizontal applied magnetic field of 40 μT. Much less flux trapping is observed for this slow cool-down compared to the fast horizontal cool-down in Figure 4.12.

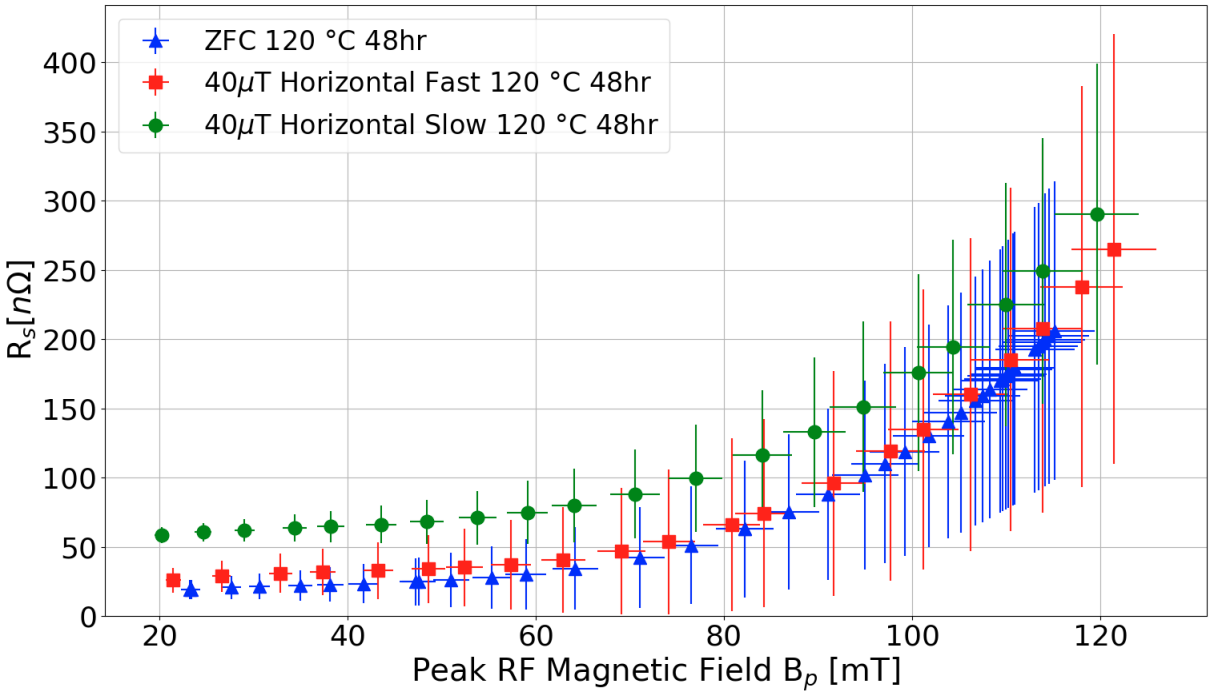

Figure 4.14: Surface resistance as a function of peak rf field for the 120 °C baked QWR in the 217 MHz mode. The slow cool-down has higher surface resistance than the fast cool-down which can be attributed to greater flux trapping for the slow cool-down compared to the fast cool-down.

applied field for cavity frequencies of 217 and 644 MHz, respectively. For the 217 MHz mode, there is a notable difference between the two cool-downs in which the slow cool-down exhibits significantly higher surface resistance than the fast cool-down. This can be attributed to the fact that the fast cool-down is more effective at expelling flux from the cavity. The surface resistance data for the 217 MHz mode has larger error bars due to difficulties in fitting the G/Q data to polynomial functions as described in Section 3.1.1. For the 644 MHz mode, slow cool-down also results in higher surface resistance than the fast cool-down

When comparing magnetic field and surface resistance measurements for different resonant modes, it is illustrative to see how strong the rf magnetic fields are at the location of the fluxgate probes. If flux is trapped in a region with a higher rf field it is more likely to affect the quality factor of the cavity because more power is dissipated into regions with high rf fields since the power dissipated is the product of the surface resistance and the square of the rf magnetic field. Figure 4.16 depicts a heat map of the rf magnetic field for the two investigated modes of the QWR, with the location of the fluxgate probes shown as a red circle. At the location of the fluxgate probes, the rf magnetic fields are higher for the 644 MHz mode compared to the 217 MHz mode.

The time-dependent COMSOL simulations do not take into account the cool-down speeds. It is insightful to compare the results of the fast vs slow cool-down experiment to the time-dependent COMSOL simulations of the QWR being cooled down in a vertical or horizontal applied field, shown in Figures 3.12 and 3.14, respectively.

Comparison Between Simulation and Measurement

The results of the COMSOL simulation and fluxgate probe measurements for the vertical and horizontal cool-downs after a 120 °C bake are plotted together in Figures 4.17 and 4.18, respectively. The COMSOL simulation results were previously presented in Figures 3.13 and 3.14, while the fast and slow cool-down results were presented in sub-Section 4.2.1. The COMSOL and experimental results are plotted here again so that they may be easily compared. The left sides of the plots in Figures 4.17 and 4.18 with a timestamp

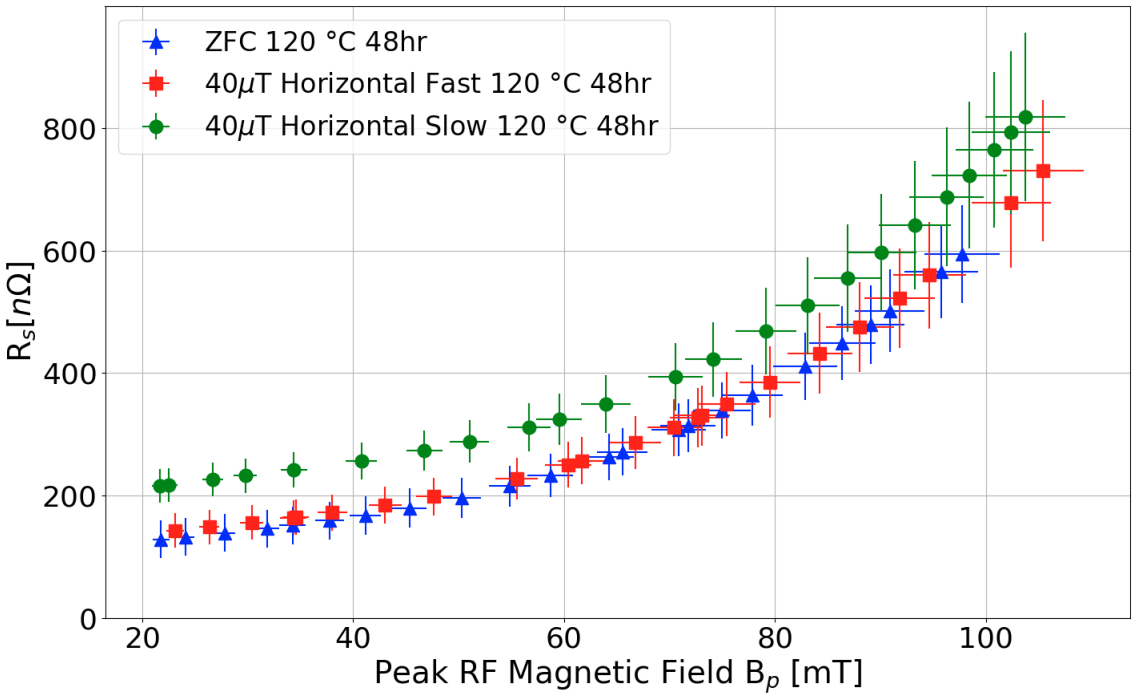

Figure 4.15: Surface resistance as a function of peak rf field for the 120 °C baked QWR in the 644 MHz mode. The slow cool-down leads to higher surface resistance than the fast cool-down due to an increase in trapped flux.

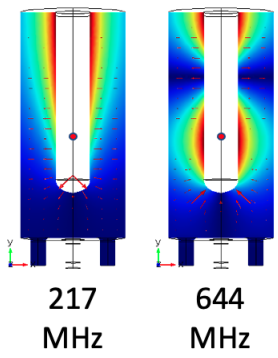

Figure 4.16: Magnetic field distribution for the fundamental 217 MHz mode (left) and next highest mode of 644 MHz (right) for the QWR. The location of the fluxgate probe in the inner conductor is shown as a red circle. The fluxgate probes are situated in a location in which the rf fields are higher for the 644 MHz mode.

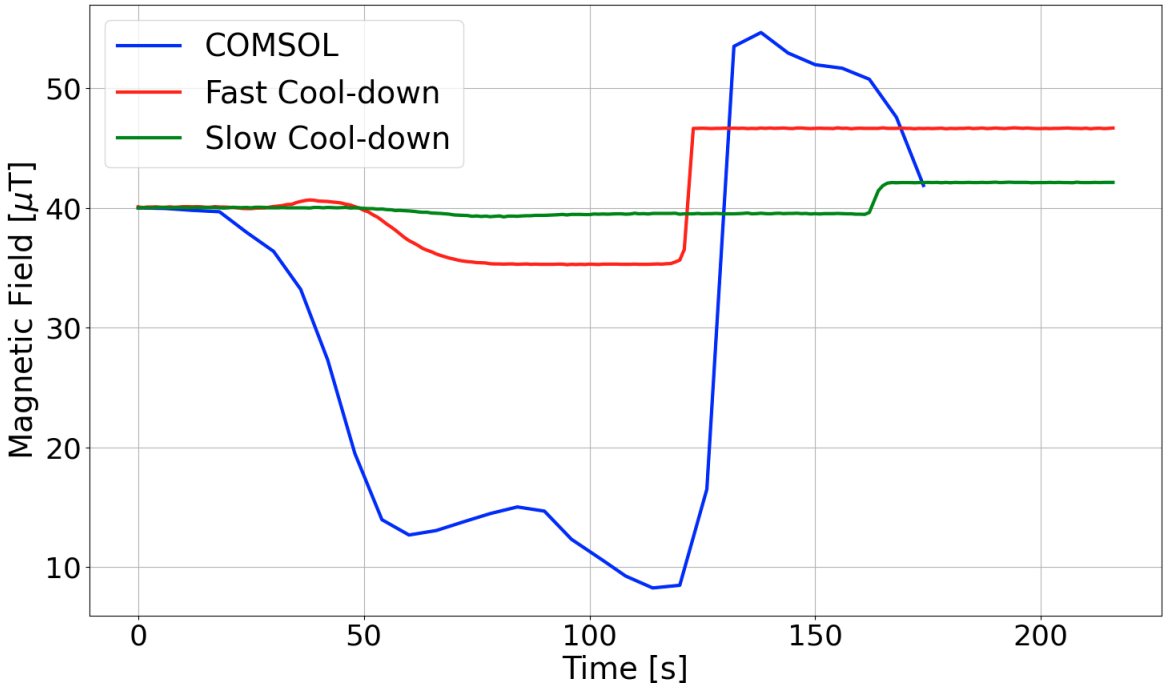

Figure 4.17: Results of the QWR vertical cool-down COMSOL simulation and 120 ℃ bake experimental results. The COMSOL simulation shows much higher variation in the magnetic field during the cool-down compared to the experimental results indicating that flux is being trapped for both the fast and slow cool-down.

of zero correspond to when the bottom of the cavity starts to become superconducting. The ends of the datasets on the right of the plots correspond to the end of the cool-down or cool-down simulation when the entire cavity is superconducting. The fast cool-down dataset is shorter than the slow cool-down dataset since a fast cool-down takes less time than a slow cool-down. For the COMSOL simulations the horizontal axis has been re-scaled to correlate with the experimental data since simulation time steps are arbitrary.

For the vertical cool-down in Figure 4.17, moving from left to right, both the fast cool-down and COMSOL simulation show a dip in the magnetic field. This dip in magnetic field is due to flux being forced around the cavity after the bottom plate becomes superconducting. This dip is much larger for the COMSOL simulation compared to the experimental result, which is thought to be because flux is trapped in the lower plate and outer conductor of the cavity during the cool-down, resulting in more flux being measured in the inner conductor. The slow cool-down does not have a significant dip in magnetic field, which may be due to flux being trapped in the top plate. Later in simulation and real cool-downs, a final field enhancement occurs after the top plate is cooled and flux near the top plate is forced into the inner conductor. This final field enhancement is also larger for the COMSOL simulation than for the measured cool-downs. This may be because some flux is trapped in the top plate during the actual cool-downs. These differences is simulated and actual magnetic field measurements indicate that there is localized rather than uniform flux trapping.

For the vertical field cooled results shown in Figure 4.17, in the final state of the simulation the magnetic field in the inner conductor goes to zero since COMSOL does not simulate flux trapping. The actual magnetic field data is much different than the simulation for the final state with the simulation predicting no flux in the inner conductor. In reality flux is forced into the tip of the inner conductor and is trapped. The simulation also predicts a larger field enhancement in the inner conductor compared to the experimental data since more flux is pushed into the inner conductor in the COMSOL simulation. An additional notable aspect of the QWR cool-downs is that the inner conductor is cooled conductively and is unaffected by the cool-down speed.

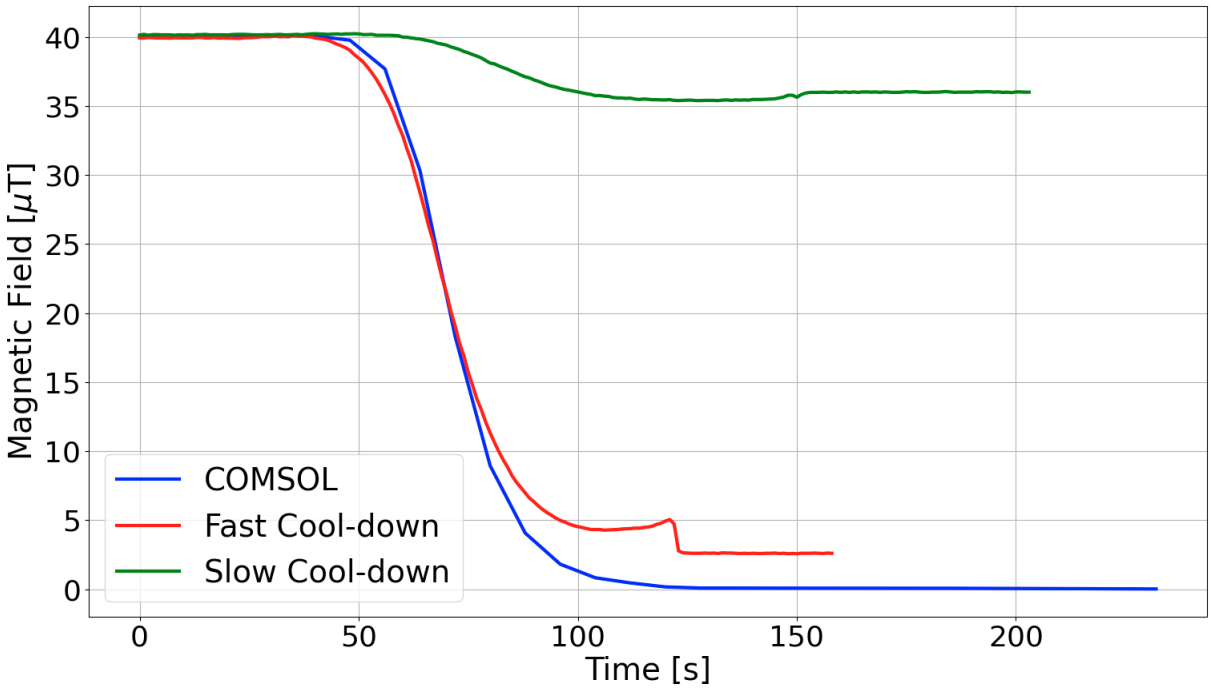

Figure 4.18: Results of the QWR horizontal cool-down COMSOL simulation and 120 °C bake experimental results. The results of the fast cool-down are similar to the COMSOL simulation, with the exception that the simulation shows complete flux expulsion.

For the simulated and measured magnetic fields for the horizontal cool-downs after a 120 °C bake plotted in Figure 4.18. At the beginning of these cool-downs the magnetic field remains at about 40 μT. After about 50 seconds, the magnetic field for the fast cool-down is quickly reduced to about 5 μT which closely matches the simulation until the end of the cool-down, which indicates that most of the flux is expelled in the fast cool-down. The simulated magnetic field is reduced to zero since COMSOL simulates a perfect superconductor with no flux trapping. The slow cool-down result is quite different than the simulation, as the magnetic field is only reduced to about 35 μT, indicating that most of the flux is trapped.

In the case of the QWR, the vertical field simulation shows some field enhancement in the inner conductor at the approximate location of the fluxgate probes as the inner conductor is becoming superconducting, as shown in Figure 3.12. Numerical analysis from COMSOL indicates that during the cool-down the center of the inner conductor sees a maximum field enhancement of about 35 % when the superconducting phase front is passing by the center of the inner conductor, whereas just before the last time step the simulated field enhancement is 5 %.

The magnetic field measurements for the 120 °C bake show an enhancement of 17.5 % in the case of a fast cool-down, and 5 % in a slow cool-down, shown in Figures 4.8 and 4.9, respectively. Meanwhile, the results form the baseline treatment exhibit enhancements of about 6 and 7.5 % for the fast and slow cool-downs, respectively, as depicted in Figures 4.2 and 4.3. A speculative explanation for this difference is that in the case of the 120 °C bake, the fast cool-down is more effective at moving flux from the top plate into the inner conductor. This means that some flux is trapped and not forced around the material by the Meissner effect.

The fast horizontal cool-downs saw about a 90 and 95 % reduction of the magnetic field in the inner conductor for the baseline treatment and 120 °C bake, respectively. The field reduction with the slow horizontal cool-down is much lower compared to the simulation and only produced a field reduction of about 28 % for the baseline treatment, and 10 % for the 120 °C bake. This means that significant flux was trapped in the case of the slow cool-down and much less flux was trapped in the fast cool-down. These results are summarized in Table 4.2.

Applied Magnetic Field Direction	Vertical	Horizontal
Simulation results after final time step	- 100%	- 100%
Simulation results before final time step	+ 5%	-100%
Largest simulation field enhancement	+ 35%	0%
Fast cool-down results Baseline	+ 6%	- 90%
Fast cool-down results 120 ℃ Bake	+ 17.5%	- 95%
Slow cool-down results Baseline	+ 7.5%	- 28%
Slow cool-down results 120 ℃ Bake	+ 5%	- 10%

Table 4.2: Comparison of the change in magnetic field in the inner conductor of the QWR after a simulated or actual cool-down in the presence of a vertical or horizontal applied magnetic field. The plus or minus signs in front of the percentages denote relative increases or decreases in the magnetic field, respectively. The listed increases and reductions are relative to the initial applied magnetic field of 40μT.

4.3 RF Field Dependence

There are many factors that can cause surface resistance in SRF cavities, and one of them is the rf magnetic field. This rf field dependence is responsible for a decrease in quality factor with gradient, known as a "Q-slope". The field dependence of surface resistance may be caused by magnetic flux entering the bulk through defects in the niobium where there are small normal conducting regions [65]. The increase in surface resistance with rf field may also be caused by thermal feedback in which the temperature of the cavity surface increases due to rf heating, while the rf heating increases with the surface temperature [66]. Recent results from McMullin indicate that in coaxial cavities the Q-slope is partially caused by thermal feedback while there is also some additional field dependence [67].

For the TRIUMF coaxial cavities, the surface resistance depends strongly on the rf field amplitude, as has been shown in Figure 3.1, which is reproduced in Figure 4.19. One way to quantify this field dependence is with a quadratic function,

$$R_s = R_{0\gamma}\left(1 + \gamma\left(\frac{B_p}{B_0}\right)^2\right) \tag{4.1}$$

where $R_{0\gamma}$ is the zero-field resistance and is a free fit parameter, B_0 is a normalizing factor equal to 100 mT, and γ is a fit parameter that defines the level of field dependence. The γ factors have been a way to characterize the medium field Q slope in coaxial cavities operating at 4.2 K [68].

In this study the focus lies on how the γ factors change as a function of temperature. In order to extract the temperature dependent γ coefficients it is necessary to first compute the surface resistance as a function of temperature as in Figure 4.19. The next step is to extract some R_s values from the BCS fits for some fixed temperatures, plot them as a function of B_p, and fit these data points to equation 4.1. An example of these extracted $R_s(B_p)$ values is shown in Figure 4.20. The $R_s(B_p)$ values in this example were extracted from the fits of Figure 4.19. The values circled in red in Figure 4.20 are the γ coefficients from equation 4.1. In this Section γ coefficients are compared for different cavity treatments and resonant frequencies for the HWR.

Resolved as a function of temperature, the γ coefficients show how the rf field dependence changes with temperature. Figure 4.21 shows an example of γ coefficients plotted as a function of temperature for the HWR in the 389 MHz mode for three different treatments: the baseline treatment, a 400 ℃ 3 hour bake, and a 120 ℃ 48 hour bake. The cavity was cooled down with the ZFC setting for each of these data sets. The baseline heat treatment has consistently larger γ coefficients, and thus has a more pronounced Q-slope. For the baseline treatment and 400 ℃ 3 hour bake, the γ coefficients increase linearly with temperature. For the 120 ℃ bake, the γ coefficients increase linearly with temperature along with the 400 ℃ bake data points until a temperature of about 2.8 K, at which the γ coefficients for the 120 ℃ bake start to plateau. This

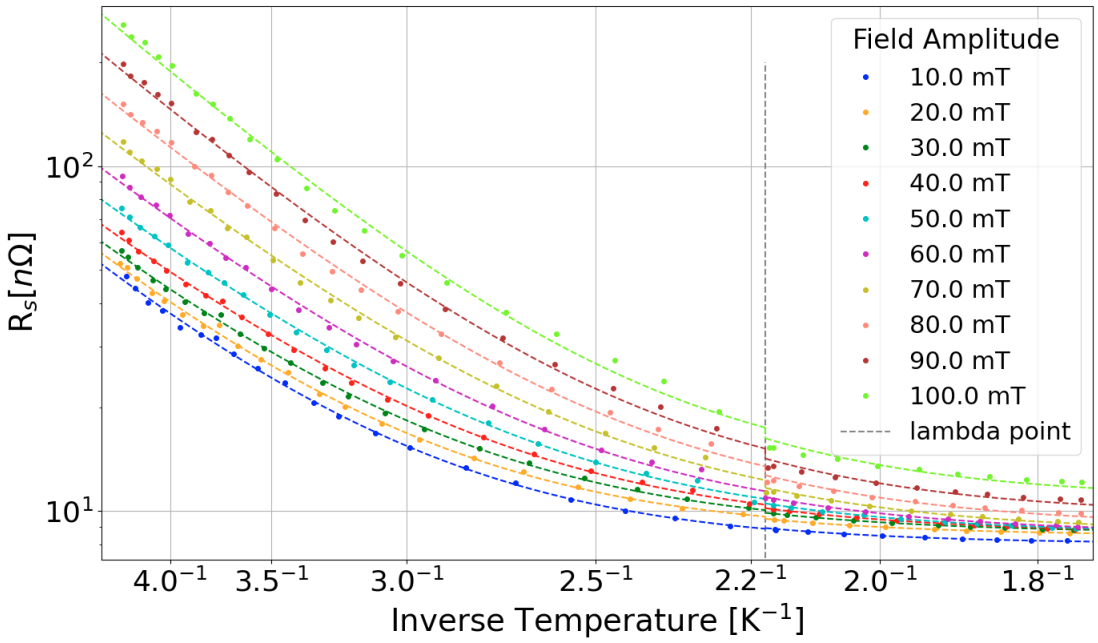

Figure 4.19: R_s vs inverse temperature data set from the HWR in the 389 MHz mode fitted to the BCS formula. The vertical gray line marks the helium superfluid transition temperature, at which there is a discontinuity in the R_s values. When the helium is in a superfluid state there is more efficient heat transfer between the cavity and the helium, leading to lower surface resistances.

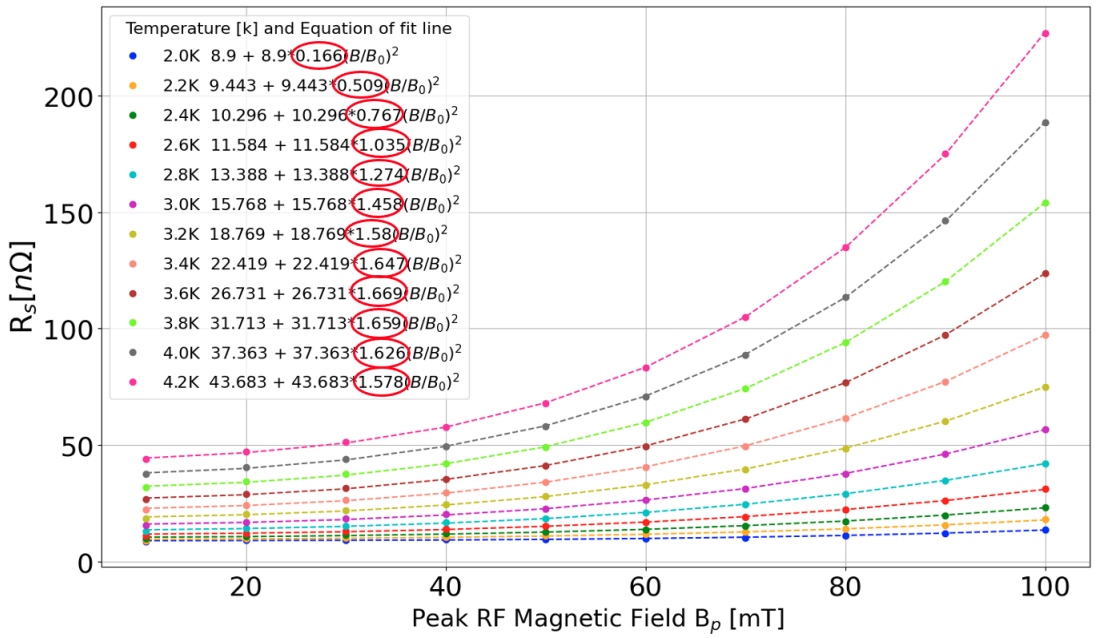

Figure 4.20: $R_s(B_p)$ values extracted from BCS formula fits and fitted to equation 4.1. The values in red circles are the γ coefficients.

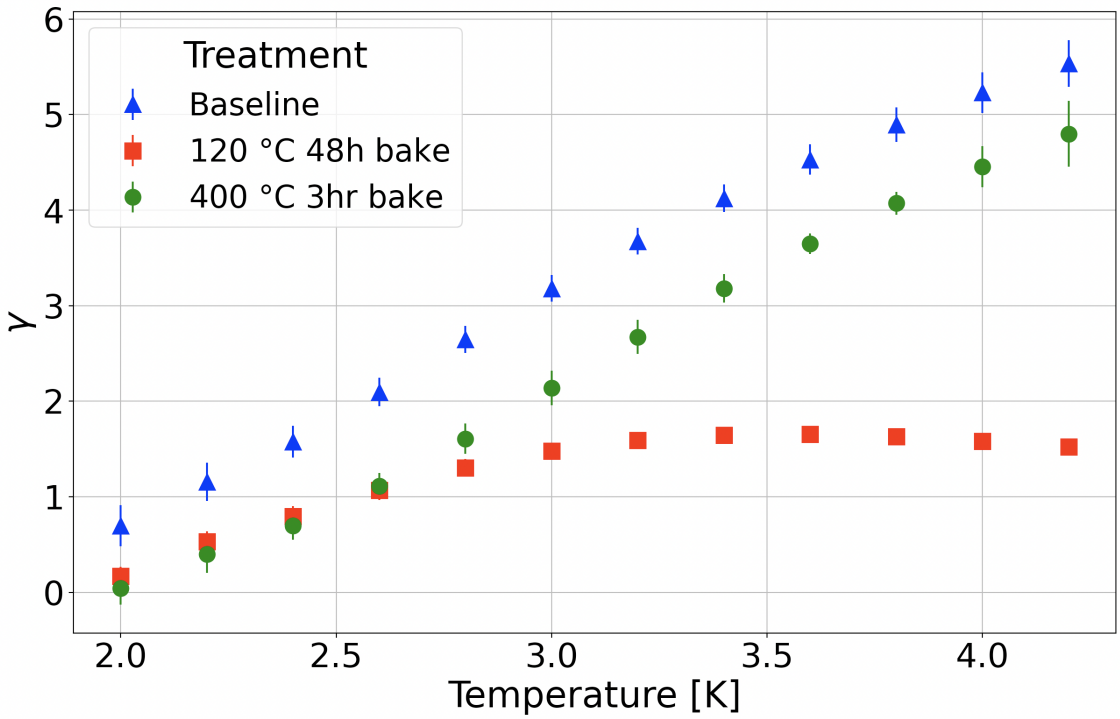

Figure 4.21: These γ coefficients are from the HWR in the 389 MHz mode after different heat treatments. For the baseline and 400 °C three hour bake the γ coefficients increase linearly with temperature. For the 120 °C 48 hour bake the γ coefficients are similar to those of the 400 °C bake until the temperature approaches 3 K, at which point the γ coefficients plateau.

means that after a 120 °C bake the HWR will have a reduced Q-slope above 3 K compared to the baseline treatment and 400 °C bake, at least in the 389 MHz mode.

The zero field resistance $R_{0\gamma}$ in equation 4.1 is plotted in Figure 4.22 for the same three cavity treatments. At temperatures above 2.8 K the 120 °C bake has lower $R_{0\gamma}$ values compared to the other two treatments. For the baseline treatment and 400 °C bake the γ coefficients and $R_{0\gamma}$ values are larger for higher temperatures compared to the 120 °C bake. This indicates that the baseline treated and 400 °C baked HWR has an increased sensitivity to the BCS (temperature dependent) resistance, since the BCS resistance dominates at higher temperatures.

The frequency dependence of the γ coefficients is explored in Figure 4.23, which shows γ coefficients plotted as a function of temperature for the HWR after a 120 °C 48 hour bake for three different modes: 389, 778, and 1166 MHz. The 389 MHz mode data was plotted previously in Figure 4.21, and is included in Figure 4.23 in order to compare γ coefficients for different modes rather than cavity treatments. For most temperatures the higher frequencies have higher γ coefficients. For the 389 and 778 MHz modes the γ coefficients increase with temperature until about 3 K, after which the γ coefficients level off and start to decrease slightly, especially for the 778 MHz mode. The γ coefficients for the 1166 MHz mode show a different trend in which γ starts decreasing significantly with temperature after about 3 K.

The surface resistance vs temperature curves in Figure 4.19 show a discontinuity in the surface resistance at the λ point for liquid helium, which is 2.17 K, and is described in Section 3.1.2. The discontinuity in the surface resistance is referred to as ΔR_s, and can be extracted from the fits done on equation 3.6. This discontinuity has been noted by several authors and is hypothesized as being due to an improved heat transfer between the helium and the rf surface for temperatures below the lambda point [67].

The ΔR_s values are plotted as a function of peak rf magnetic field for the 389, 778, and 1166 MHz modes of the 120 °C baked HWR in Figure 4.24. ΔR_s tends to increase with cavity frequency. For the 778 and

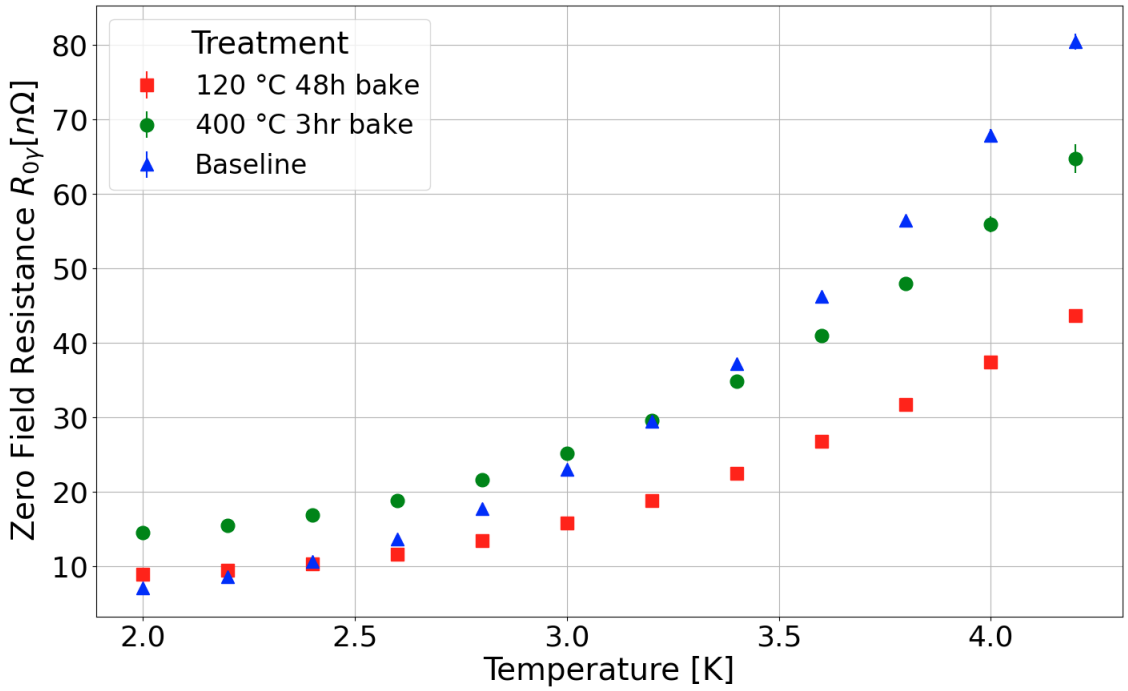

Figure 4.22: Zero field resistance from the HWR in the 389 MHz mode after different heat treatments. These values were extracted from the same fits used find the γ coefficients plotted in Figure 4.21. For all treatments, the zero field resistance increases with temperature. For the 120 °C bake, $R_{0\gamma}$ is lower compared to the other two treatments after the temperature reaches about 3 K.

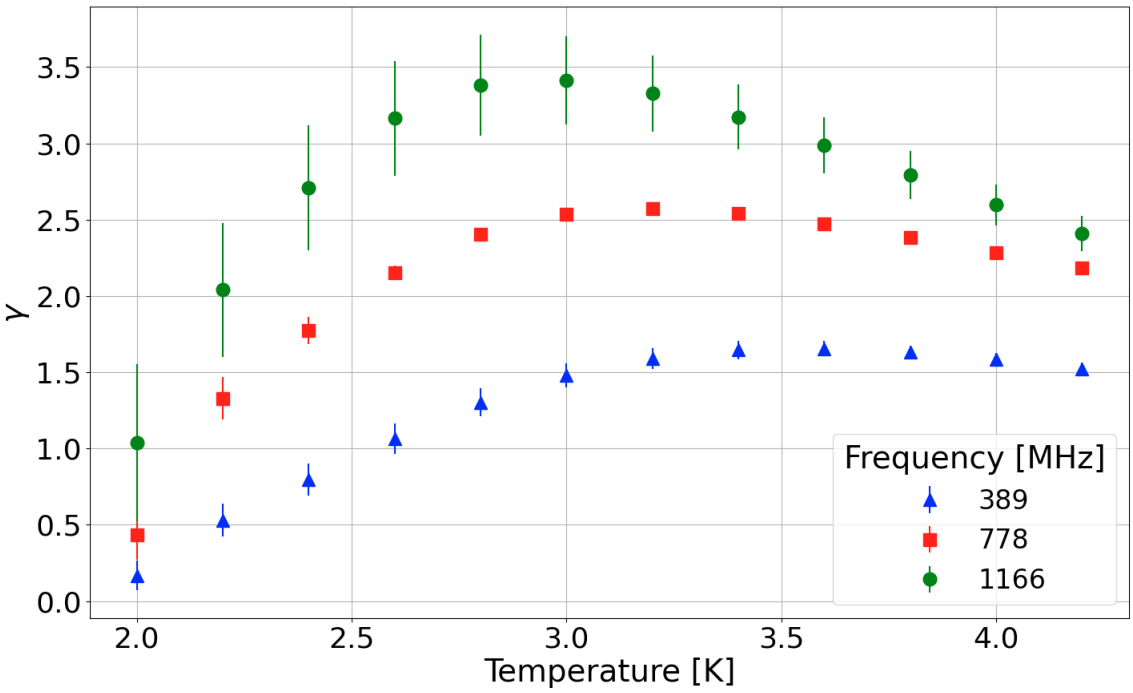

Figure 4.23: These γ coefficients are from the HWR in the 389, 778, and 1166 MHz modes after a 120 °C 48 hour bake. For the most part the γ coefficients increase with cavity frequency.

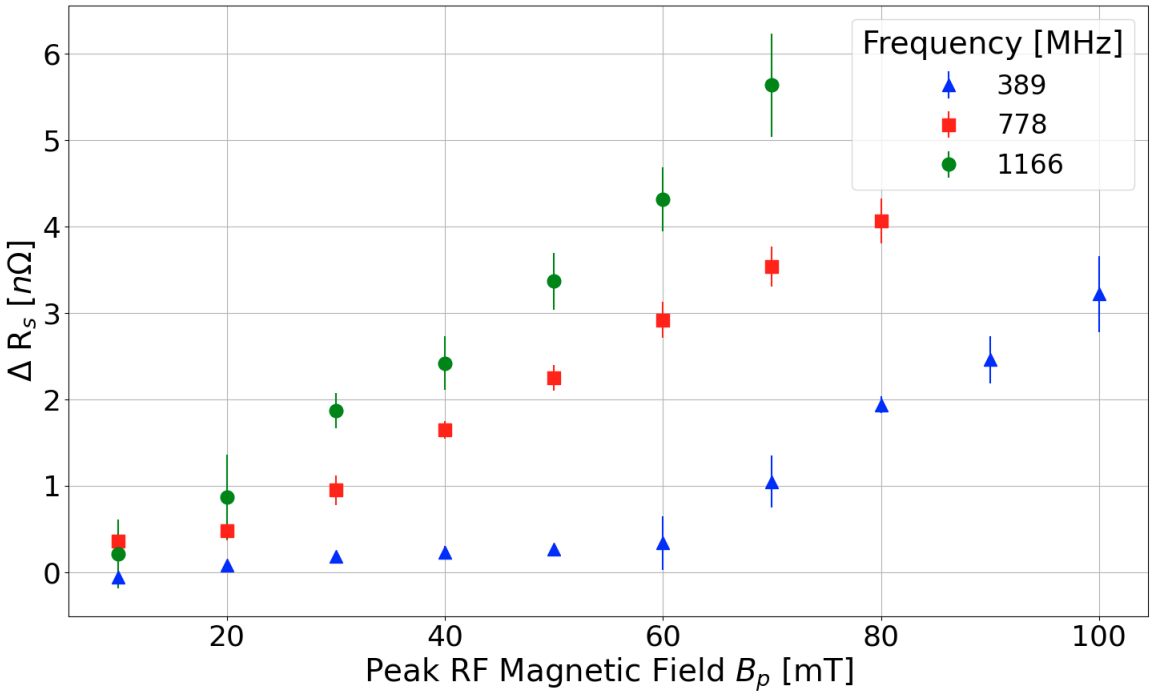

Figure 4.24: ΔR_s is the difference in surface resistance just before and just after the liquid helium lambda point. The ΔR_s values are plotted for all three measured modes of the HWR after a 120 °C bake. The fundamental mode has ΔR_s values near zero for peak rf magnetic fields below 70 mT. ΔR_s generally increases with cavity frequency.

1166 MHz modes, ΔR_s increases approximately linearly with peak rf field. For the 389 MHz mode, the ΔR_s values are close to zero below 70 mT, and then increase linearly from 70 to 100 mT. The increase of ΔR_s with peak rf field is thought to be due to the fact that higher peak rf fields lead to more thermal feedback. The value of ΔR_s is expected to increase with power density, thus it is not surprising that ΔR_s increases with field amplitude.

The effect of different heat treatments on ΔR_s is investigated in Figure 4.25, in which the ΔR_s values are plotted as a function of peak rf field for a baseline treatment as well as 120 °C, and a 400 °C bakes for the HWR in the 389 MHz mode. For most peak rf field values, the 120 °C bake results in smaller ΔR_s values compared to the other two treatments.

The data in Figures 4.24 and 4.25 show that ΔR_s is smaller for the lower frequency and 120 °C bake. This is to be expected because lower frequencies and 120 °C bakes are known to reduce the temperature dependent surface resistance. Since ΔR_s increases with power density it is inversely proportional to the quality factor, and thus higher quality factors lead to lower ΔR_s values.

4.4 Magnetic Sensitivity and Normalized R_{mag}

Magnetic sensitivity, S_{mag} is a measure of the sensitivity of the surface resistance of a material to trapped magnetic flux, defined in Section 1.3. S_{mag} is related to another quantity, R_{mag}, which is the additional rf surface resistance on an SRF cavity caused by magnetic vortices that are trapped by pinning centres in the cavity during cool-down. R_{mag} contributes to the residual resistance R_{res} in the equation [69]

$$R_s = R_{BCS} + R_0 + R_{mag}. \tag{4.2}$$

It is important to reduce additional rf losses from the magnetic component to a small fraction of the overall surface resistance. For the experimental results in this thesis, S_{mag} is equal to R_{mag} divided by the applied

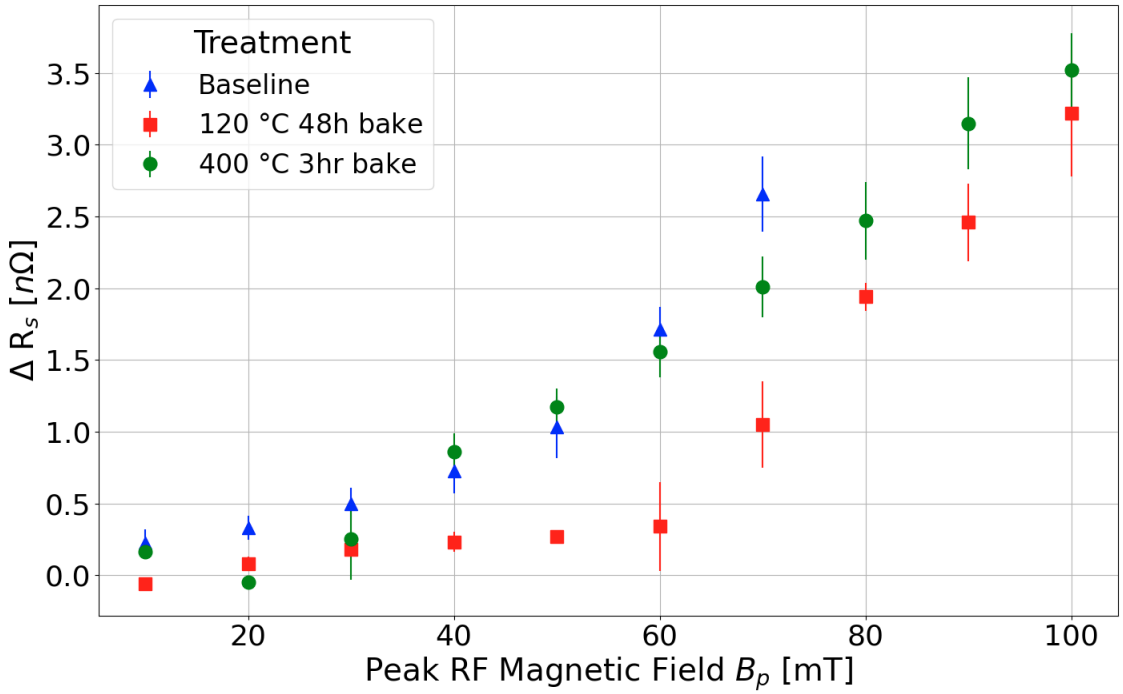

Figure 4.25: ΔR_s values for the HWR in the 389 MHz mode for different treatments. The ΔR_s values tend to increase with peak rf field. For the baseline treatment data is not available for peak rf magnetic fields above 70 mT.

field multiplied by the flux trapping efficiency η_{mag} [26],

$$S_{mag} = \frac{R_{mag}}{\eta_{mag} B_{applied}}. \tag{4.3}$$

S_{mag} does not depend on the applied field. S_{mag} is a material property, whereas R_{mag} depends on not only the material, but also the applied magnetic field and η_{mag}. The flux trapping efficiency is a measure of what percentage of flux is trapped in the cavity during a cool down. In a simplistic analysis it can be assumed that flux is trapped uniformly over the surface of a cavity, in which case the flux trapping efficiency can be described by the equation,

$$\eta_{mag} = 1 - \frac{B_{measured}}{B_{expected}} \tag{4.4}$$

where $B_{measured}$ is the field enhancement observed from the fluxgate probe readings and $B_{expected}$ is the field enhancement expected from the COMSOL simulations. In cases where $B_{expected}$ is zero, η_{mag} is defined as

$$\eta_{mag} = \frac{B_{remaining}}{B_{applied}} \tag{4.5}$$

where $B_{remaining}$ is the flux remaining after the cool-down, and $B_{applied}$ is the applied magnetic field.

For the data analysis performed in this thesis, R_{mag} is extracted by taking the difference in cavity surface resistance when the cavity is cooled with an applied magnetic field (FC) and when it is ZFC,

$$R_{mag} = R_{sFC} - R_{sZFC}. \tag{4.6}$$

For example, to compute R_{mag} for the 40 μT horizontal applied field for the fast cool-down shown in Figure 4.15, one would need to subtract the red field cooled data points from the blue ZFC data points. However,

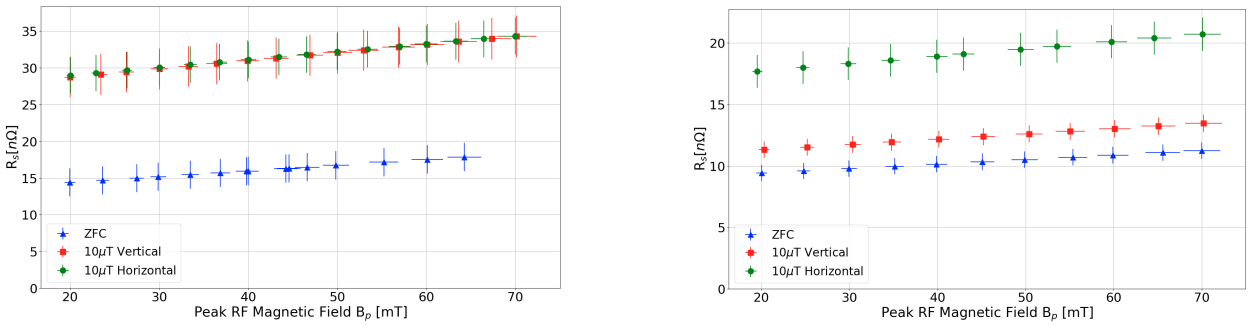

(a) 400 °C bake

(b) 120 °C bake

Figure 4.26: Surface resistance as a function of peak rf field for the HWR in the 389 MHz mode at 2.0 K. The R_{mag} values in Figure 4.27 are the difference in R_s between the ZFC and field cooled data sets in these plots.

this cannot be done directly because these data points do not line up at the same B_p values. Therefore, the data sets are fitted to polynomial functions, and the two polynomial fits are subtracted from each other at specific B_p values. It is important to note that R_{mag} values are not raw data points, but rather the result of subtracting two polynomial fits at specific values. The uncertainties in these fit functions propagate into the total uncertainties of R_{mag}.

Plots of the surface resistance as a function of peak rf field for the HWR after undergoing a 400 °C bake for three hours, and a 120 °C bake for 48 hours with magnetic fields of 10 μT applied in either the horizontal or vertical direction are shown in Figure 4.26. As an example, these R_s values are used to compute the R_{mag} values in Figure 4.27. For all of the HWR data the cool-downs were done at a fast speed. The average cool-down speed for the HWR cool-downs is 1355 mK/min. The B_p range of 20-70 mT is chosen because the polynomial fits of the R_s vs B_p fields are more accurate in this range.

The focus of the data analysis for this Section is on a property called normalized R_{mag}, denoted R_{magN}, and defined as

$$R_{magN} = \frac{R_{mag}}{B_{applied}}. \tag{4.7}$$

In order to fully characterize η_{mag} a full map of localized flux trapped all over the cavity surface would be required. In order to obtain a direct characterization of S_{mag}, the cavities should be cooled down very slowly so that the condition $\eta_{mag} \sim 1$ is satisfied, as was done in experiments by Longuevergne [26]. Computing S_{mag} is not a reliable way to characterize flux trapping in coaxial cavities since flux can be trapped very non-uniformly. The R_{magN} results in this thesis still reveal information about flux trapping as a function of treatment, but the results need to be carefully evaluated while considering both geometry and field direction.

As with the R_{mag} result above, for the R_{magN} values computed in this chapter, the peak rf field range is limited to 20-70 mT because the polynomial fits of the R_s vs B_p fields are more accurate in this range. The normalized R_{mag} values for the HWR and QWR were computed using data that was collected while the cavities were at fixed temperatures of 2.0 and 4.2 K, respectively.

4.4.1 HWR Normalized R_{mag} Analysis

For the following HWR data analysis, the normalized R_{mag} values are computed for vertical and horizontal field cooled data sets after the cavity undergoes two different bakes: a 400 °C three hour bake and a 120 °C 48 hour bake. The dependence of R_{magN} on cavity frequency is also explored for both bakes. For these experiments the HWR was cooled through its superconducting temperature as fast as possible, at a similar speed to the fast cool-downs mentioned in previous sections.

Normalized R_{mag} as a function of peak rf field for the HWR with a vertical or horizontal applied field after undergoing a 400 °C three hour bake and a 120 °C 48 hour bake is plotted in Figure 4.28. Note that

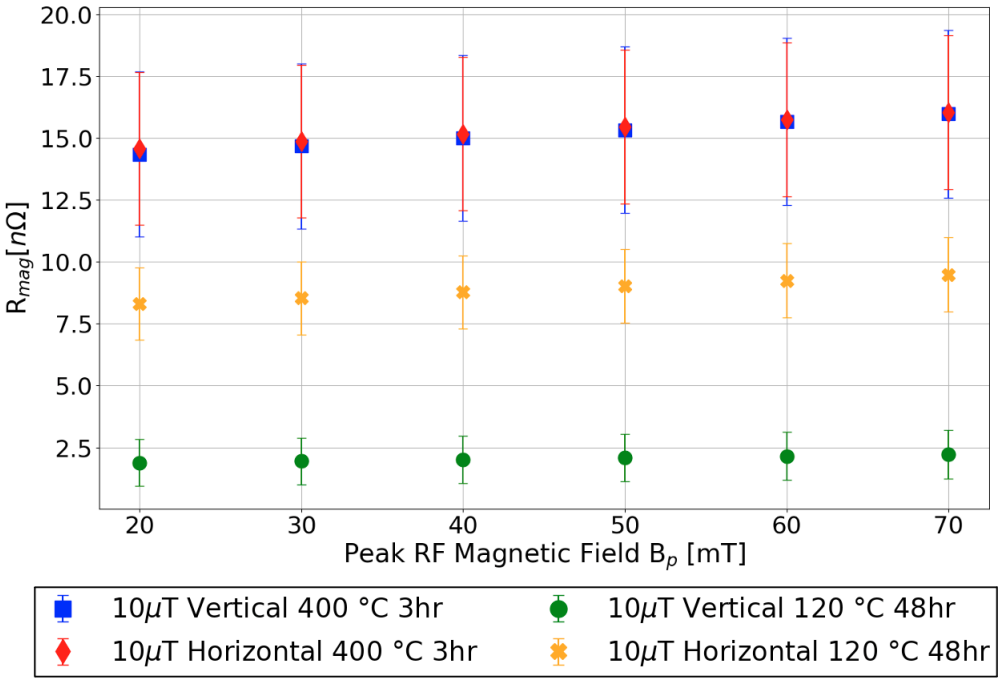

Figure 4.27: R_{mag} as a function of peak rf field for the HWR at 2.0 K in the 389 MHz mode. R_{mag} shows little field dependence.

this plot contains the same data as in Figure 4.27 with R_{mag} converted to R_{magN}. For the 400 °C bake the R_{magN} values for the vertically and horizontally field cooled data sets are nearly identical, whereas for the 120 °C bake the horizontal applied field gives rise to higher normalized R_{mag} than the vertical. Overall the HWR has a lower R_{magN} after a 120 °C bake in this mode for either field orientation. It was found that for all the HWR R_{magN} datasets in this thesis, R_{magN} depends more on cavity frequency than on peak rf field. Therefore, in subsequent R_{magN} plots the average normalized R_{mag} is plotted for the peak rf field range of 20-70 μT, and field dependence is not shown.

The use of higher order modes (HOMs) in the HWR makes it possible to resolve R_{magN} as a function of frequency without changing cavities or cool-down dynamics which may influence flux trapping. The normalized R_{mag} values as a function of frequency for the HWR with a vertical and horizontal applied magnetic field are shown in Figures 4.29 and 4.30, respectively. Note that the 389 MHz data points in Figures 4.29 and 4.30 contain averages of the R_{magN} values plotted in Figure 4.28 so that they may be compared with other frequencies. Both field orientations have a reduced R_{magN} after the 120 °C bake compared to the 400 °C bake. R_{magN} generally increases with frequency.

The results described in the previous paragraph can be compared with Checchin's results [24] shown in Figure 1.13 where he found that magnetic sensitivity, which is closely related to normalized R_{mag}, generally increases with frequency. It is worth noting that the magnetic sensitivity in Checchin's results is defined as the additional surface resistance introduced per amount of trapped magnetic field, with the trapped magnetic field measured at the cavities' equator. The magnetic sensitivity results presented by Checchin cannot be directly compared to the R_{magN} results of this section since these are different values.

The COMSOL simulations for the vertical field cooled case indicate that there is more magnetic flux at the top and bottom of the cavity as the flux lines are bent around the cavities' edges as shown in Figures 3.3 and 3.7. The data for the vertical field cooled HWR in Figure 4.29 shows that normalized R_{mag} increases with frequency. This pattern does not suggest any particular location for flux trapping. In Figure 4.29 square-root and linear fit functions are superimposed on the R_{magN} versus peak field vertical field cooled data. A square-root dependence would be expected from Padamsee's simple model [8] in which magnetic

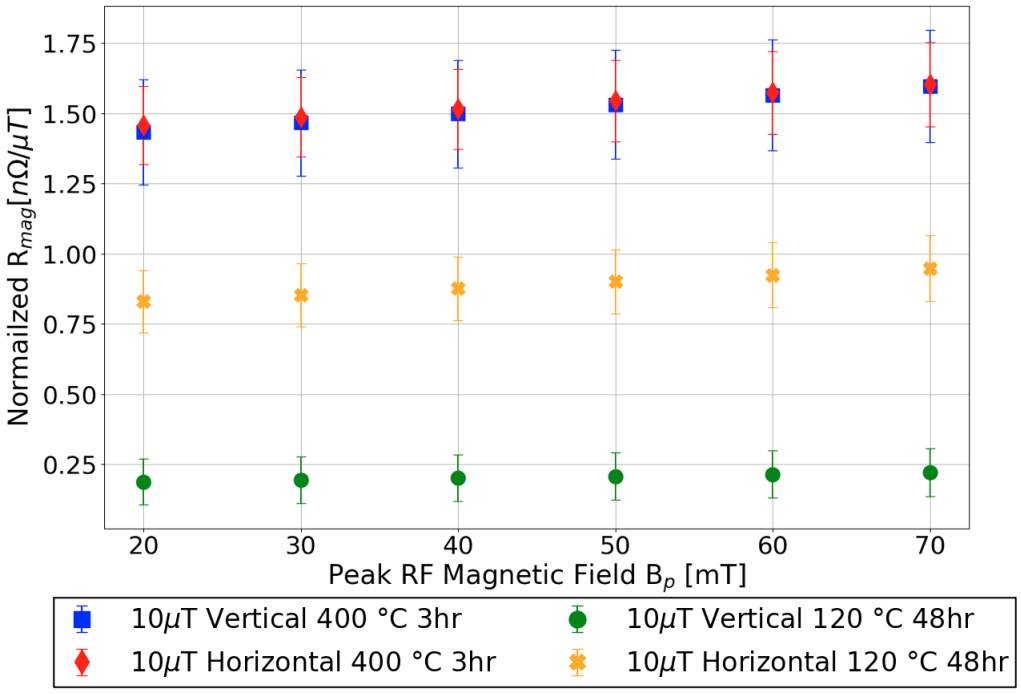

Figure 4.28: R_{magN} as a function of peak rf field for the HWR in the 389 MHz mode. The normalized R_{mag} values are higher after the 400 °C bake. There is a larger difference between the R_{magN} values of the vertically and horizontally field cooled data sets for the 120 °C bake compared to the 400 °C bake. There is little dependence on peak rf field.

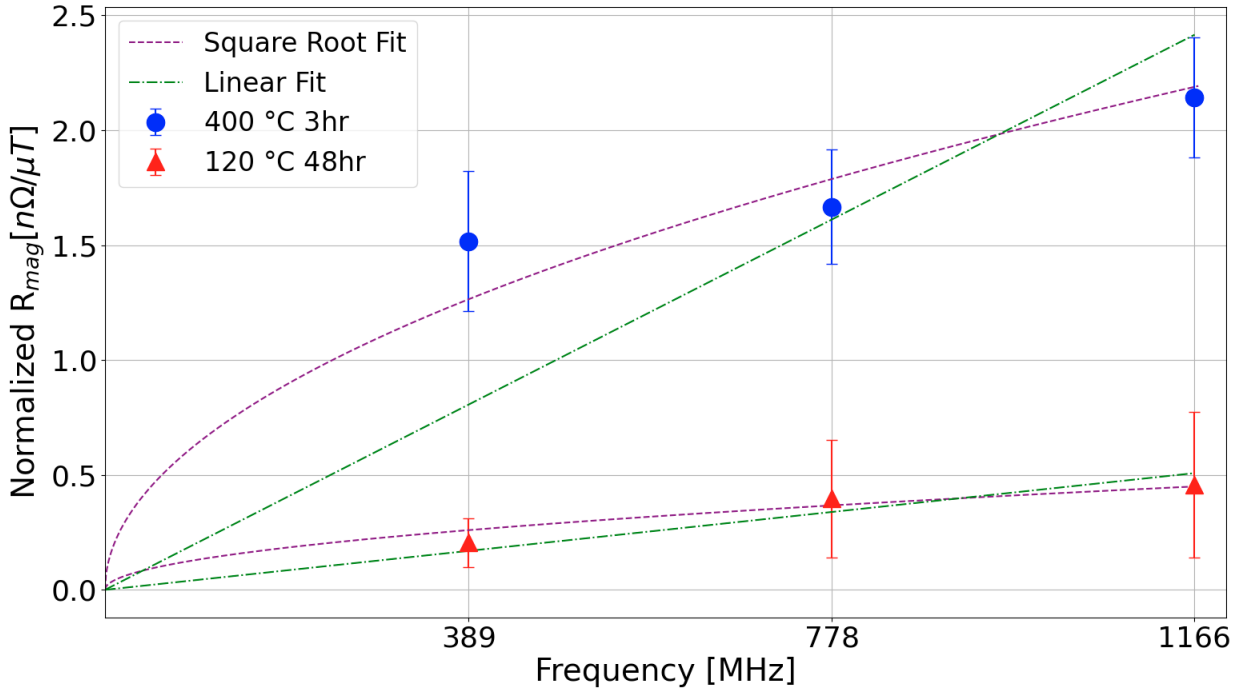

Figure 4.29: Normalized R_{mag} for the vertical field cooled HWR in different resonant modes after different heat treatments. Linear and square-root fit functions were fitted to both data sets. The square-root fits are more accurate than the linear fits.

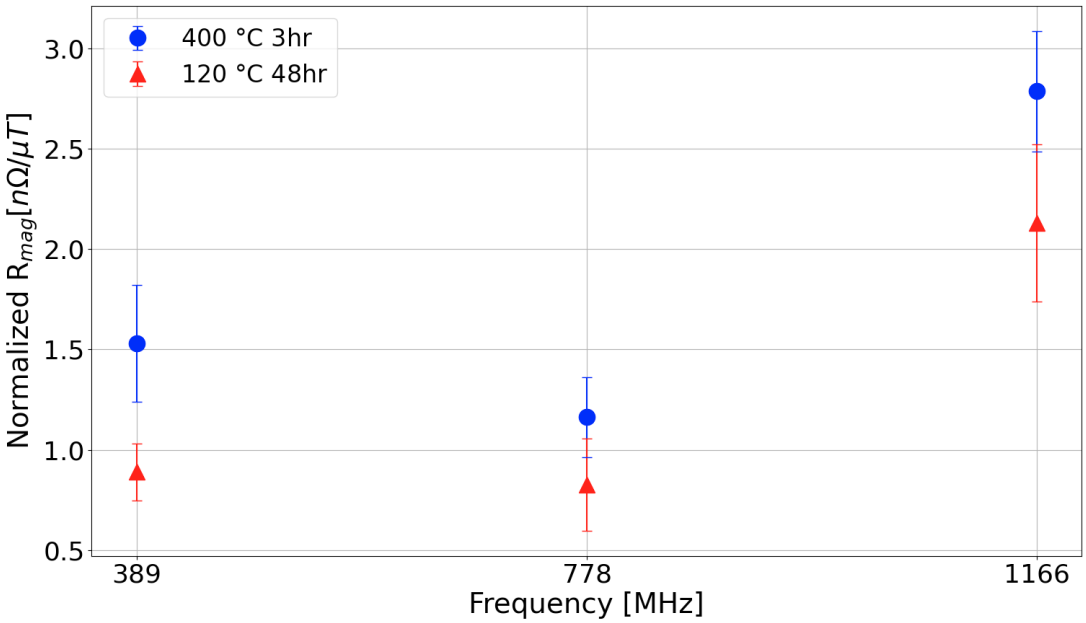

Figure 4.30: Normalized R_{mag} for the horizontal field cooled HWR in different resonant modes after different heat treatments. As with the vertical field cooled case, the 120 °C bake leads to lower normalized R_{mag} than the 400 °C bake. For this field orientation, the middle resonant frequency, 778 MHz shows a drop in normalized R_{mag} compared to the other two frequencies.

Bake temperature	400 °C	120 °C
Square-root fit R-squared value	0.97	0.97
Linear fit R-squared value	0.80	0.95

Table 4.3: Summary of R-squared values for the fit functions in Figure 4.29.

sensitivity is proportional to the normal state resistance which varies as the square-root of cavity frequency. The linear fits were done to determine if a linear dependence describes the R_{magN} data better than the expected square-root dependence. The R-squared values of these fits are summarized in Table 4.3. For each data set the square-root fits have larger R-squared values than the linear fits. This means that the relationship between normalized R_{mag} and frequency is closer to a square-root dependence than linear dependence.

Fits were not done for the horizontal field cooled data since the middle frequency showed a decrease in normalized R_{mag}. In the horizontal field cooled case the 778 MHz mode has a lower normalized R_{mag} than the 389 and 1166 MHz modes. Of the three measured frequencies, a unique feature of the 778 MHz mode is that it has a high rf magnetic field in the center of the cavity, as illustrated in Figure 2.3. These observations indicate that magnetic flux is trapped non-uniformly, and is most likely not trapped in the center of the HWR. A speculative interpretation is that flux is trapped about one third or two thirds of the way up the cavity where the 389 and 1166 MHz modes have higher rf magnetic fields since these modes have higher R_{magN} values.

Assuming uniform flux trapping, η_{mag} has been calculated and summarized in Table 4.4. These values should be interpreted with caution since the magnetic field used to compute η_{mag} is only measured in one location, and there may be non-uniform flux trapping on other parts of the cavity. For this reason, η_{mag} and therefore S_{mag} are not very useful and η_{mag} is not used in the calculations of R_{magN}. The results in Table 4.4 will illustrate some issues with η_{mag}. The η_{mag} values are generally higher for the vertical field orientation compared to the horizontal. There is a larger difference in the η_{mag} values for the two field orientations after the 120 °C bake compared to the 400 °C bake.

Treatment	Vertical	Horizontal
400 °C bake	0.71	0.55
120 °C bake	1.24	0.67

Table 4.4: Measured η_{mag} values for the HWR.

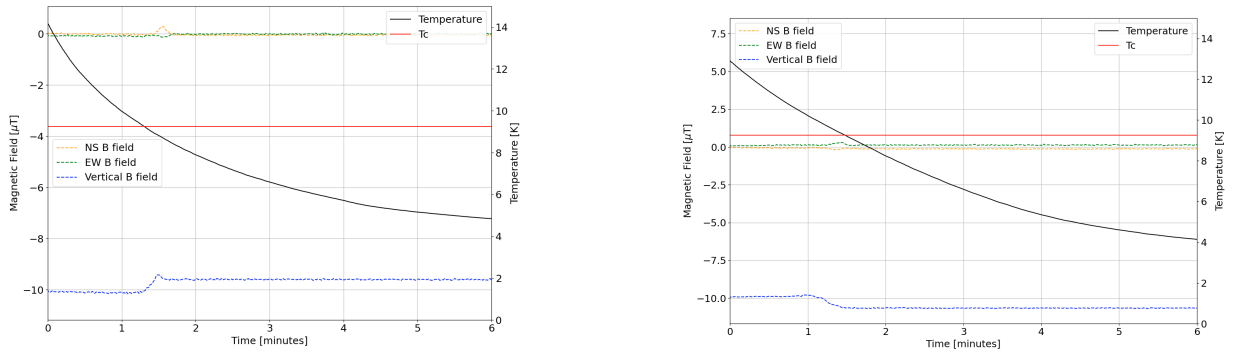

(a) 120 °C Bake

(b) 400 °C Bake

Figure 4.31: Fluxgate probe and temperature sensor readings for the HWR with a vertical applied field after two different bakes. For the 120 °C bake shown on the left the vertical field sees a small reduction after the superconducting transition. For the 400 °C bake plotted on the right, a small field enhancement is measured. Both heat treatments yield significant amounts of flux trapping and are different from the COMSOL simulation.

An interesting result shown in Table 4.4 is that after a 120 °C bake, a vertical applied field results in an η_{mag} value greater than one, namely 1.24. This is because from the COMSOL simulations a field enhancement of about 20 % is expected in the inner conductor, while in reality a field reduction is observed as shown on the left of Figure 4.31. This is an indication that the definition of η_{mag} does not work for coaxial cavities, as η_{mag} should never be greater than one. A limitation of these flux trapping measurements is that they only apply to one specific location in the cavity where the fluxgate probes are situated. However, it is likely that flux is trapped non-uniformly and may be located somewhere else that is not measured.

This phenomenon is not observed for the 400 °C bake, as the vertical field sees a small field enhancement shown on the right of Figure 4.31, and the η_{mag} value is less than one. A possible explanation for this is that after the 120 °C bake the cavity has less pinning centers, making it easier to move flux away from the cavity.

The magnetic field measurements shown in Figure 4.31 are compared with the COMSOL simulation in Figure 4.32. The COMSOL result in Figure 4.32 was already presented in Figure 3.9 and is re-plotted here so that it may be easily compared with the experimental results. The COMSOL simulation shows a larger dip in magnetic field and final field enhancement. When compared to the COMSOL simulation the two data sets indicate strong flux trapping but with different trapping evolutions. This may be because some fraction of the flux is being pushed around the HWR rather than through the inner conductor. There are signs that flux is trapped both in the outer and inner conductor.

A comparison of the COMSOL simulation and fluxgate probe measurements is also done for a horizontally applied magnetic field in Figure 4.33. As with the vertical cool-down, the COMSOL result was previously shown in Figure 3.11 and is repeated here for a direct comparison with real cool-down data. Both the experimental results and COMSOL simulation show a reduction in the magnetic field after the superconducting transition. The COMSOL simulation models complete flux expulsion in which the magnetic field in the inner conductor is reduced to zero. For the 400 and 120 °C bakes, about 5.5 and 7, μT of magnetic flux remains in the inner conductor, respectively, as there is incomplete flux expulsion.

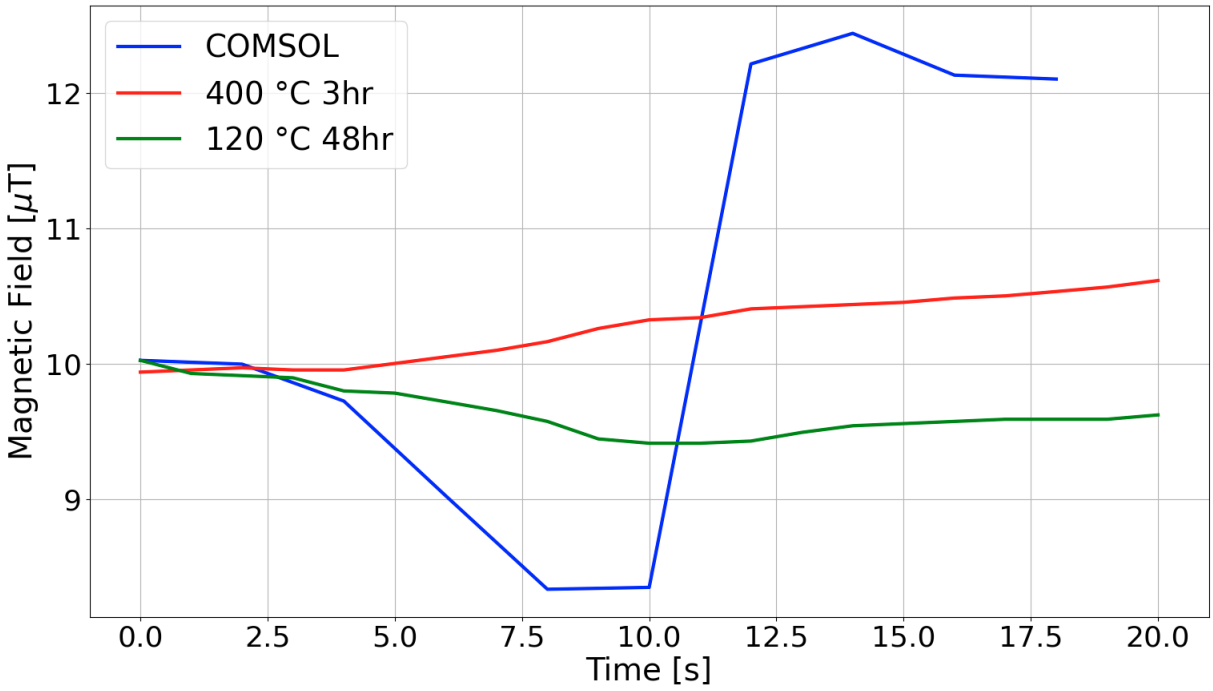

Figure 4.32: Comparison of magnetic fields during the superconducting transition with a vertically applied field for the COMSOL simulation, 400, and 120 °C bakes of the HWR. Both bakes result in strong flux trapping with different cool-down evolutions compared to the COMSOL simulation.

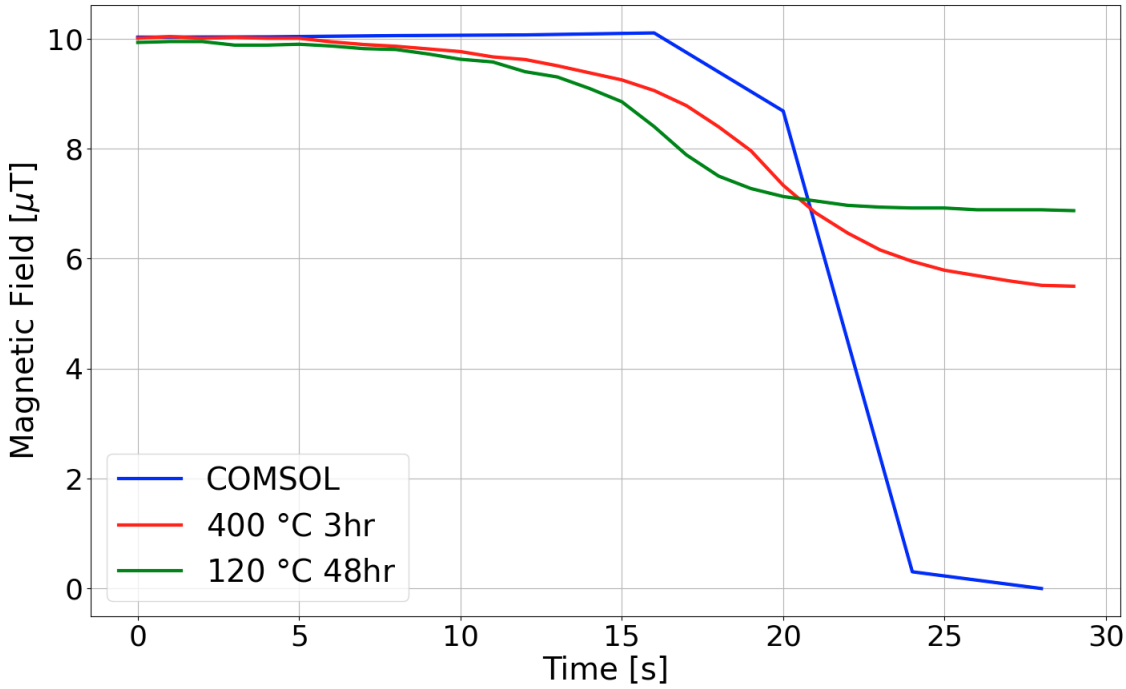

Figure 4.33: Comparison of magnetic fields during the superconducting transition with a horizontally applied field for the COMSOL simulation, 400, and 120 °C bakes of the HWR. The COMSOL simulation shows complete flux expulsion, while the experimental results show some remaining magnetic flux in the inner conductor after the cool-down.

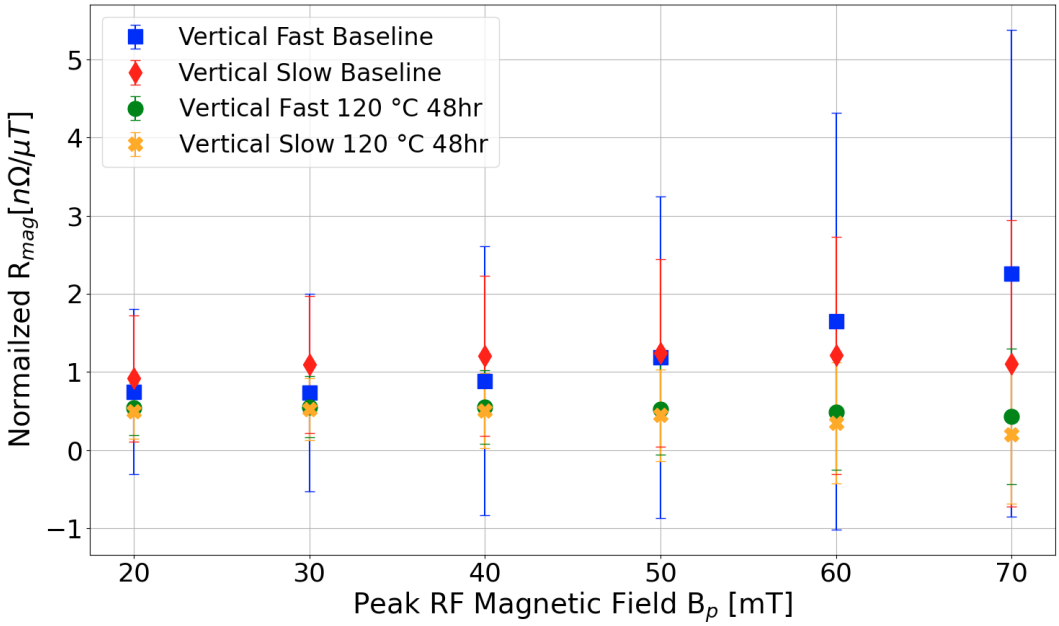

Figure 4.34: R_{magN} as a function of peak rf field for fast and slow cool-downs of the QWR in the 644 MHz mode. The R_{magN} values were computed using the field corrected R_s values. The dataset for the baseline treatment and fast vertical cool-down shows an increase in R_{magN} with peak rf field. The error bars are large compared to the R_{magN} values.

In summary, for the HWR, R_{magN} usually tends to increase with cavity frequency. This frequency dependence is in agreement with the results reported by Checchin [24] shown in Figure 1.13. For the vertical field cooled data R_{magN} agrees with Padamsee's square-root dependence model as a square-root dependence describes the data just as well or better than a linear dependence. For the horizontal field cooled case the R_{magN} data does not strictly increase with frequency. The deviation from Padamsee's square-root model in the horizontal field cooled case can be explained by incomplete flux trapping.

4.4.2 QWR Normalized R_{mag} Analysis

For the QWR the two cavity treatments to be compared are the baseline treatment and a 120 °C 48 hour bake. The normalized R_{mag} values for fast and slow cool-downs with vertical and horizontal applied magnetic fields are examined. The frequency dependence of some of these R_{magN} results is also studied.

These R_{magN} values in this subsection were computed using the non field corrected R_s^* values, which are equal to the geometry factor divided by the quality factor, G/Q. When R_{magN} is computed using R_s, the error bars are larger since the uncertainties in the polynomial fits used to convert R_s^* to R_s propagate to the final result. This can be seen by comparing Figures 4.34 and 4.35 which show R_{magN} as a function of peak rf field for the baseline and 120 °C bake treatments for vertical field cooled data sets. The difference in these figures is that the R_{magN} values in Figure 4.34 were computed using R_s while the R_{magN} values in Figure 4.35 were computed using R_s^*. In addition to having large uncertainties, the field corrected R_{magN} data for the fast vertical field cooled baseline treatment dataset in Figure 4.34 shows an increase in R_{magN} with peak rf field. Without computing R_{magN} using R_s^*, it would be unclear as to whether this field dependence is a real measured effect or the result of data processing. Another justification for using R_s^* instead of R_s is that the absolute field dependence is not required to compare surface resistances for different data sets, as a relative value will suffice.

In Figure 4.35, the error bars represent the uncertainties associated with the standing wave ratio described in Section 2.5.3 and the error propagated from taking the difference of two R_s^* curves. In the case of the baseline treatment and fast cool-down, R_{magN} shows a small increase with peak rf field. For all other cool-

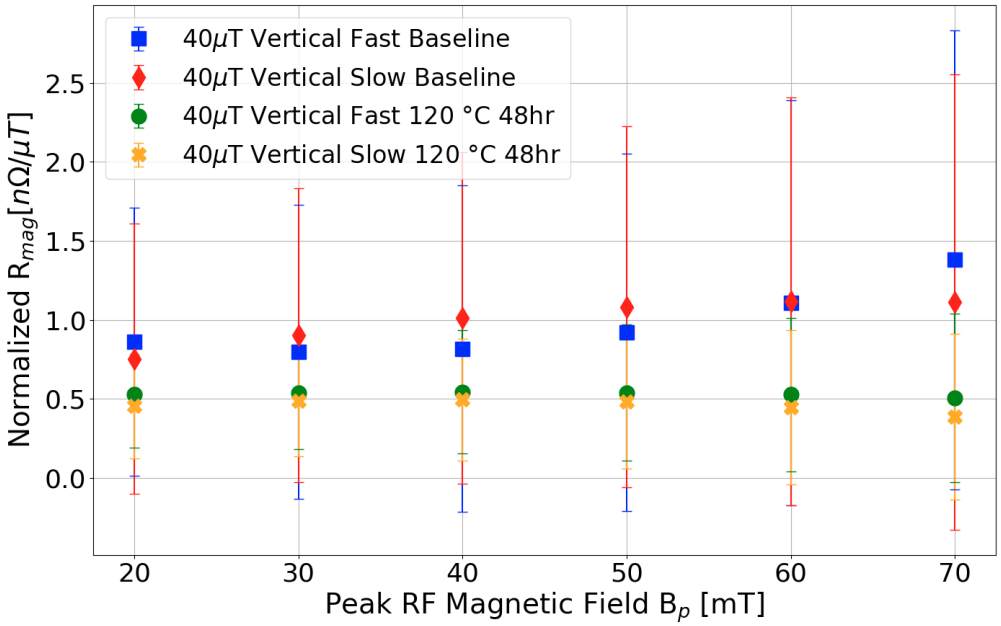

Figure 4.35: R_{magN} as a function of peak rf field for fast and slow cool-downs of the QWR in the 644 MHz mode. The R_{magN} values were computed using the non field corrected R_s^* values. R_{magN} does not show a significant dependence on peak rf field within the error bars.

downs in Figure 4.35, R_{magN} shows almost no dependence on peak rf field. R_{magN} is lower for the 120 °C bake compared to the baseline treatment.

The horizontal field cooled case is shown in Figure 4.36. In the scenario of the baseline treatment and fast cool-down, there is a slight rise in R_{magN} with the peak rf field. However, in all other cool-downs depicted in Figure 4.36, R_{magN} demonstrates no dependence on the peak rf field. The strong field dependence for the fast cool-down baseline treatment with a horizontal applied field in Figure 4.36 is a striking result of the cavity measurements. RF field amplitude dependence of magnetic sensitivity has been previously observed by Calatroni [70]. Calatroni observed that magnetic sensitivity can have a linear dependence on rf field amplitude, and this dependence tends to be stronger for high frequency cavities and higher rf fields. However, in this case a possible explanation is that more flux is trapped in the tip of the inner conductor where the rf fields are lower. Thus, as B_p increases, more power is absorbed in the tip of the inner conductor, leading to a localized increase in surface resistance in the inner conductor. In this case it is thought that the field dependence mostly comes from non-uniform flux trapping in the QWR geometry.

One way of quantifying the field dependence of a cavity is by calculating the γ coefficient, which is described in Section 4.3. The coefficient is a parameter that measures rf field dependence on B_p^2. A larger γ coefficient indicates a larger dependence on peak rf field. The γ coefficients for the R_s vs B_p curves of the baseline treated QWR for a fast and slow horizontal cool-down are 2.1 and 1.6, respectively. Note that these γ coefficients were computed using the field corrected R_s values rather than the non-field corrected value G/Q in order to get an accurate measurement of the rf field dependence. These γ coefficients provide further confirmation that the fast horizontal cool-down does indeed have a larger peak rf field dependence than the slow cool-down.

Normalized R_{mag} values for the different resonant modes of the QWR are compared in Figure 4.37 for the fast and slow cool-downs with vertical applied fields and a 120 °C bake heat treatment. The 644 MHz values in Figure 4.37 are the average of the 120 °C bake data points shown in Figure 4.35. For the same frequencies, R_{magN} values are similar for the fast and slow cool-downs which is consistent with the similar levels of trapped flux seen for both cool-down speeds in Figure 4.17.

The 644 MHz mode has overall higher R_{magN} than the 217 MHz mode. A possible explanation for these

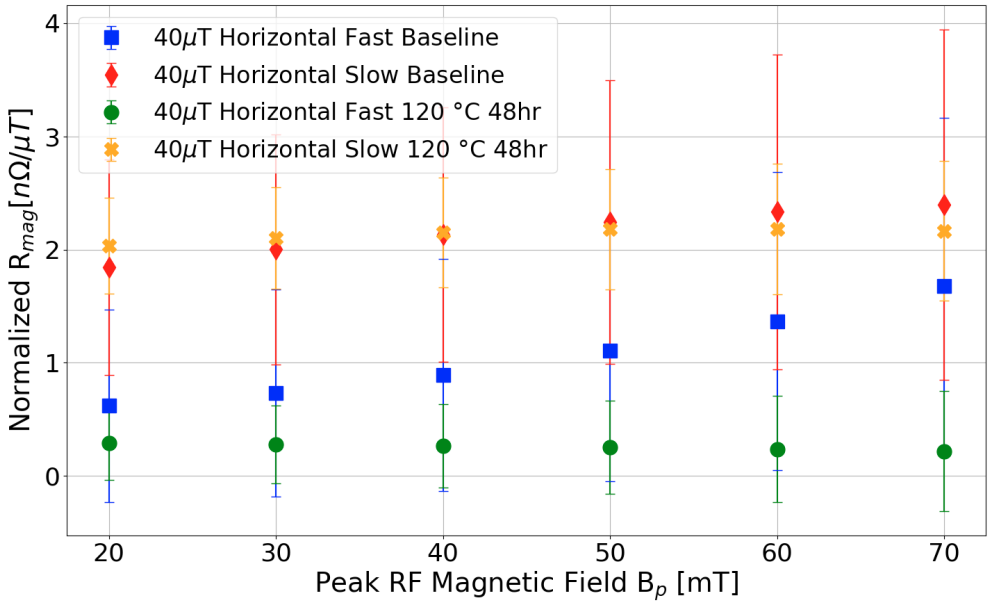

Figure 4.36: R_{magN} as a function of peak rf field for fast and slow cool-downs of the QWR in the 644 MHz mode. The R_{magN} values were computed using the non field corrected R_s^* values. The fast cool-down after a baseline treatment shows some increase in normalized R_{mag} with peak rf field.

results is that magnetic flux is trapped along the length of the inner conductor, with a larger concentration of flux trapped near the tip. The rf magnetic field distributions for both measured resonant modes are illustrated in Figure 4.16. The lower parts of the inner conductor have higher rf magnetic field for the 644 MHz mode compared to the 217 MHz mode. Parts of the cavity with higher rf magnetic fields are more sensitive to trapped magnetic flux since more power is dissipated into regions with higher rf fields. Fits were not done for the QWR since each data set only contains two data points. This comparison is not available for the baseline treatment because there is no data available for the 217 MHz mode due to an amplifier malfunction.

A comparison of the two QWR resonant modes is done for the horizontally applied field for the fast and slow cool-down data sets after a 120 °C bake in Figure 4.38. The average values for the 644 MHz measurements in Figure 4.38 are derived from the data points of the 120 °C bake shown in Figure 4.36. For both frequencies the fast cool-down has significantly lower normalized R_{mag} values than the slow cool-down, which is the opposite of what was found for the vertical field cooled case due to the significant increase in flux trapping seen in the slow cool-down of Figure 4.13. For both cool-down speeds, the 644 MHz mode has a higher R_{magN} than the 217 MHz mode. The observed frequency dependence suggest that the slow cool-down may result in flux being trapped near the lower end of the inner conductor, particularly with the slow cool-down.

In Section 4.4.1 it was observed that for the HWR a 120 °C bake leads to lower normalized R_{mag} values than a 400 °C bake. Likewise, it was noted earlier in this section that for the QWR a 120 °C bake leads to lower R_{magN} values than the baseline treatment. This is consistent with previous results reported by Checchin et al [24] and Martinello et al [25] who found that 120 °C baked cavities have lower mean free paths and magnetic sensitivities compared to other treatments. This is also consistent with the findings reported by Ito et al [48] who found that 120 °C baked cavities have lower magnetic sensitivities compared to 400 °C baked cavities.

The following bullet points summarize the findings on the external normalized R_{mag}:

- For the HWR the normalized R_{mag} has little dependence on peak rf field.
- For the HWR the normalized R_{mag} values for the vertical field cooled data sets have an approximately square root dependency on the rf frequency.

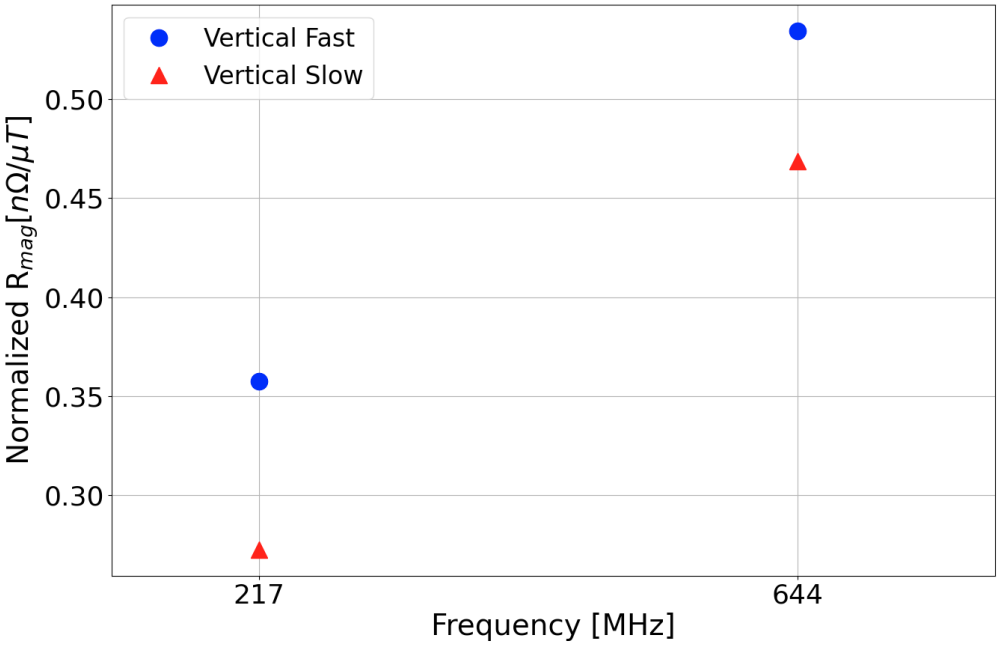

Figure 4.37: R_{magN} for the QWR for different resonating modes and cool-down speeds after undergoing a 120 °C bake. The 644 MHz mode has higher normalized R_{mag} values than the 217 MHz mode, and the fast cool-down results in higher normalized R_{mag} values compared to the slow cool-down. Error bars are omitted for clarity.

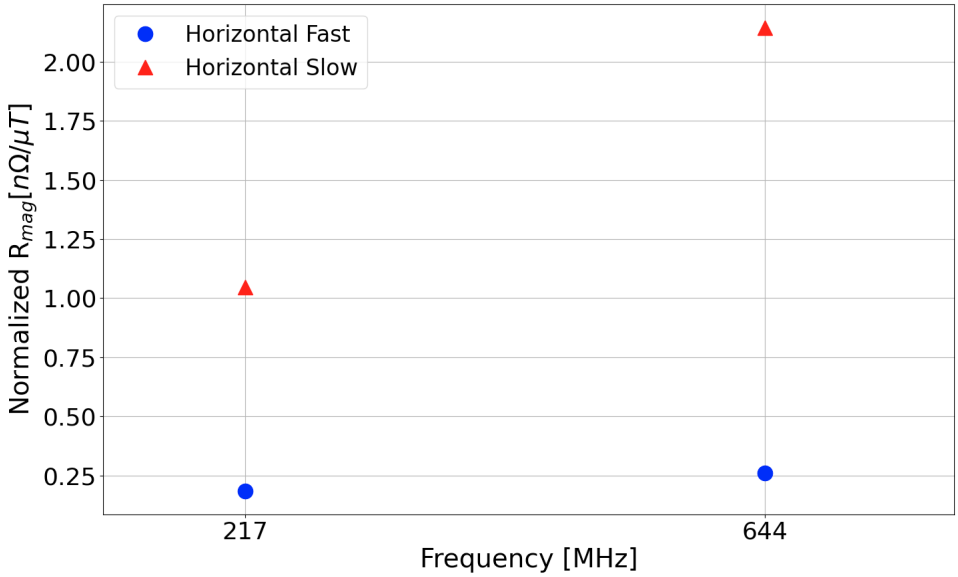

Figure 4.38: R_{magN} for the QWR after undergoing a 120 °C bake. For the fast cool-downs the 644 MHz mode has higher normalized R_{mag} compared to the 217 MHz mode at the same cool-down speed.

- For the HWR horizontal field cooled data sets a clear frequency dependence on R_{magN} could not be determined due to suspected non-uniform flux trapping.
- The QWR shows an increase in normalized R_{mag} with peak rf field for the case of a fast cool-down with a vertical applied magnetic field after the baseline treatment.
- The 120 ℃ bake decreases the normalized R_{mag} for both cavities compared to a baseline treatment or a 400 ℃ bake.
- Both cavities are more sensitive to horizontal fields than vertical fields.
- For horizontal applied fields in the QWR a fast cool-down can improve flux expulsion and cavity performance since the fast cool-down is better able to overcome flux pinning.
- The QWR has higher normalized R_{mag} in the first higher order mode compared to the fundamental mode due to flux being trapped in a region of the inner conductor in which the first higher order mode has a larger rf magnetic field.
- Flux can be trapped non-uniformly in coaxial cavities.
- R_{magN} is a better parameter for characterizing flux expulsion in coaxial cavities than S_{mag} because coaxial cavities can have incomplete flux trapping, and flux is likely trapped non-uniformly.
- The normalized R_{mag} results for the HWR were different than those for the QWR, indicating that flux trapping is geometry dependent. This is in agreement with Longuevergne's findings [26].

Chapter 5

Conclusions

The goal of these studies is to study flux trapping in coaxial cavities. It is known that SRF cavities are sensitive to external magnetic fields. Their performance is measured using the quality factor Q_0, which decreases if external magnetic fields are present during the cavities' superconducting transition. The experiments described in this thesis investigate how external magnetic fields, temperature gradients, cavity processing, and cool-down speeds influence cavity surface resistance when a cavity is cooled down to superconducting temperatures.

Most research on SRF cavities has been done on 1.3 GHz single cell elliptical cavities. There remains an open question of how geometry affects the expulsion of magnetic fields in SRF cavities. To explore this question, several experiments were conducted using a HWR and QWR style cavity. Several measurements were done with external fields applied in different directions relative to the cavities' axis. These studies also explore how different heat treatments affect the cavities' sensitivity to external magnetic fields as well as the amount of flux trapped in the cavities. An important lesson learned from this thesis is that flux trapping in coaxial cavities is rather complicated due to their highly non-uniform rf magnetic field distributions, flux trapping, and cool-down dynamics.

A result of the work in this thesis is that the geometry of the cavities is of great importance, as the results of the HWR are much different than those of the QWR. Another important finding is that flux is trapped non-uniformly. Non-uniform flux trapping is particularly influential in coaxial cavities due to their non-uniform rf magnetic field distribution. This is evident from the fact that there is a frequency dependence of R_{mag} that deviates from what would be expected based on the literature. Further evidence of non-uniform flux trapping is that the COMSOL simulations showed different patterns of flux expulsion than the experimental results.

One novel finding arose from cooling the QWR down past its superconducting temperature at different cool-down rates. This was done with external magnetic fields applied in the vertical or horizontal direction relative to the axis of the QWR to see which combination of field direction and temperature gradient would yield the most efficient flux expulsion. It was found that cooling the QWR down with a high temperature gradient with a horizontal applied magnetic field resulted in the most significant flux expulsion compared to the other cavity tests by a large margin (see Figure 4.12). The significant flux expulsion for a fast cool-down can be explained by large thermal gradients that are better able to overcome flux pinning compared to smaller thermal gradients. In the experiments performed in this thesis fast cool-downs had much larger thermal gradients compared to slow cool-downs.

When the QWR is cooled with a vertical applied field, the change in magnetic field observed during the cool-downs is small compared to the applied field for both fast and slow cool-downs after the baseline treatment and 120 ℃ bake. For a vertical applied magnetic field magnetic flux is unable to escape the inner conductor regardless of cool-down speed. For the QWR the applied magnetic field direction and temperature gradient greatly affect the amount of flux trapped in the cavity.

A study was done to analyze how different heat treatments affect the normalized R_{mag} values of the HWR. The normalized R_{mag}, R_{magN}, was computed for the HWR after it underwent a 120 or 400 ℃ bake.

It was found that the HWR had consistently lower R_{magN} values after the 120 ℃ bake as compared to the 400 ℃ bake, indicating that cavity processing affects the cavities' sensitivity to trapped flux. When the HWR was cooled with a vertical applied field, the normalized R_{mag} increased with frequency, suggesting that flux was trapped near the top or bottom of the cavity as flux is bent around the edges of the cavity as in the COMSOL simulations. For the horizontal applied field, the 778 MHz mode had lower R_{magN} values than the 389 and 1166 MHz modes. This led to speculation that for the horizontal field cooled case flux may be trapped one or two thirds of the way up the cavity where the rf magnetic field of the 778 MHz mode is at a minimum. For these experiments, identifying the locations of trapped flux in coaxial cavities is not straightforward as flux is trapped non-uniformly. To get an accurate picture of flux trapping, localized trapping must be considered. Multiple sensors measuring flux expulsion across the cavity surface would help identify flux trapping locations.

For the R_{magN} study done on the QWR it was found that with a horizontal applied magnetic field, R_{magN} was reduced when the cavity was cooled down with a higher temperature gradient as compared to a lower temperature gradient. This is consistent with the flux expulsion measurements. Different temperature gradients can affect both the amount of trapped flux in the cavity and the way in which the cavity reacts to the trapped flux.

When the HWR was cooled down with a vertical applied field after a 120 ℃ bake a reduction of the magnetic field in the center of the inner conductor was observed, which is the opposite of what is expected from simulations. This lead to an η_{mag} value of more than one. It has been shown that flux is trapped non-uniformly in coaxial cavities, and therefore the flux expulsion efficiency parameter η_{mag} is not useful. Flux may be trapped in parts of the cavity that were not measured, as the fluxgate probes were only in one location for the HWR cool-downs.

For future experiments it would be beneficial to measure the magnetic fields at more locations on the cavity during cool-downs to gain a better understanding of where flux is being trapped in coaxial cavities.

Bibliography

[1] ATLAS Collaboration. Observation of a new particle in the search for the standard model higgs boson with the ATLAS detector at the LHC. *Physics Letters B*, 716(1):1–29, Sep 2012. doi:10.1016/j.physletb.2012.08.020.

[2] R. Mohan and D. Grosshans. Proton therapy – present and future. *Advanced Drug Delivery Reviews*, 109:26–44, 2017. ISSN 0169-409X. doi:10.1016/j.addr.2016.11.006.

[3] D. S. Pudjorahardjo and P. I. Wahyono. High power particle accelerator for driving the nuclear waste transmutation system at nuclear power plant. *Journal of Physics: Conference Series*, 1825(1):012093, Feb 2021. doi:10.1088/1742-6596/1825/1/012093.

[4] D. A. Edwards and M. J. Syphers. *An introduction to the physics of high energy particle accelerators*. Wiley-VCH Verlag GmbH & Co., 2004. ISBN 9780471551638.

[5] J. D. Jackson. *Classical electrodynamics*. Wiley & Sons, Inc, 1962. ISBN 0471431311. First Edition.

[6] M. Conte and W. M. Mackay. *An introduction to the physics of particle accelerators*. World Scientific Publishing Co., 2008. ISBN 9789812779618. Second Edidtion.

[7] M. Martinello. *The path to high Q-factors in superconducting accelerating cavities: Flux expulsion and surface resistance optimization*. PhD thesis, Chicago, Il, 2016.

[8] H. Padamsee, J. Knobloch, and T. Hays. *RF superconductivity for accelerators*. Wiley-VCH, 2008. ISBN 9783527408429.

[9] T. P. Wangler. *RF linear accelerators*. Wiley-VCH, 2008. ISBN 9783527406807. Second Edidtion.

[10] J. K. Sekutowicz and DESY. Superconducting elliptical cavities. CERN Accelerator School, Ebeltoft (Denmark), 8 Jun 2010 - 17 Jun 2010, CERN, Jun 2010. doi:10.48550/ARXIV.1201.2598.

[11] A. Roy, A. S. Dhavle, J. Mondal, K. C. Mittal, and Accelerator & Pulse Power Division. RF design of a single cell superconducting elliptical cavity with input coupler. Bhabha Atomic Research Centre, 12th Workshop on RF Superconductivity at Cornell University, U.S.A., 2005. URL `https://www.classe.cornell.edu/public/SRF2005/pdfs/TuP16.pdf`.

[12] R. Laxdal and Z. Yao. Coaxial resonators for fundamental study. TESLA Technology Collaboration Meeting, June 2018.

[13] T. Moreno. *Microwave tranmission desing data*. Dover Publications Inc., 1948. ISBN 9780890063460.

[14] S. V. Kutsaev, S. Belomestnykh, I. Ben-Zvi, Z. A. Conway, M. P. Kelly, B. Mustapha, P. N. Ostroumov, Q. Wu, B. Xiao, and W. Xu. Design of a superconducting quarter-wave resonator for eRHIC. 27th International Linear Accelerator Conference, Argonne National Laboratory, Argonne, IL 60439, U.S.A., Stony Brook University, Stony Brook, NY 11794, U.S.A., Brookhaven National Laboratory, Upton, NY 11973-5000, U.S.A., 2014. doi:10.1109/TNS.1985.4334439.

[15] A. Gurevich. Theory of RF superconductivity for resonant cavities. *Superconductor Science and Technology*, 30(3):034004, Jan 2017. doi:10.1088/1361-6668/30/3/034004.

[16] N. Haleeda, M. Awang Kechik, and R. Abd-Shukor. Pjsrr (2016) 2(1): Effect of Yb2o3 nanoparticle addition on superconducting properties of BSCCO (2223)/Ag tapes by acetate precipitation method. *Pertanika Journal of Science and Technology*, 2, 01 2016. doi:10.1016/j.physc.2006.08.004.

[17] H. Podlech. Superconducting versus normal conducting cavities. page 20 p, Mar 2013. doi:10.5170/CERN-2013-001.151. Comments: 20 pages, contribution to the CAS - CERN Accelerator School: Course on High Power Hadron Machines; 24 May - 2 Jun 2011, Bilbao, Spain.

[18] A. Romanenko, A. Grassellino, O. Melnychuk, and D. A. Sergatskov. Dependence of the residual surface resistance of superconducting radio frequency cavities on the cooling dynamics around Tc. *Journal of Applied Physics*, 115(18):184903, 2014. doi:10.1063/1.4875655.

[19] A. Romanenko, A. Grassellino, A. C. Crawford, D. A. Sergatskov, and O. Melnychuk. Ultra-high quality factors in superconducting niobium cavities in ambient magnetic fields up to 190 mg. *Applied Physics Letters*, 105(23):234103, 2014. doi:10.1063/1.4903808.

[20] M. Checchin. *Physics of limiting phenomena in superconducting microwave resonators: Vortex dissipation, ultimate quench and quality factor degradation mechanisms*. PhD thesis, Graduate College of the Illinois Institute of Technology, Chigago, Illinois, 2016.

[21] S. Posen, M. Checchin, A. C. Crawford, A. Grassellino, M. Martinello, O. S. Melnychuk, A. Romanenko, D. A. Sergatskov, and Y. Trenikhina. Efficient expulsion of magnetic flux in superconducting radiofrequency cavities for high Q0 applications. *Journal of Applied Physics*, 119(21):213903, 2016. doi:10.1063/1.4953087.

[22] S. Posen, G. Wu, A. Grassellino, E. Harms, O. S. Melnychuk, D. A. Sergatskov, N. Solyak, A. Romanenko, A. Palczewski, D. Gonnella, and T. Peterson. Role of magnetic flux expulsion to reach Q_0>3 $\times$ 10^{10} in superconducting RF cryomodules. *Phys. Rev. Accel. Beams*, 22:032001, Mar 2019. doi:10.1103/PhysRevAccelBeams.22.032001.

[23] M. Martinello, M. Checchin, A. Grassellino, A. C. Crawford, O. Melnychuk, A. Romanenko, and D. A. Sergatskov. Magnetic flux studies in horizontally cooled elliptical superconducting cavities. *Journal of Applied Physics*, 118(4):044505, 2015. doi:10.1063/1.4927519.

[24] M. Checchin, M. Martinello, A. Grassellino, S. Aderhold, S. K. Chandrasekaran, O. S. Melnychuk, S. Posen, A. Romanenko, and D. A. Sergatskov. Frequency dependence of trapped flux sensitivity in SRF cavities. *Applied Physics Letters*, 112(7):072601, 2018. doi:10.1063/1.5016525.

[25] M. Martinello, M. Checchin, M. Checchin, A. Grassellino, O. S. Melnychuk, S. Posen, A. Romanenko, D. A. Sergatskov, and J. Zasadzinski. Trapped flux surface resistance analysis for different surface treatments. Number 17 in International Conference on RF Superconductivity, pages 115–119, Geneva, Switzerland, Dec 2015. JACoW, JACoW. ISBN 978-3-95450-178-6. doi:10.18429/JACoW-SRF2015-MOPB015.

[26] D. Longuevergne and A. Miyazaki. Impact of geometry on the magnetic flux trapping of superconducting accelerating cavities. *Physical Review Accelerators and Beams*, 24(8), Aug 2021. doi:10.1103/physrevaccelbeams.24.083101.

[27] F. Kramer, O. Kugeler, J. Köszegi, and J. Knobloch. Impact of geometry on flux trapping and the related surface resistance in a superconducting cavity. *Phys. Rev. Accel. Beams*, 23:123101, Dec 2020. doi:10.1103/PhysRevAccelBeams.23.123101. URL `https://link.aps.org/doi/10.1103/PhysRevAccelBeams.23.123101`.

[28] P. Kolb, R. Laxdal, and Z. Yao. Low frequency, low beta cavity performance improvement studies. 19th International Conference on RF Superconductivity (SRF 2019), 2019. doi:10.18429/JACoW-SRF2019-TUP046. TUP046.

[29] P. Kolb, Z. Yao, T. Junginger, B. Dury, A. Fothergill, M. Vanderbanck, and R. E. Laxdal. Coaxial multimode cavities for fundamental superconducting RF research in an unprecedented parameter space. *Physical Review Accelerators and Beams*, 23(12), Dec 2020. doi:10.1103/physrevaccelbeams.23.122001.

[30] Z. Y. Yao, T. Junginger, A. N. Koveshnikov, R. E. Laxdal, Y. Ma, D. W. Storey, E. Thoeng, B. S. Waraich, and V. Zvyagintsev. Operating experience on cavity performance of ISAC-II superconducting heavy ion linac. Number 18 in International Conference on RF Superconductivity, pages 527–530, Geneva, Switzerland, Jan. 2018. JACoW. ISBN 978-3-95450-191-5. doi:10.18429/JACoW-SRF2017-TUPB064.

[31] Comsol multiphysics ®, v. 5.4, www.comsol.com. URL www.comsol.com. COMSOL AB, Stockholm, Sweden.

[32] P. Kolb. personal communication.

[33] B. Matheson. Coaxial QWR cavity weldment. Technical Report IRF4010, TRIUMF, 4004 Wesbrook Mall Vancouver, British Columbia, Canada, V6T 2A3, 2017.

[34] M. Laverty, K. Fong, S. Fang, and Q. Zheng. ISAC II RF controls - Status and comissioning. page 3047, 2006.

[35] M. Laverty, K. Fong, and Q. Zheng. TRIUMF e-linac control system design. page 2246, 2009. IEEE, Piscataway, NJ.

[36] P. Kolb. *SRF cavity testing procedure*. TRIUMF, 4004 Wesbrook Mall, Vancouver, BC V6T 2A3, 2019. Document-173967.

[37] Bartington Instruments. Mag-01H single axis fluxgate magnetometer. Brochure, 2022. URL https://bartingtondownloads.com/wp-content/uploads/DS0003.pdf.

[38] P. Harmer. Procedure for etching niobium cavities and parts. Technical Report 123467, TRIUMF, October 2015.

[39] A. Grassellino, A. Romanenko, A. Crawford, O. Melnychuk, A. Rowe, M. Wong, C. Cooper, D. Sergatskov, D. Bice, Y. Trenikhina, L. D. Cooley, C. Ginsburg, and R. D. Kephart. Fermilab experience of post-annealing losses in SRF niobium cavities due to furnace contamination and the ways to its mitigation: a pathway to processing simplification and quality factor improvement. 2013. doi:arXiv:1305.2182.

[40] P. Dhakal, G. Ciovati, W. Rigby, J. Wallace, and G. R. Myneni. Design and performance of a new induction furnace for heat treatment of superconducting radiofrequency niobium cavities. *Review of Scientific Instruments*, 83(6):065105, 2012. doi:10.1063/1.4725589.

[41] G. Ciovati. Effect of low-temperature baking on the radio-frequency properties of niobium superconducting cavities for particle accelerators. *Journal of Applied Physics*, 96:1591 – 1600, 09 2004. doi:10.1063/1.1767295.

[42] A. Romanenko, A. Grassellino, F. Barkov, and J. P. Ozelis. Effect of mild baking on superconducting niobium cavities investigated by sequential nanoremoval. *Phys. Rev. ST Accel. Beams*, 16:012001, Jan 2013. doi:10.1103/PhysRevSTAB.16.012001.

[43] A. Romanenko, F. Barkov, L. D. Cooley, and A. Grassellino. Proximity breakdown of hydrides in superconducting niobium cavities. *Superconductor Science and Technology*, 26(3):035003, Jan 2013. doi:10.1088/0953-2048/26/3/035003.

[44] F. He, W. Pan, P. Sha, J. Zhai, Z. Mi, X. Dai, S. Jin, Z. Zhang, C. Dong, B. Liu, H. Zhao, R. Ge, J. Zhao, Z. Mu, L. Du, L. Sun, L. Zhang, C. Yang, and X. Zheng. Medium-temperature furnace bake of superconducting radio-frequency cavities at IHEP, 2020.

[45] M. Delheusy, A. Stierle, N. Kasper, R. P. Kurta, A. Vlad, H. Dosch, C. Antoine, A. Resta, E. Lundgren, and J. Andersen. X-ray investigation of subsurface interstitial oxygen at Nb/oxide interfaces. *Applied Physics Letters*, 92:101911–101911, 03 2008. doi:10.1063/1.2889474.

[46] M. Martinello, A. Grassellino, M. Checchin, A. Romanenko, O. Melnychuk, D. A. Sergatskov, S. Posen, and J. F. Zasadzinski. Effect of interstitial impurities on the field dependent microwave surface resistance of niobium. *Applied Physics Letters*, 109(6):062601, 2016. doi:10.1063/1.4960801.

[47] S. Posen, A. Romanenko, A. Grassellino, O.S. Melnychuk, and D.A. Sergatskov. Ultralow surface resistance via vacuum heat treatment of superconducting radio-frequency cavities. *Phys. Rev. Appl.*, 13:014024, Jan 2020. doi:10.1103/PhysRevApplied.13.014024.

[48] H. Ito, H. Araki, K. Takahashi, and K. Umemori. Influence of furnace baking on Q-E behavior of superconducting accelerating cavities. *Progress of Theoretical and Experimental Physics*, 2021, 05 2021. doi:10.1093/ptep/ptab056.

[49] P. Dhakal. Nitrogen doping and infusion in SRF cavities: A review. *Physics Open*, 5:100034, 2020. ISSN 2666-0326. doi:10.1016/j.physo.2020.100034.

[50] J. P. Holzbauer, C. Contreras, Y. Pischalnikov, D. Sergatskov, and W. Schappert. Improved RF measurements of SRF cavity quality factors. *Nuclear Instruments and Methods in Physics Research Section A: Accelerators, Spectrometers, Detectors and Associated Equipment*, 913:7–14, 2019. ISSN 0168-9002. doi:10.1016/j.nima.2018.09.155.

[51] D. W. Storey. *A superconducting RF deflecting cavity for the ARIEL e-linac separator*. PhD thesis, University of Victoria, Victoria, BC, 2018.

[52] O. Melnychuk, A. Grassellino, and A. Romanenko. Error analysis for intrinsic quality factor measurement in superconducting radio frequency resonators. *Review of Scientific Instruments*, 85(12):124705, 2014. doi:10.1063/1.4903868.

[53] Agilent Technologies. *Agilent E4419B Power Meter User's Guide*. Agilent Technologies, Inc. 3501 Stevens Creek Blvd. Santa Clara, CA 95052 USA, 2010. Sixth Edition.

[54] Agilent Technologies. *Agilent 53181A 225 MHz Frequency Counter Operating Guide*. Agilent Technologies, Inc. 3501 Stevens Creek Blvd. Santa Clara, CA 95052 USA, 2003.

[55] J. R. Taylor. *An introduction to error analysis: The study of uncertainties in physical measurements*. University Scienece Books, Sausalito, CA, USA, 2nd ed. edition, 1997. ISBN 9780935702422.

[56] J. R. Delayen, H. Park, S. U. De Silva, G. Ciovati, and Z. Li. Determination of the magnetic field dependence of the surface resistance of superconductors from cavity tests. *Phys. Rev. Accel. Beams*, 21: 122001, Dec 2018. doi:10.1103/PhysRevAccelBeams.21.122001.

[57] J. Halbritter. Fortran-program for the computation of the surface impedance of superconductors. Technical Report 3/70-6, June 2006.

[58] W. F. Vinen. The physics of superfluid helium. 2004. doi:10.5170/CERN-2004-008.363.

[59] Y. Song, A. Four, and B. Baudouy. Nucleate boiling heat transfer in a helium natural circulation loop coupled with a cryocooler. *International Journal of Heat and Mass Transfer*, 66:64–71, 2013. ISSN 0017-9310. doi:10.1016/j.ijheatmasstransfer.2013.07.002.

[60] M. C. Jones and W. W. Johnson. Heat transfer and flow of helium in channels–practical limits for applications in superconductivity. Technical Report NBS 675, U.S. Department of Commerce/National Bureau of Standards, Boulder, Colorado, April 1976. Cryogenics Division, Institute for Basic Standards.

[61] *COMSOL Multiphysics Reference Manual*.

[62] D. J. Griffiths. *Introduction to Electrodynamics*. Pearson Education Inc., Glenview, IL, 2013. Fourth Edition.

[63] J.-M. Vogt, O. Kugeler, and J. Knobloch. Impact of cool-down conditions at T_c on the superconducting rf cavity quality factor. *Phys. Rev. ST Accel. Beams*, 16:102002, Oct 2013. doi:10.1103/PhysRevSTAB.16.102002.

[64] J. Cheung. personal communication.

[65] W. Weingarten. Field-dependent surface resistance for superconducting niobium accelerating cavities. *Phys. Rev. ST Accel. Beams*, 14:101002, Oct 2011. doi:10.1103/PhysRevSTAB.14.101002.

[66] P. Bauer, N. Solyak, G. Ciovati, G. Eremeev, A. Gurevich, L. Lilje, and B. Visentin. Evidence for non-linear bcs resistance in srf cavities. *Physica C: Superconductivity*, 441:51–56, 07 2006. doi:10.1016/j.physc.2006.03.056.

[67] M.W. McMullin, T. Junginger, P. Kolb, R.E. Laxdal, and Z. Yao. Thermal feedback in coaxial SRF cavities. Pre-Press Publication, June 2023. URL https://srf2023.vrws.de/papers/suspb020.pdf.

[68] R.E. Laxdal B. Waraich V. Zvyagintsev A. Grassellino, K. Fong. Medium field Q-slope studies in quarter wave cavities. 14th International Conference on RF Superconductivity (SRF 2014), 2009. URL https://accelconf.web.cern.ch/srf2009/papers/tuppo062.pdf. TUPPO62.

[69] H. Padamsee. *RF superconductivity*. Wiley-VCH, 2009. ISBN 9783527405725.

[70] S. Calatroni and R. Vaglio. Simple model for the rf field amplitude dependence of the trapped flux sensitivity in superconducting rf cavities. *Physical Review Accelerators and Beams*, 22(2), feb 2019. doi:10.1103/physrevaccelbeams.22.022001.